Measuring Interactions in Cells with Spatial Image Cross-Correlation Spectroscopy: Characterization, Application and Advances

Jonathan W. D. Comeau
Department of Chemistry
McGill University
Montréal, Québec
Canada

February, 2008

A Thesis submitted to McGill University
in partial fulfillment of the requirements for the degree of
Doctor of Philosophy

Your file Votre référence
ISBN: 978-0-494-50801-5
Our file Notre référence
ISBN: 978-0-494-50801-5

Contents

Abstract vi

Résumé vii

Statement of Originality viii

Acknowledgments x

List of Abbreviations xii

1 Introduction 1

1.1 An Overview of the Eukaryotic Cell 1
1.2 The Role of Protein Interactions 4
1.3 Measuring Protein Interactions 5
1.4 Fundamentals of Fluorescence 9
1.5 Fluorescence Microscopy 11
1.6 Fluorescence Labeling 16
1.6.1 Immunofluorescence Labeling 16
1.6.2 Genetically Encoded Fluorescent Proteins 19
1.7 Fluorescence Microscopy Colocalization Measurements 21

2 Theory 39

2.1 Fluorescence Correlation Spectroscopy (FCS) 40
2.1.1 Fluorescence Cross-Correlation Spectroscopy (FCCS) 44
2.2 Image Correlation Spectroscopy (ICS) 46
2.2.1 Image Cross-Correlation Spectroscopy (ICCS) 50
2.3 Automatic Colocalization 53
2.3.1 Colocalization Significance Test 56

3 Materials and Methods 64

3.1 Computer Simulated Images with Interacting Populations of Point Emitters 64
3.2 Antibodies 67
3.3 Antibody Adsorption on Glass 67
3.4 Cell Culture and PDGF-β Labeling 68
3.5 Transfection of YFP-Talin constructs in CHO-K1 cells 69
3.6 Microscopy 69

4 Accuracy and Dynamic Range of Colocalization Measurements 74
4.1 Simulation Results . . . 76
4.1.1 Colocalization Detection Limits . . . 76
4.1.2 Dynamic Range . . . 79
4.1.3 Effect of Noise on Colocalization Measurements . . . 84
4.2 Experimental Results . . . 88
4.2.1 Adsorption of Antibody on Glass . . . 88
4.2.2 Analysis of PDGF-β Receptor Labeled AG01523 Human Foreskin Fibroblasts . . . 91

5 *In vivo* studies of AP-2/β-arrestin Complexes 96
5.1 Introduction . . . 97
5.2 β-arrestin Mediated Endocytosis . . . 99
5.3 Regulation of the Interaction between β-arrestin and AP-2 investigated by Image Cross-Correlation Spectroscopy . . . 102

6 Advances in ICCS 112
6.1 Variable Binding Stoichiometry . . . 113
6.1.1 ICCS Analysis of Multiple Binding Interactions: Stoichiometric ICCS . . . 121
6.2 Improving the ICCS Detection Limits . . . 126
6.2.1 Image Scrambling for Spatial ICCS . . . 129
6.3 Particle Distribution in ICCS . . . 135
6.3.1 ICCS Analysis of Focal Adhesion Proteins . . . 136
6.4 ICCS Analysis of Arbitrary Regions within Images . . . 141

7 Conclusion 149

8 Appendix A: Derivation of Equation 6.5 157

9 Appendix B: Biohazardous Materials Certificate 159

10 Appendix C: Copyright Permission Form 160

Figures and Tables

Figures

1.1 Components of the eukaryotic cell . . . 2
1.2 Protein interactions at focal adhesions . . . 3
1.3 Protein interaction map in yeast . . . 8
1.4 Jablonski energy diagram . . . 10
1.5 Absorption and emission spectrum of fluorescein isothiocyanate . . . 11
1.6 Schematic diagram of a conventional fluorescence microscope . . . 12
1.7 Schematic diagram of a two channel confocal laser scanning microscope 14
1.8 Schematic diagram of total internal reflection fluorescence microscope 14
1.9 The structure of the IgG antibody . . . 17
1.10 Indirect immunofluorescence labeling schematic and a confocal fluorescence image of the immunolabeled platelet derived growth factor receptor-β . . . 18
1.11 Fluorescence spectrum and structure of enhanced green fluorescent protein . . . 19
1.12 Fluorescence resonance energy transfer . . . 23
1.13 Statistical colocalization analysis . . . 26

2.1 Overview of fluorescence correlation spectroscopy . . . 40
2.2 Overview of fluorescence cross-correlation spectroscopy . . . 45
2.3 Temporal image cross-correlation spectroscopy . . . 47
2.4 Spatial image cross-correlation spectroscopy . . . 51
2.5 Method of automatic colocalization determination . . . 55
2.6 Colocalization significance test . . . 58

4.1 Example two channel simulation images . . . 75
4.2 Automatic colocalization detection limit . . . 77
4.3 ICCS detection limits as a function of the number of independent fluctuations per image . . . 78
4.4 2D surface plot of the ICCS measured interaction fraction as a function of the densities of particles in both simulated image detection channels 81
4.5 Absolute value of the relative error in automatic colocalization analysis 82
4.6 Density dependence of colocalization measurements at a fixed channel density ratio . . . 83
4.7 Effect of noise on colocalization measurements . . . 85
4.8 2D surface plot of the absolute value of the relative error in $M1$ as a function of S/B ratio of each image . . . 87
4.9 Colocalization analysis of the adsorption of antibody on a glass surface 89

4.10 Measurement of the counting noise width factor 90
4.11 Colocalization analysis of immunolabeled PDGF-β receptors in human fibroblasts 92

5.1 G protein-coupled receptor activation 98
5.2 β-arrestin mediated endocytosis 101
5.3 Experimental schematic of the determination of the stability of endocytic complexes 103
5.4 Two channel fluorescence image time series of β-arrestin2-CFP and β2-adaptin-YFP in HEK293 cells 105
5.5 $M2_{ICCS}$ as a function of time after addition of angiotensin II for five wild type and five Y737F β2-adaptin mutant cells 107
5.6 The dissociate rate of β-arrestin2/β2-adaptin complexes in HEK293 cells 108

6.1 Polyvalent interactions in biological systems 113
6.2 Particle brightness in multiple ligand binding systems 115
6.3 ICCS analysis of multiple ligand binding molecules 124
6.4 ICCS detection limits with pre-ICCS analysis image scrambling as a function of the number of independent fluctuations per image 127
6.5 Spatial two channel image scrambling 130
6.6 The effect of random spatial scrambling on the calculated spatial cross-correlation function 132
6.7 ICCS detection limits with spatial image scrambling as a function of the number of independent fluctuations per image 134
6.8 The effect of uniform and nonuniform spatial distributions of particles on the autocorrelation function 136
6.9 Spatial correlation analysis of focal adhesions 138
6.10 Spatial cross-correlation analysis of focal adhesions 140
6.11 Spatial correlation with mean padding of the image 142
6.12 Arbitrary selection of regions of analysis in ICCS 143
6.13 The interaction of actin and α-actinin at the leading edge of a migrating cell 145

Tables

4.1 Automatic colocalization vs. ICCS 94

6.1 Stoichiometric ICCS analysis of fluorescently tagged antibodies incubated with primary antibodies adsorbed on glass 125

Abstract

The objective of this thesis research project is to provide a complete, systematic characterization of spatial image cross-correlation spectroscopy (ICCS) for its use in quantifying molecular interactions via analysis of fluorescence microscopy images. In spatial ICCS, cross-correlation of fluctuations in fluorescence intensity recorded as images from two independent wavelength detection channels in a fluorescence microscope is used to determine the average number of interacting particles in a sample. Other statistical image analysis methods exist that can be performed on fluorescence microscopy images of fixed or live cells and have been routinely applied for biophysical studies of molecular interaction. These approaches measure the fraction of interacting particles by analyzing fluorescence images from two detection channels for colocalized pixels. Colocalization algorithms have been widely used, although the dynamic range and accuracy of these measurements has never been well established. Using computer simulations, control experiments of fluorescently labeled antibodies adsorbed on glass, and cell measurements, we show that ICCS is more accurate than standard colocalization algorithms at moderate to high densities of particles, which are often encountered in cellular systems. Furthermore, it was found that the density ratio between the two labeled species of interest plays a major role in the accuracy of the colocalization analysis. By applying a direct and systematic comparison between the standard, fluorescence microscopy colocalization algorithms and spatial ICCS, we show regimes where each approach is applicable, and more importantly, where they fail to yield accurate results. Spatial ICCS was then used to measure a 4-fold increase in the dissociation rate of phosphorylated AP-2/β-arrestin complexes, important regulatory proteins of G protein-coupled receptors in living cells. New approaches to improve ICCS were also studied. Spatial scrambling of pixel blocks within fluorescence images was investigated as a way of extending the detection of two-channel ICCS to measure lower interaction fractions as well as colocalization within large structures. ICCS theory was also extended to handle the analysis of systems with multiple ligand-binding sites.

Résumé

L'objectif de cette thèse de doctorat est de fournir une caractérisation systématique de la spectroscopie par corrélation croisée d'images (SCCI) pour quantifier des interactions moléculaires via l'analyse d'images prises par microscopie en fluorescence. Pour la SCCI spatiale, la corrélation croisée de fluctuations de la fluorescence enregistrée par les images de deux canaux de détection avec des longueurs d'onde différentes est utilisée pour déterminer le nombre moyen de particules en interaction dans un échantillon. D'autres méthodes statistiques d'analyse d'images existent et peuvent être appliquées sur des images de microscopie en fluorescence de cellules vivantes ou fixées. Ces approches mesurent la fraction de particules en interaction par l'analyse d'images provenant de deux canaux de détection pour chaque pixel colocalisé. Les algorithmes de colocalisation ont été grandement utilisés, bien que l'étendue dynamique et l'exactitude de ces mesures n'a jamais été bien établies. En utilisant des simulations, des expériences de contrôle impliquant des anticorps marqués adsorbés sur le verre et des mesures faites sur des cellules, nous démontrons que la SCCI est plus exacte que les algorithmes de colocalisation utilisés pour des densités de particules de modérées à élevées, ce qui est souvent le cas pour les systèmes cellulaires. En appliquant une comparaison directe et systématique entre la méthode standard, les algorithmes de colocalisation de la microscopie en fluorescence, et la SCCI, nous démontrons des régimes où chaque approche est applicable, et d'une plus grande importance, où elles échouent à fournir des résultats exacts. La SCCI spatiale a été utilisée pour mesurer une augmentation de 4 fois dans le taux de dissociation de complexes phosphorylés de AP-2/β-arrestin, une protèine régulatrice importante de récepteurs couplés aux protèines G dans les cellules vivantes. De nouvelles approches pour améliorer la SCCI ont aussi été étudiées. Un mélangeage spatial de blocs de pixels à l'intérieur même d'images en fluorescence a été étudié comme moyen d'étendre à des fractions d'interaction plus basse et à des structures plus larges la SCCI. La théorie de la SCCI a aussi été étendue de façon à couvrir l'analyse de systèmes contenant de multiples sites ligand-liants.

Statement of Originality

The author claims the following aspects of the thesis constitute original scholarship and an advancement of knowledge:

1. The complete characterization of the dynamic range and accuracy of spatial image cross-correlation spectroscopy (ICCS) for its use in measuring intermolecular interactions from two-channel fluorescence images. ICCS is a spatial intensity fluctuation cross-correlation technique that can be applied to fluorescence images of fixed or live cells to quantify any molecular interactions that exist between labeled molecules of interest. The following points summarize the major findings that led to establishing the first experimental guidelines to be proposed for the broader use of ICCS in biological systems.

- Fundamental limits on the minimum numbers of interacting particles that could be detected using ICCS were found to exist, and quantified in terms of the amount of spatial sampling that was recorded in the two channel images.
- Accurate measurements of the particle interaction fractions were obtained, provided the ratio between the particle number densities in each detection channel was less than 10.
- Accurate measurements of the particle interaction fractions were obtained, even in the presence of significant levels of noise, provided the levels of noise in each detection channel were comparable.

2. A systematic comparison of ICCS with other, common two channel fluorescence microscopy 'colocalization' analysis methods was performed, and it was demonstrated for the first time, that these methods lead to significant errors in the measured particle interaction fractions when the densities of the two labeled species differ. These statistical colocalization techniques are widely applied to fluorescence images of biological systems, but their accuracy has never been well established.

The simulations and cell experiments from which these conclusions are drawn are presented in detail in Chapter 4. All simulations were performed by the author using custom written Matlab programs with the following exceptions: David Kolin

(Wiseman Group) wrote the nonlinear fitting routines used to fit the calculated correlation functions. Dr. Santiago Costantino (Wiseman Group) wrote the program for simulating fluorescence images, which was extended by the author to include a cross-correlated population between two images. Dr. Santiago Costantino wrote the Matlab routine for adding background and counting noise to an image, which was modified by the author to add noise to cross-correlated images. Dr. Costantino modified the automatic colocalization routine that was written by the author to significantly increase its speed.

3. In collaboration with the group of Stéphane Laporte (Department of Medicine, McGill University), spatial ICCS was applied to live cells to identify and quantify the interaction between two important cell-signal regulatory proteins AP-2 and β-arrestin (Chapter 5). The HEK293 cells used in this study were cultured and transfected with small interfering RNA and fluorescent protein constructs by members of the Laporte group (Brandon Zimmerman, May Simaan). The confocal fluorescence images presented were acquired by Stéphane Laporte, Brandon Zimmerman, and myself using Prof. Laporte's microscope in the Department of Medicine at McGill University. The quantification of the interaction between AP-2 and β-arrestin via ICCS analysis of these images sets was then performed by the author in the Department of Chemistry at McGill University. These ICCS measurements confirmed that a specific phosphorylation site on the AP-2 protein, that was hypothesized to regulate its interaction with β-arrestin after several biochemical studies by the Laporte group, does in fact control the affinity of AP-2 for β-arrestin *in vivo*.

4. The design and implementation of new procedures toward improving the range of applicability of spatial ICCS was performed. The extension of ICCS analysis to molecules with multiple binding sites was demonstrated through simulation studies. Spatial image scrambling, combined with 'mean-padding' of images, was shown to extend the technique of spatial ICCS to the analysis of small, arbitrarily selected regions within the images, which is not possible without the procedures described in Chapter 6. The TIRF microscopy images that were analyzed by these new techniques as a proof of principle were generously provided by Dr. Claire Brown at McGill University.

Acknowledgments

Many thanks to all those who have helped make the completion of this thesis possible. Without the support of each and everyone of you, it surely would have been an impossible task...

The thoughtful supervision of Prof. Paul W. Wiseman has been greatly appreciated throughout the duration of my studies at McGill University. His enthusiasm for science, and for life in general, has made this personal journey of the past several years a profound learning experience. For teaching me to be a better scientist I thank you.

It has been an privilege to work side-by-side with Alexia Bachir from day one. We founded the Wiseman Group (with a little help from Wiseman himself), and I could not think of a better person to share that honour with. I thank David Kolin for his unlimited willingness to discuss any subject that I deemed appropriate at any given moment, whether it be Matlab functions, image scrambling, or hockey, all I needed to say was, "Hey, Dave?" from the other side of the lab. To our first postdoc, Santiago Costantino, I wish to offer sincere thanks for the broad range of knowledge and determination he brought to the lab, and the extra-supervision he provided to all the members of the group. Santiago is a great scientist, but an even greater person, and I wish him health and happiness for years to come. I would like to thank Ben Hébert, Mikhail Sergeev, Antoine Godin, Chris McQuinn, Jonathan Bélisle (especially for his French translation services), Richard Naud, Nela Durisic, Elvis Pandzic, Katrin Heinze, Jody Swift and Colin Heyes, and whomever else I have shared a lab with in the Wiseman group. I can honestly say that is has been a privilege to work and laugh with every past and present member of the group. I have learned so much from each and every member.

I owe a great deal of thanks to several collaborators who have helped me along the way. I only worked with the research group of Prof. Stéphane Laporte at McGill University, Department of Medicine, for a short time, but I enjoyed every minute.

Stéphane's passion for science is contagious, and I learned a great deal from working with him. I would like to specifically thank Brandon Zimmerman and May Simaan from the Laporte group for their hard work in preparing transfected cells, and sharing some of their vast cell biological knowledge. Many thanks to Prof. Rick Horwitz at the University of Virginia, Jessica Zareno, and Colin Choi, for providing several stable GFP-labeled cell lines that were used in many different imaging experiments, and for providing the YFP-talin plasmid that was used to label CHO-K1 cells. Special thanks to Dr. Claire Brown, now at McGill University, for transforming the DNA plasmids and offering troubleshooting advice, experimental suggestions, and discussions in general. I also like to thank Profs. Yves de Koninck and Paul de Koninck at the Université Laval for inviting me into their labs when I first started for training on a confocal fluorescence microscope.

Finally, I must thank my family, (Moms, Dads, Sisters, Brothers, Aunts, Uncles, Cousins), for all their continuing support, and of course, my beautiful wife Sabine Schnepf-Comeau, for her unconditional support of my studies. Loves.

Mille mercis.

List of Abbreviations

ACF	autocorrelation function
Ang	angiotensin
ATP	adenosine triphosphate
AT1R	angiotensin II type 1 receptor
BA	beam area
BSA	bovine serum albumin
CaM	calmodulin
CaMKII	Ca^{2+}/calmodulin-dependent protein kinase II
CCD	charge-coupled device
CCF	cross-correlation function
CCV	clathrin-coated vesicle
CFP	cyan fluorescent protein
CHO	chinese hamster ovary
CLSM	confocal laser scanning microscope
DNA	deoxyribonucleic acid
EGFP	enhanced green fluorescent protein
FCS	fluorescence correlation spectroscopy
FCCS	fluorescence cross-correlation spectroscopy
FITC	fluorescein isothiocyanate
FRET	fluorescence resonance energy transfer
GDP	guanosine diphosphate
GFP	green fluorescent protein
GPCR	G protein-coupled receptor
GRK	G protein-coupled receptor kinase
GTP	guanosine triphosphate
HA-AT1R	hemagglutinin-tagged angiotensin II type 1 receptor
HEK	human embryonic kidney
ICS	image correlation spectroscopy
ICCS	image cross-correlation spectroscopy
IF	interaction fraction

MAPK	mitogen-activated protein kinase
mRFP	monomeric red fluorescent protein
NA	numerical aperture
NIF	number of independent fluctuations
PBS	phosphate buffered saline
PDGF-β	platelet derived growth factor-β
PDGF-BB	platelet derived growth factor-BB
PMT	photomultiplier tube
PSF	point spread function
RGB	red-green-blue
RNA	ribonucleic acid
siRNA	small interfering ribonucleic acid
S/N	signal-to-noise
S/B	signal-to-background
TIRF	total internal reflection fluorescence
WF	width factor
wt-GFP	wild-type green fluorescent protein
YFP	yellow fluorescent protein
2D	2-dimensional
3D	3-dimensional

1

Introduction

1.1 An Overview of the Eukaryotic Cell

Atoms and molecules are the basic building blocks of all matter on Earth, while micrometer-sized, membrane-enclosed cells that are present in all living things constitute the basic units of life. From the simplest single-celled bacteria, to the more complex, multi-cellular plants and animals, it is the cell that is the common thread that unites all living organisms. Since the description presented by Robert Hooke in the 17th century of the microscopic structure of cork [1], the cell has been the subject of intense study by scientists, due in part to the inspiring complexity they possess, and the fact that the cell represents the ever-engaging mystery of life itself.

The eukaryotic cell consists of several smaller compartments called organelles that carry out the necessary functions of life. The nucleus, enclosed in a porous, double lipid-bilayer envelope, contains double-stranded deoxyribonucleic acid (DNA), which is the genetic blueprint for the cell and encodes all of the information that is required to synthesize all of the cellular components. Double-membrane enclosed organelles called mitochondria, that are present in almost every cell, generate the fuel that powers all cellular functions. These organelles oxidize nutrients, such as glucose, to produce adenosine triphosphate (ATP), which is eventually hydrolyzed to provide energy to cells. The endoplasmic reticulum and Golgi apparatus are equally important organelles that work together to synthesize and sort proteins destined for incorporation into the cell membrane or to be exported from the cell altogether [2].

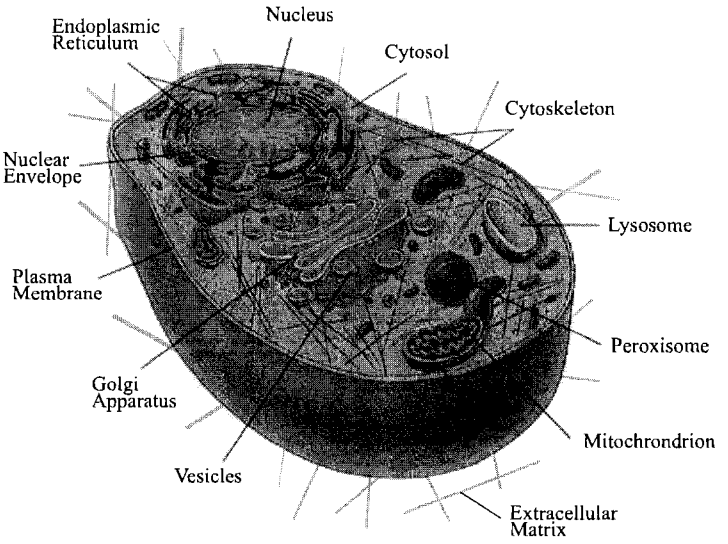

Figure 1.1: *The eukaryotic cell is comprised of specialized compartments called organelles, which are enclosed within a phospholipid membrane bilayer. Eukaryotic cells typically range from 2-100 μm in diameter. Adapted from [3].*

As we can see in Fig. 1.1, many other organelles exist in eukaryotic cells, such as lysosomes, which act as isolated compartments for intracellular digestion as well as many smaller vesicles, which are used to transport a variety of cargoes to various locations throughout the cell. All of these organelles are present in a highly concentrated aqueous solution of large and small molecules called the cytosol.

The shape of the cell is actively maintained by a network of polymeric microtubules, intermediate and actin filaments, referred to collectively as the cytoskeleton. The cytoskeleton is by no means a static, rigid structure as the name might suggest. In fact, it is an extremely dynamic meshwork that is largely responsible for cell migration, generation of contractile forces, and separating chromosomes during cell division [4, 5]. The cytoskeleton also serves as an intracellular highway on which specialized motor proteins travel and actively transport vesicle or molecular cargoes throughout the cell [6].

The entire cell is enclosed by the plasma membrane, which consists of a lipid bilayer

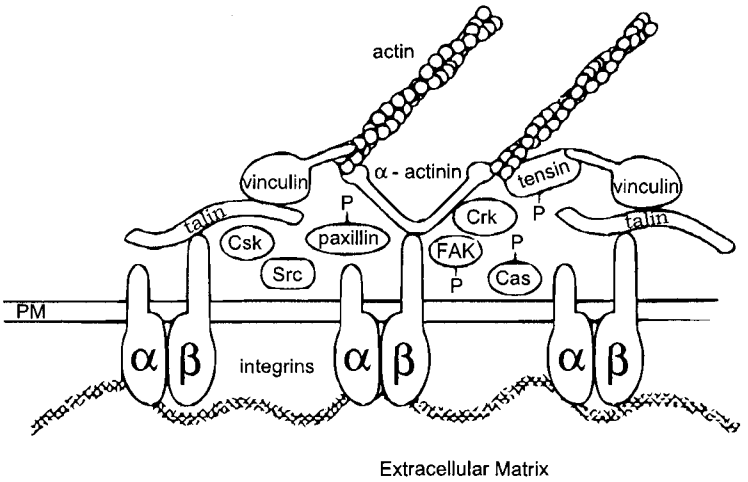

Figure 1.2: Focal adhesions are composed of a large number of interacting components and are formed when a cell binds to a surface. Integrin membrane receptors are adhesion molecules that link the extracellular matrix to elements of the cytoskeleton, but also act as signaling molecules by mediating cell signaling pathways, which lead to proliferation and differentiation. Many different signaling molecules (Cas, Crk, Csk, Src) are recruited to focal adhesions where they initiate signal propagation, which is often carried out by means of phosphorylation of target proteins. FAK; focal adhesion kinase. P; phosphorylated tyrosine. PM; plasma membrane. Adapted from [9].

composed of several types of phospholipids. Many integral proteins are incorporated into the plasma membrane. These proteins span across the entire bilayer and provide a link between the cytosolic interior and exterior, or extracellular matrix, of the cell. Numerous types of transmembrane proteins exist to carry out an array of important functions. For instance, certain integral proteins act as ion channels to maintain small concentration gradients across the plasma membrane, which is particularly important for signal transduction in the nervous system [7]. Others act as signaling receptors by the binding of extracellular ligands, which results in the initiation of specific signaling pathways within the cell [8]. Yet others act as direct sites of adhesion and migration by linking extracellular substrate proteins to intracellular cytoskeletal components [5] (see Fig. 1.2). The plasma membrane, therefore, not only serves as a selective barrier between the outside and the inside of the cell, but a dynamic and responsive locale that is implicated in many essential cellular processes.

From a chemist's perspective, the cell could be considered an amalgamation of

many different coordinated chemical reactions that are often complex and far from equilibrium. This has always made the cell a particularly difficult system to study, in addition to its small size. There is, however, an extraordinary number of underlying chemical similarities in the cells of all living species. Cellular DNA encodes for sequences of twenty different amino acids that are strung together by peptide bonds to produce the vast array of different proteins. This stored information, once transcribed and translated, leads to a large variety of specialized cell types, like the highly extended motor neurons of the central nervous system or the sound-transducing hair cell of the inner ear. Fortunately, the similarities in chemical composition allow for the systematic study of particular cellular components and processes, and the ability to extend any knowledge gained to the life process in general.

1.2 The Role of Protein Interactions

From the beginning of a cell's life during the M-phase of the cell cycle, until its eventual programmed death by apoptosis, the cell carries out many biochemical reactions and functions, practically all of which are regulated by polypeptides called proteins. Moreover, the overwhelming majority of proteins do not function alone, but through direct associations with other proteins and molecules in sequence or as part of larger complexes. These direct protein interactions are essential to the proper function of any cell and regulate some of the most important cellular processes such as DNA transcription [10], cell cycle regulation [11], metabolic pathways [12] and virtually every other crucial endeavor carried out by a given cell.

One example of protein-protein interaction is seen in the many classes of multi-subunit proteins that have been identified. The functional forms of these proteins consist of separate protein macromolecules that associate with one another through multiple, non-covalent, but essentially permanent, bonds. Functional hemoglobin, for example, which transports oxygen from the lungs to tissues throughout the rest of the body, exists as a tetramer of two pairs of identical protein subunits, each of which

are held together by weak ionic bonds, hydrogen bonds, and hydrophobic interactions [13].

Another important class of transient protein-protein interactions is the association of a biological catalyst protein, or enzyme, with its substrate. Protein kinases are a large class of enzymes that transfer phosphate groups from ATP to target proteins [14]. The initial step of this phosphorylation reaction is the non-covalent binding of the substrate protein to the binding pocket of the enzyme. Phosphorylation typically activates or deactivates target proteins by increasing or decreasing their affinity for other proteins, and is therefore implicated in a series of cellular signal transduction mechanisms [15–17].

The net effect of a multitude of cellular interacting partners is to maximize a variety of functions from a limited set of components. Accordingly, the first step in understanding the underlying mechanisms that regulate cellular function is quite often the detection and quantification of molecular interactions in cells. To this end, many techniques for measuring protein interactions have been developed, and continue to be applied for both *in vitro* and *in vivo* studies, each with varying degrees of success.

1.3 Measuring Protein Interactions

Classical approaches to measure protein-protein interactions include several biochemical assays, which have proved particularly useful for the initial identification of potential interacting protein pairs. Protein affinity chromatography is such an assay, whereby proteins of interest are covalently attached to a column of cross-linked agarose, and screened against cell extracts. The proteins identified in the fraction of the extract with the longest retention time along the column are considered possible interacting partners [18]. Proteins may also be separated by electrophoresis and subsequently screened against possible high affinity binding partners on a nitrocellulose membrane (affinity blotting). A significant advantage of this approach is that no protein purification is required prior to the analysis, which facilitates the testing of

the often difficult to purify membrane proteins [19].

Perhaps the most common biochemical approach for measuring protein interactions is by exploiting the specificity of the antibody-antigen interaction through co-immunoprecipitation [20, 21]. An antibody is developed against a particular protein of interest and added to a cell extract where it selectively binds to the protein (antigen). The resulting antibody-protein complex is then precipitated by an antibody-binding protein (e.g. protein G) attached to a solid support, and analyzed for the presence of other proteins/molecules that were co-precipitated with the original protein of interest. It is assumed that any proteins identified in the precipitate are interacting partners, and are therefore related to a particular function of the target protein *in vivo*. However, as is the case in each of the methods briefly described above, further investigation is usually warranted to justify this assumption.

Understanding the complex interconnected relationships between all the protein-protein interactions that drive most cellular functions is a daunting task that has only started to be achieved in last fifteen years with the development of high-throughput techniques such as two-hybrid screening [22]. The two-hybrid system is a genetic based method that relies on the activation of a reporter gene to indicate the presence of particular protein interactions. An important step in protein synthesis is transcription, or the transfer of the information encoded in the four base pairs of DNA to ribonucleic acid (RNA). This process is regulated by special proteins called transcription factors, which bind to DNA promoter sequences and activate the synthesis of RNA by controlling the binding of RNA polymerase. The first two-hybrid system was based on the GAL4 transcription factor in a species of budding yeast [23]. Fields and Song showed that the transcription factor could still be activated (i.e. a gene was expressed), if the binding domain and the activating domain were split and separately attached to two hybrid proteins that were known to interact.

A typical two-hybrid screening experiment consists of engineering DNA plasmids that produce two sets of hybrid proteins. One of the hybrid proteins is composed

of the binding domain of a transcription factor, such as GAL4, fused to a protein of interest (bait). In the second set of hybrids, a different protein, or an entire library of proteins (prey), is fused to the activating domain of the transcription factor. Yeast cells are transformed with the DNA plasmids encoding for these hybrid proteins and the reporter gene will only be transcribed if both the binding domain and the activating domain of the transcription factor are able to come into close proximity by the binding of the bait and prey proteins. The transcription of the reporter gene itself must then be detected in the phenotype of the cell in order to confirm the interaction of the two proteins of interest. This is accomplished in several ways depending on the reporter gene used in the experiment, and can be as simple as the death of cells that do not successfully express the reporter gene [24]. Two-hybrid experiments set the stage, not only for large-scale screening of interacting proteins, but for mapping of the entire network of interactions in cells [25, 26] (Fig. 1.3).

Although high-throughput screening approaches are promising and offer a wealth of information, the presence of numerous false-positive results has led to questions regarding the accuracy of these methods [27]. Also, spatial and temporal information with respect to the individual protein interactions is lost with high-throughput screening methods, which means other techniques that are capable of extracting this information are essential to a better understanding of the protein-interaction networks in cells. Nevertheless, the accuracy of two-hybrid approaches is steadily improving [28], and as such, they continue to play an important role in identifying the protein binding partners involved in a myriad of cellular interactions.

A molecular binding event inside a cell results in a number of measurable effects, which can be used to monitor the presence of such interactions. Changes in binding affinities [29], secondary structural changes [30], or reduced diffusion coefficients [31] are just some of the effects that have been observed following molecular binding events. Perhaps this is the reason why so many different techniques can be tailored to fit the particular detection needs of a given system. Surface plasmon resonance

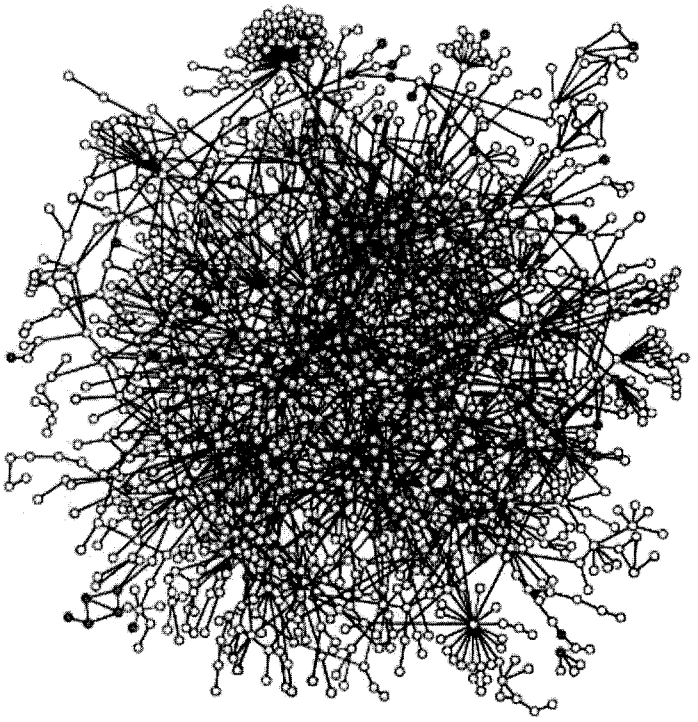

Figure 1.3: Protein-protein interaction map depicting part of the complex network of interacting proteins in yeast. Each circle represents a protein and lines are used to represent interactions with other proteins. Adapted from [26].

[32], isothermal titration calorimetry [33], mass spectroscopy [34] and atomic force microscopy [35] have all been successful in measuring, and in some cases quantifying, the interaction between two proteins. None of these methods, however, has found as widespread application as optically based spectroscopic techniques, in particular, fluorescence spectroscopy and microscopy.

1.4 Fundamentals of Fluorescence

The molecular property of luminescence was first observed by Sir John Herschel who reported on the blue light emanating from a solution of quinine sulphate [36]. Since Herschel's detailed observation over 150 years ago, luminescence has been studied extensively and continues to be an important phenomenon employed for a broad range of spectroscopic and microscopy applications.

Luminescence is defined as the emission of light that results when a molecule relaxes from an excited electronic energy state to its ground state. Two types of luminescent emission are possible depending on the nature of the excited state prior to relaxation. The first is fluorescence, which is the emission of a photon that occurs when a molecule makes a transition from an excited electronic singlet state to the singlet ground state ($S_1 \rightarrow S_0$). Phosphorescence is the emission that occurs as a result of a forbidden transition from an excited triplet state to the singlet ground state ($T_1 \rightarrow S_0$), and therefore, occurs at much slower rates than that of fluorescence for most molecules [37].

A typical Jablonski energy level diagram, named after the Ukrainian physicist who was a pioneer in the photoluminescence field, is shown in Fig. 1.4 to illustrate the relaxation processes that may result in fluorescence, phosphorescence, or non-radiative transitions to the ground state. Very rapid absorption ($\sim 10^{-15}$ s) of a photon of sufficient energy will promote an electron from the ground state to one of the electronic excited states of the molecule. This is followed by internal conversion, that is, the rapid non-radiative relaxation ($\sim 10^{-12}$ s) to the S_1 state in addition to

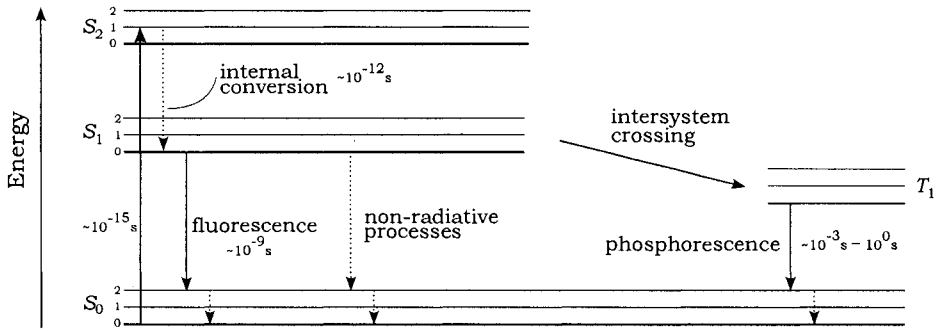

Figure 1.4: A typical Jablonski energy diagram to illustrate the mechanism by which a molecule undergoes fluorescence emission upon relaxation from an excited electronic energy level to the ground state ($S_1 \rightarrow S_0$). Non-radiative decay processes include any mechanism by which quenching, i.e. non-radiative energy transfer, occurs.

molecular relaxation to the lowest vibrational energy level of S_1. After a period of time that is typically on the order of nanoseconds, the molecule may relax to the ground state, S_0, by emission of a fluorescence photon, which is followed by rapid equilibration to the lowest vibrational level of the ground state ($< 10^{-12}$ s). The combination of loss of energy by internal conversion followed by transitions to different vibrational levels of the ground state results in an equally broad, red-shifted (Stoke's shift) emission spectrum with respect to the absorption spectrum (Fig. 1.5). If intersystem crossing to the triplet state occurs prior to photon emission then the molecule may relax to the ground state through phosphorescence emission rather than fluorescence.

Several other relaxation mechanisms exist that are non-radiative in that no photon is emitted upon return to the ground state. These include collisions with other molecules, energy transfer to acceptor molecules through dipole-dipole interactions, as well as others. The ratio of the number of photons emitted to the number of photons absorbed is defined as the fluorescence (or phosphorescence) quantum yield of a particular molecule. Quantum yields are usually the highest for aromatic molecules with conjugated ring systems.

An important characteristic of a fluorescent molecule is the average time spent in the excited state before emission of a photon, which is referred to as the fluorescence lifetime, τ_f. Fluorescent lifetimes are on the order of 10^{-9} s, which allows sufficient

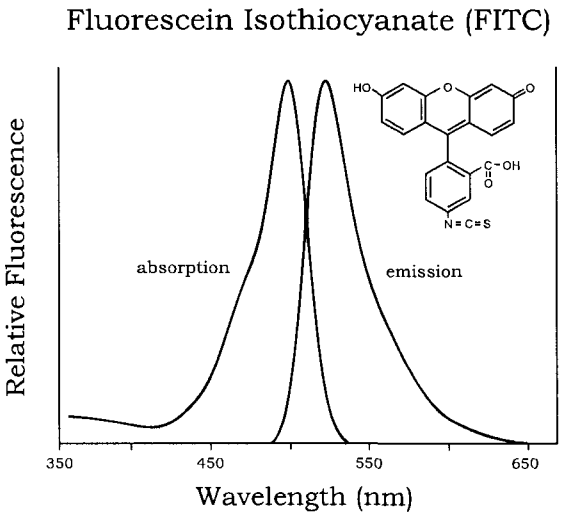

Figure 1.5: Absorption and emission spectrum of fluorescein isothiocyanate (FITC). The molecular structure of FITC is shown in the upper right portion of the figure. Adapted from [37].

time for reorientation of solvent molecules (< 40 ps) around excited state dipoles prior to photon emission. This rearrangement alters the excited state energy. Consequently, the local solvent environment can be probed by measuring shifts in the fluorescence wavelength [38], as well, information regarding rotation of the fluorophore itself can be obtained by applications that use polarized light excitation and detection [39].

Due to several factors including the inherent sensitivity derived from detection against a dark background, the molecular information contained therein and the timescales described above, fluorescence experiments have found many applications in biological (and non-biological) systems [37].

1.5 *Fluorescence Microscopy*

Cellular imaging using conventional light (transmission) microscopy suffers from an inherent lack of contrast, which can only be partially overcome by following appropriate staining procedures. The development of specific fluorescence labeling techniques on the other hand, combined with the inherent sensitivity of fluorescence detection (low background signals with single molecule detection possible) has propelled fluo-

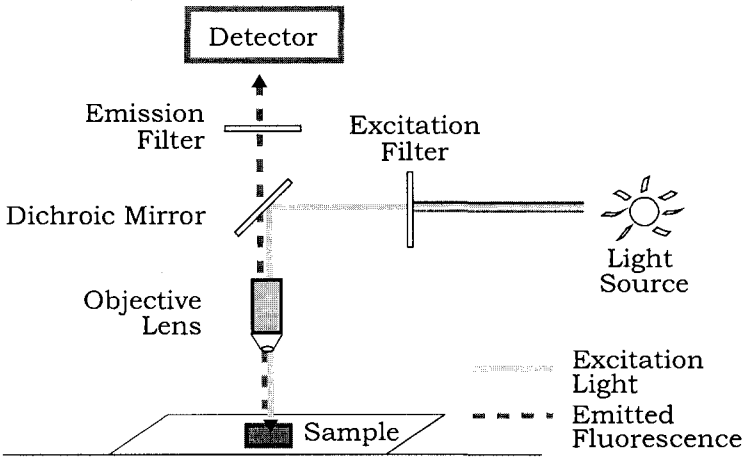

Figure 1.6: Schematic diagram of a conventional fluorescence microscope depicting the optical path taken by the light from the excitation source and the corresponding emitted fluorescence. Typical light sources are either the mercury or xenon arc lamps, while detection is accomplished by use of charge-coupled device (CCD) cameras.

rescence imaging to the forefront of biological light microscopy.

A typical optical path of a fluorescence microscope is shown in Fig. 1.6. Light from an excitation source, such as a mercury lamp, is reflected and focused on the sample using a wavelength selective dichroic mirror and an objective lens respectively. The red-shifted emitted fluorescence is then collected with the same objective, separated from the excitation light by passing through the dichroic mirror, and wavelength filtered before reaching the detector (e.g. a charge-coupled device (CCD) camera). Conventional fluorescence images obtained using this type of microscope, however, suffer from a significant amount of out-of-focus light, which originates from different axial image planes within the sample, but still reaches the detector. The result is a significant decrease in the overall contrast of the acquired image [40].

In order to alleviate this problem, a confocal microscope is used where small aperture ($\sim$100 μm) pinholes are placed in a confocal arrangement on the excitation and detection paths to spatially filter the fluorescence emission from out-of-focus planes. This arrangement permits imaging of light from a single focal plane and the focus can be changed to allow optical sectioning imaging within a 3-dimensional (3D) sample.

The confocal optical geometry allows the light that is in focus at the image plane to be focused within the small pinhole aperture and therefore reach the detector. In contrast, light emanating from out-of-focus image planes will not be in focus at the detection pinhole and will therefore be blocked from reaching the detector (see Fig. 1.7). In modern confocal laser scanning microscopy, a laser is used for excitation and the beam is focused through the objective lens and the confocal geometry to achieve a tiny diffraction limit focal volume. The beam focus is raster scanned point-by-point across the sample and the fluorescence excited sequentially at each point is collected and focused onto a point detector (e.g photomultiplier tube (PMT)) to build up an image of N_x by N_y pixles. The resulting optical sectioning offered by the confocal laser scanning microscope (CLSM) set-up described above, has made confocal fluorescence imaging the tool of choice for imaging relatively thick biological specimens. In addition, the CLSM set-up is easily modified for the excitation and detection of two spectrally distinct fluorophores, which enables fluorescence from two separate molecules of interest to be monitored simultaneously.

Most of the advantages that are provided by confocal imaging over conventional fluorescence microscopy have only been realized commercially in the past twenty years, although they were first proposed by Marvin Minsky in his 1957 patent application. These include, reduced blurring within the image due to out-of-focus light, in addition to a 30% increase in both lateral and axial resolution for a lens of a given numerical aperture (NA) (0.16 μm and 0.65 μm respectively for NA = 1.4) [41], increased signal-to-noise (S/N) ratios, and the possibility of z-scanning for effective 3D imaging of thick samples.

Only with the rapid development of laser technology and digital imaging in the early 1970's and 80's did Minsky's vision for the confocal microscopy culminate in the commercial CLSM found in many laboratories throughout the world today (see [40] for a review).

Another mode of fluorescence microscopy is called total internal reflection fluores-

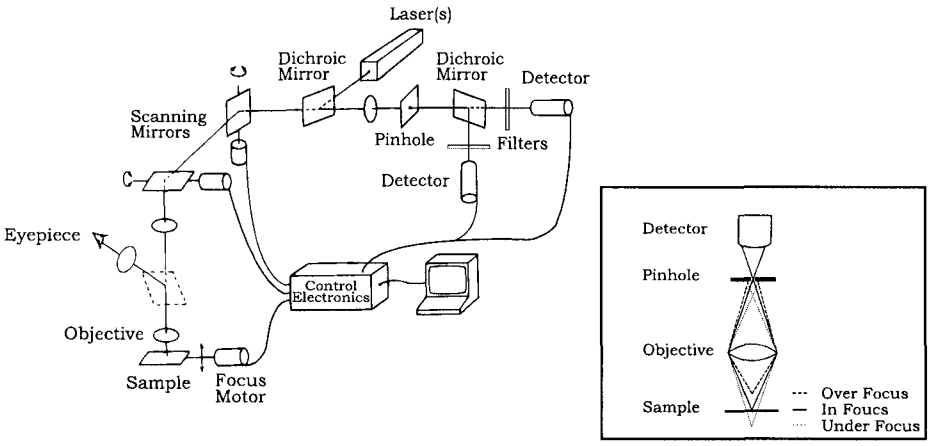

Figure 1.7: Multiple laser lines can be used to raster scan across the sample and excite two spectrally distinct fluorophores. The emitted fluorescence is collected with the same objective used to focus the excitation light and a pinhole is used to reject out-of-focus fluorescence emission. The emitted light is separated by a dichroic mirror, filtered and detected in two different detection channels. Typical excitation wavelengths are the 488 and 514 nm lines of the Argon laser and the 633 nm line of the Helium-Neon (HeNe) laser. Photo multiplier tubes (PMTs) are generally used for the detection of emitted photons and the subsequent conversion to an electrical signal. Shown in the inset is a simplified diagram of the optical path of the emitted fluorescence to illustrate the optical sectioning ability of the confocal pinhole. Adapted from [40].

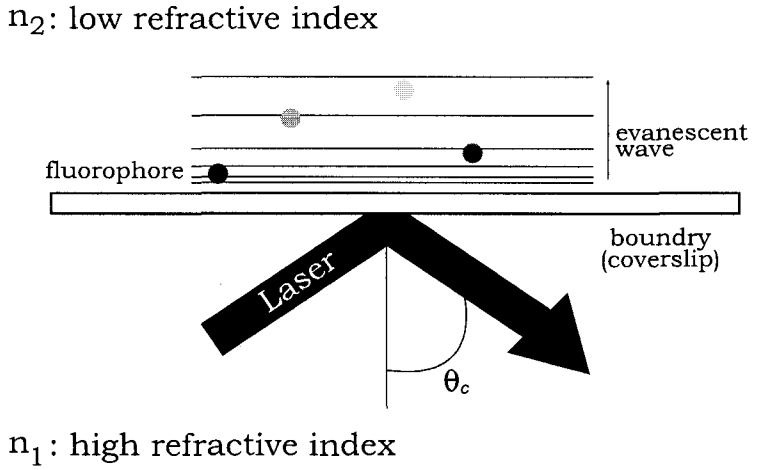

Figure 1.8: Total internal reflection fluorescence (TIRF) microscopy. A evanescent wave is produced at the interface between a high and low refractive index medium. The wave decays exponentially as a function of the distance from the interface, and can be used to excite fluorescent molecules that are present at small distances from the interface (< 100 nm) in the low refractive index medium.

cence (TIRF), which employs the excitation of fluorophores with an evanescent wave. This type of radiation is produced when light strikes the interface between a higher refractive index medium and a lower refractive index medium, at angles larger than some critical angle, θ_c (Fig. 1.8). At $\theta \geq \theta_c$, total internal reflection of the light leads to the formation of an evanescent wave that propagates into the medium of lower refractive index, parallel to the interface, but which decays exponentially as a function of the distance away from the surface. This exponential decay in the intensity of the evanescent wave makes total internal reflection an excellent source of excitation for fluorophores that reside in close proximity (< 100 nm) to the boundary between different refractive index media. Only those fluorophores that are close enough to the refractive index interface will be excited by the evanescent wave, which results in small optical sectioning of the sample [42].

In TIRF microscopy, an objective lens can be used to focus a laser onto a glass coverslip at angles greater than θ_c, producing an evanescent wave that propagates into a cell sample on the opposing side of the coverslip. The objective lens can then be used to collect the resulting fluorescence emission, and a CCD camera can be used to detect the emitted fluorescence photons. This TIRF microscopy set-up has been used extensively to study the basal membrane of living cells, which is an active site for many of the proteins involved in cellular adhesion and migration, and many other cell signaling processes [43, 44]. TIRF microscopy, as compared to other fluorescence microscopy techniques, results in better isolation of the signal from fluorescently tagged proteins in the plasma membrane from that of the same proteins in the cytosol.

Fluorescence microscopy techniques have become an essential tool for studying specific fluorescently tagged biomolecules in living cells. However, in order to apply this sensitive tool to a wide variety of different macromolecules in cells, specific fluorescence labeling methods are required that will tag the molecule of interest, but will not affect its biological functionality.

1.6 Fluorescence Labeling

Some cellular molecules are inherently fluorescent (intrinsic fluorescence), such as the amino acid tryptophan and its indolamine derivatives, and several proteins found in connective tissues like collagen, fibrillin and elastin. However, the contrast of the resulting fluorescence signal is generally quite low for the purposes of most studies, as well, specific imaging of other components is usually desired. In fact, autofluorescence originating from these types of species typically results in increased background signals during cellular imaging. In order to increase the contrast and the range of experiments that can be performed, fluorescent probes are introduced to specific targets within the cell (extrinsic probes). Organic dyes [45], fluorescent proteins [46], as well as inorganic, semi-conductor quantum dots [47] have all been used to label specific molecules within living cells. The two most common labeling techniques involve the use of fluorescently tagged antibodies to label macromolecules of interest as well as genetically encoded fluorescent protein fusion constructs such as the green fluorescent protein (GFP), both of which will be described in the next sections.

1.6.1 Immunofluorescence Labeling

An animal's ability to locate, neutralize and eventually eliminate foreign invaders (like viruses) from the body is an extremely important task that is essential to its continuing survival. Specialized white blood cells called lymphocytes, which are part of the immune system, are the cells responsible for adapting to the constant barrage of potentially infectious organisms. It is imperative, therefore, that the lymphocytes be able to alter their response specifically based on the molecular surface properties of the foreign species that are mounting an attack at any particular time. One mechanism to cope with these fast-changing threats posed by foreign bacterial or viral invaders is by secretion of glycoproteins called antibodies or immunoglobulins, which bind to target antigens on the surface of the invaders in a highly specific manner. Several mechanisms exist that result in mutations of the antigen binding site to ensure the

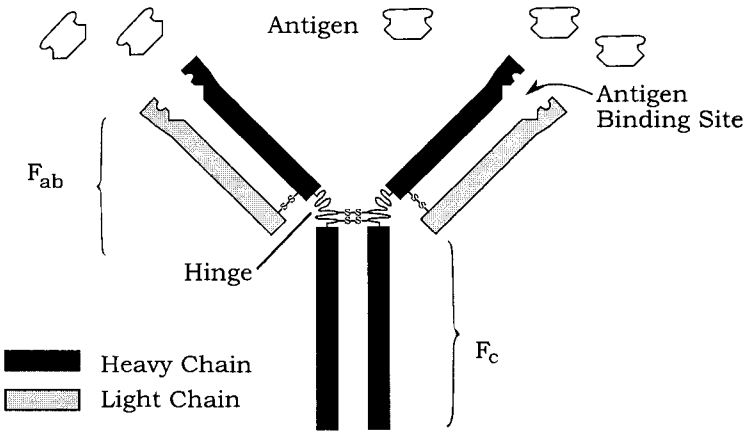

Figure 1.9: The antibody IgG molecule is composed of two pairs of polypeptides held together by disulfide bridges and noncovalent interactions. Two identical antigen binding sits are found at one end of the F_{ab} fragment, which is separated by a flexible hinge from the F_c region responsible for immune cell regulation.

necessary ability to adapt to many different target molecules.

Several classes of antibodies exist, all of which share a similar, bivalent Y-shaped structure. Antibodies of the IgG class consist of two smaller proteins called the light chains (~25 kDa), and two identical polypeptide heavy chains (~55 kDa), held together by disulfide bridges and noncovalent interactions (Fig. 1.9). The arms of the Y-shaped molecule are referred to as the F_{ab} fragments, the ends of which form two identical antigen binding sites. The base of the antibody molecule, or F_c fragment, is responsible for the regulation of various cells of the immune system and has a relatively constant amino acid sequence over a large range of antibodies. A hinge region separates the F_{ab} and F_c domains and provides important flexibility to the antibody for accommodating antigen binding. The remaining four isotypes of antibodies found in mammals are composed of higher oligomers of the same Y-shaped IgG monomer [48].

Antibody proteins that bind specifically to virtually any antigen can be produced in almost unlimited quantities and can be chemically linked to a fluorescent dye, which is the reason why immunolabeling has developed into such a common fluorescence labeling technique. The plasma cells of the immune system that are responsible for

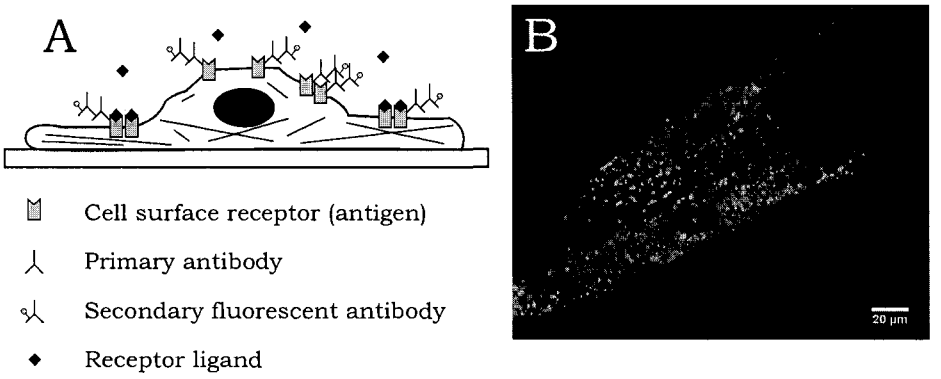

Figure 1.10: (A) Schematic diagram depicting the indirect immunofluorescence labeling procedure. Not drawn to scale. (B) CLSM fluorescence image of fluorescein isothiocyanate (FITC) labeled platelet derived growth factor receptor-β (PDGF-β) in human foreskin fibroblast cells (AG01523). Primary mouse IgG's were used to selectively bind to the PDGF-β receptor, which were then labeled with FITC conjugates of a goat-anti-mouse IgG.

the secretion of antibodies can be readily isolated from an animal that was subjected to a foreign antigen, but cannot be grown in culture unless they are fused with a myeloma tumor cell [49]. The resulting hybridoma cells, however, can be grown in culture indefinitely and will continue to produce large amounts of the desired antibody. Antibodies produced in this manner are monoclonal, that is, they were derived from a single parent cell, and are all identical and recognize one single antigen molecule.

Direct immunofluorescence labeling consists of producing monoclonal antibodies for a desired target molecule as described above, and subsequent covalent attachment of a desired fluorescent dye molecule. Typically, however, an indirect labeling approach is taken, which employs a non-fluorescent primary antibody specific to the molecule of interest, and a secondary, fluorescently labeled antibody that binds specifically to the primary antibody (Fig. 1.10). Indirect immunostaining is a much more flexible alternative to direct labeling because the secondary antibodies are usually species specific, and will therefore bind any primary IgG that was originally produced in a given species. This means that a single, fluorescently tagged secondary antibody can be used to label a large array of primary antibodies, regardless of the

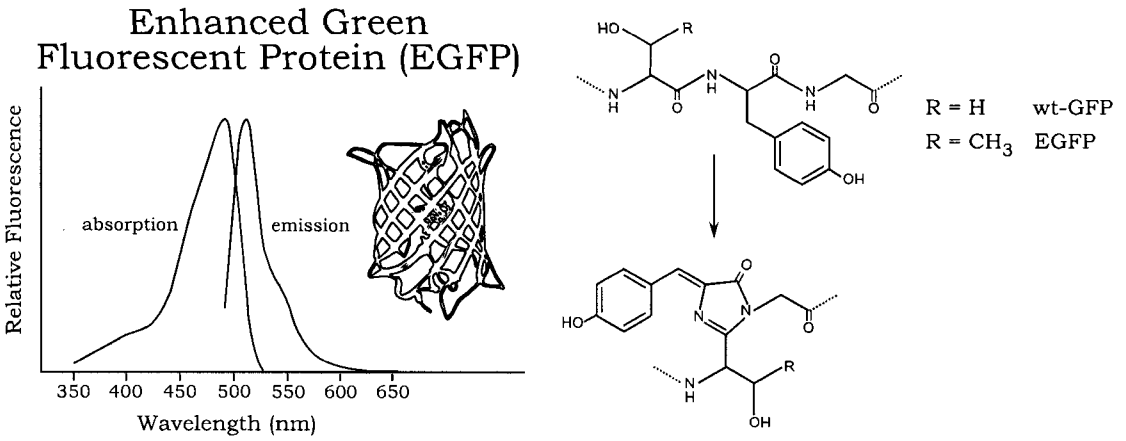

Figure 1.11: Enhanced green fluorescent protein (EGFP) is most efficiently excited at 488 nm and maximum emission occurs at 508 nm. The β-barrel structure of the molecule is important in mediating the autocatalytic reaction that results in the formation of a fluorescent species, which is folded in the middle of the barrel, and is shown on the right side of the figure. In EGFP, the hydrogen of wild-type GFP (wt-GFP) is substituted for a methyl group (serine65 to threonine65). Adapted from [56].

particular antigen target. In certain cases, greater signal is obtained with indirect immunolabeling due to the fact that multiple secondary antibodies can bind to a single primary antibody. Immunofluorescence labeling has been applied to both fixed and living cells in order to identify an essential protein in maintaining polarity in epithelial cells [50], and for the quantitation of retroviruses [51], respectively, in addition to countless other applications.

1.6.2 *Genetically Encoded Fluorescent Proteins*

Beginning with the purification of the green fluorescent protein (GFP) by Osamu Shimomura from the crystal jellyfish, *Aequorea victoria*, in the early 1960's [52, 53], and culminating with the cloning [54] and expression of the fluorescent protein in bacteria [55] over 30 years later, GFP and its derivatives have become some of the most widely employed reporter molecules in molecular biology today.

The GFP is composed of an 11-stranded β-barrel that forms a hollow cylinder and surrounds an irregular α-helix containing the fluorescence moiety [57, 58]. The fluorophore itself is formed from an autocatalytic cyclization reaction of the amino

acid residues serine65-tyrosine66-glycine67 at the center of the β-barrel structure [59](Fig. 1.11). Interestingly, this amino acid sequence is found in numerous proteins, none of which demonstrate fluorescent properties, which is an indication of the importance of the β-barrel structure in forming and protecting the luminescent nature of the protein. Point mutations of *Aequorea* wild-type GFP (wt-GFP, F64L/S65T) resulted in a brighter, enhanced form of GFP (EGFP) [60, 61] as well as a series of fluorescent proteins with emission peaks that spanned a large portion of the visible spectrum from blue to yellow [62]. Recent advances have made the red part of the spectrum accessible using proteins derived from several species of coral [63].

One important property of GFP that has made it such a useful labeling tool for cellular experiments is the overall stability of the fluorophore as a direct result of its tertiary structure. Typical fluorescence quenchers such as halides and oxygen have little to no effect on the fluorescence properties of GFP [64]. Common proteases, which are enzymes that cleave proteins by peptide bond hydrolysis, have no effect on GFP, even under optimal conditions for the hydrolysis reaction [65]. Perhaps most importantly, cellular fixatives such as paraformaldehyde that are commonly used to preserve tissues for imaging do not alter the fluorescent properties of GFP even over long periods of time [55]. Other useful properties of GFP include a high quantum yield (wt-GFP $\sim$0.8, EGFP $\sim$0.60)[56], relatively small size (27kDa, $\sim$3 x 4 nm)[58] and the ability to create and express chimeric proteins, *in vivo*, that consist of GFP fused to the end of a particular protein of interest.

Well established transfection procedures are used to generate GFP-fusion proteins by introducing into cells foreign DNA molecules that encode for an amino acid sequence of a protein target as well as the 238 amino acids of GFP. Once inside the cell, the DNA is transcribed and translated into protein by the normal cellular mechanisms. The result is expression of a single polypeptide composed of the protein of interest with an attached GFP [66, 67]. Many different fluorescent constructs have been developed, which were shown to be functionally unaltered by fusion to fluores-

cent proteins, and were therefore used in subsequent experiments. The transfection may be performed in a transient manner such that the foreign gene is expressed by the cell, but the DNA (and fluorescently tagged protein) is eventually lost when the cell divides during mitosis. Stable transfections may also be carried out in which the foreign DNA is actually incorporated into the nuclear genome of the cell and therefore results in indefinite expression of the fluorescent fusion protein as long as the cells continue to proliferate.

1.7 Fluorescence Microscopy Colocalization Measurements

To date, most approaches for measuring interacting cellular constituents based on fluorescence microscopy require the labeling of two component species with different fluorophores and imaging the emissions in two detection channels. The two detection channel images are then analyzed for the presence of colocalized signals, that is, spatially overlapping signals within images collected on the separate detection channels. The measurement of a high degree of colocalization indicates close proximity of the two labeled species, and therefore suggests a nonrandom interaction between the two labeled molecules of interest.

Several different approaches to two channel image analysis can be employed to measure the colocalization of biomolecules. The simple overlay of RGB microscopy images for qualitative assessments of colocalization has been, and continues to be, a common practice in many biological studies [68, 69]. Frequently, images of green and red fluorophores labeling different species are overlapped and assessed for the predominance of yellow pixels in the combined image, which, to a first approximation, indicates the presence of interacting species. Overlaying images is a relatively quick and straightforward method for detecting interactions between molecules, but it is strictly qualitative and can be misleading due to the relatively large size of the optical microscopy diffraction resolution limit focus (~250 nm) relative to the size of the macromolecules of interest (~5-10 nm).

Numerous strategies have been employed in the past to implement a more quantitative measure of colocalization. For example, the creation of a binary image mask of fluorescein labeled mitochondria together with images of Texas Red labeled hexokinase, led to the measurement of ~70% colocalization between the enzyme and the organelle [70]. The association of poly(A) RNA with different cytoskeletal elements of human diploid fibroblast cells was quantified by detailed statistical analysis of pixel intensity distributions [71]. The analysis of fluorescence intensity second-order histograms and improved color look-up tables was proposed for the characterization of colocalization in two detection channel fluorescence images, as well as any image acquisition artifacts affecting the measurement [72]. Similar histograms were employed by Li et al. but plotted as a function of the covariance between the two detection channels, which led to sensitive visual cues to the type of colocalization present between components at a presynaptic nerve terminal [73].

More recently, single particle fluorescence imaging techniques were used to quantify colocalization by statistical analysis of either the overlap integral [74], or via estimation of the intermolecular distance by point spread function (PSF) centroid fitting [75, 76], for single particles within images. Nevertheless, single particle methods require very sensitive detectors and, more importantly, are not feasible at higher molecular densities where the individual particles cannot be optically resolved within the images.

Fluorescence resonance energy transfer (FRET) occurs without the appearance of a photon via long-range dipole-dipole interactions between a donor and an acceptor molecule. Energy transfered from the donor molecule will then lead to either fluorescence emission by the acceptor or relaxation to the ground state by non-radiative mechanisms. The rate, k_T at which energy is transfered from the donor to the acceptor depends on the spectral overlap of the two fluorophores (donor emission with acceptor excitation), the orientation of the donor/acceptor transition dipoles, and is extremely sensitive to the distance between the two molecules ($k_T \ \alpha \ r^{-6}$). The

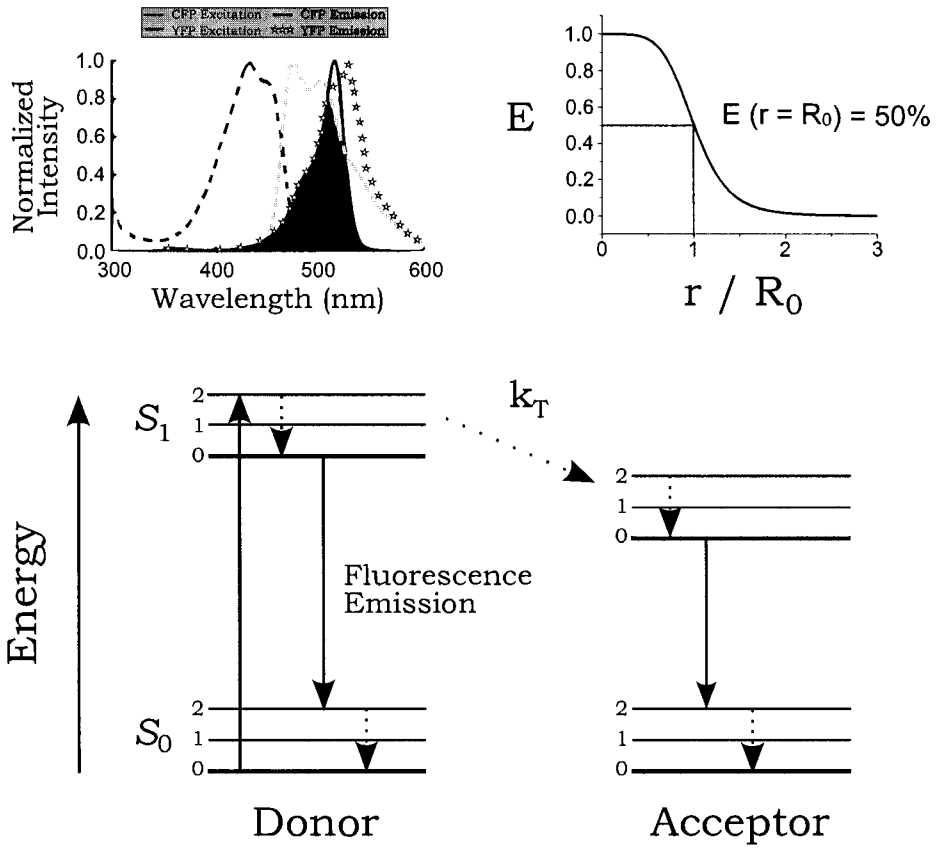

Figure 1.12: The fluorescence emission spectrum of cyan fluorescent protein (CFP) significantly overlaps with the excitation spectrum of yellow fluorescent protein (YFP) as shown in the shaded area of the top left panel. This overlap can lead to non-radiative energy transfer at a rate, k_T, from excited CFP donor molecules to YFP acceptor molecules followed by subsequent fluorescence emission of the acceptor. The efficiency, E, of fluorescence resonance energy transfer (FRET) is a measure of the fraction of photons absorbed by the donor that are transfered to the acceptor. The FRET efficiency has an inverse sixth power dependence on the separation distance, r, between the two fluorophores, and the Förster radius, R_0, for a donor/acceptor pair is defined as the distance at which the energy transfer efficiency is 50%. R_0 for CFP/YFP is ~5 nm, and typically ranges from 2-6 nm for most donor/acceptor pairs.

Förster radius, R_0, is a convenient constant that describes the spectral overlap and dipole-dipole orientation of a particular donor/acceptor pair, and is defined as the distance at which 50% of the donor molecules decay by resonance energy transfer to the acceptor, while the other 50% decay by the normal radiative and non-radiative pathways. The distance sensitivity of FRET has been exploited to measure short ($2 - 10$ nm) inter- and intramolecular distances on the order of the size of many biological macromolecules, as well as the distance between protein subunits, and consequently, has proven to be an effective measure of molecular interactions [77, 78], protein conformational changes [79], and the distance between two sites of interest on a protein [80]. Besides the useful distance sensitivity on biological spatial scales, FRET has also found widespread use in biological experiments due to the ability to accurately predict the extent of energy transfer from the spectral properties of the two fluorophores, and the fact that the FRET between these two fluorophores is typically unaffected by other molecules within a cellular environment.

FRET is typically quantified as the fraction of photons absorbed by the donor that are transferred to the acceptor. This fraction is defined as the FRET efficiency, E, and is given by the ratio of the energy transfer rate to the total decay rate of the donor in the presence of the acceptor. The most common experimental method to determine the FRET efficiency is by measuring the extent to which the donor fluorescence emission (or lifetime) is quenched by the presence of an acceptor molecule. In an imaging experiment, this can be accomplished by recording the fluorescence signal from the donor in the presence of the acceptor, followed by the irreversible photobleaching of the acceptor molecule and measuring the resulting increase in donor emission [81]. Similarly, the FRET efficiency can be determined by the enhanced acceptor emission observed in the presence of donor molecules. This method will lead to the same FRET efficiency as that measured by donor quenching, but is more susceptible to error due to donor fluorescence bleed-through into the acceptor detection channel, as well as the direct excitation of the acceptor by the donor excitation

source [82]. Several other experimental approaches to quantify FRET efficiencies in fluorescence microscopy images have been proposed to minimize the effects that can lead significant errors in the determination of E (see [83] for review).

While the sensitivity of FRET to the separation distance between fluorophores can essentially serve as an informative spectroscopic ruler, it may also be a disadvantage in cases where colocalized structures are composed of large multi-protein complexes so that the distance scale exceeds the Förster radius where the FRET efficiency begins to decrease rapidly with distance. In addition, most FRET experiments in cells have shown limited success in measuring interaction distances between molecules, and are not easily adaptable to quantification of the fraction, or numbers, of interacting molecules [84], and therefore, most cellular FRET applications have simply acted as sensitive diagnostic tests for the presence of interactions.

Two channel fluorescence cross-correlation spectroscopy (FCCS) is capable of measuring interacting fluorescently tagged macromolecules via temporal cross-correlation analysis of fluorescence intensity fluctuations collected from a small microscopic (<1 fL) observation volume defined by the beam focus of an excitation laser(s) [85]. Intensity fluctuations arising from changes in fluorophore concentration within the beam focus are recorded simultaneously in two channels and correlated in time to reveal transport properties and number densities of interacting and noninteracting species. Image cross-correlation spectroscopy (ICCS) relies on the same principles as FCCS, but utilizes spatial correlation analysis of intensity fluctuations in fluorescence images collected via laser scanning microscopy. It can access transport dynamics on slower timescales ($D = 0 - 10^{-10}$ cm^2/s) such as those often encountered for cell membrane proteins or immobilized proteins in chemically fixed cells [86, 87]. Until now, the dynamic range and accuracy of ICCS has not been investigated and the application to measure interactions within single, two channel images has not been extensively investigated. Both FCCS and ICCS will be covered in more detail in the next chapter.

Several statistical measures between images have been used to measure colocal-

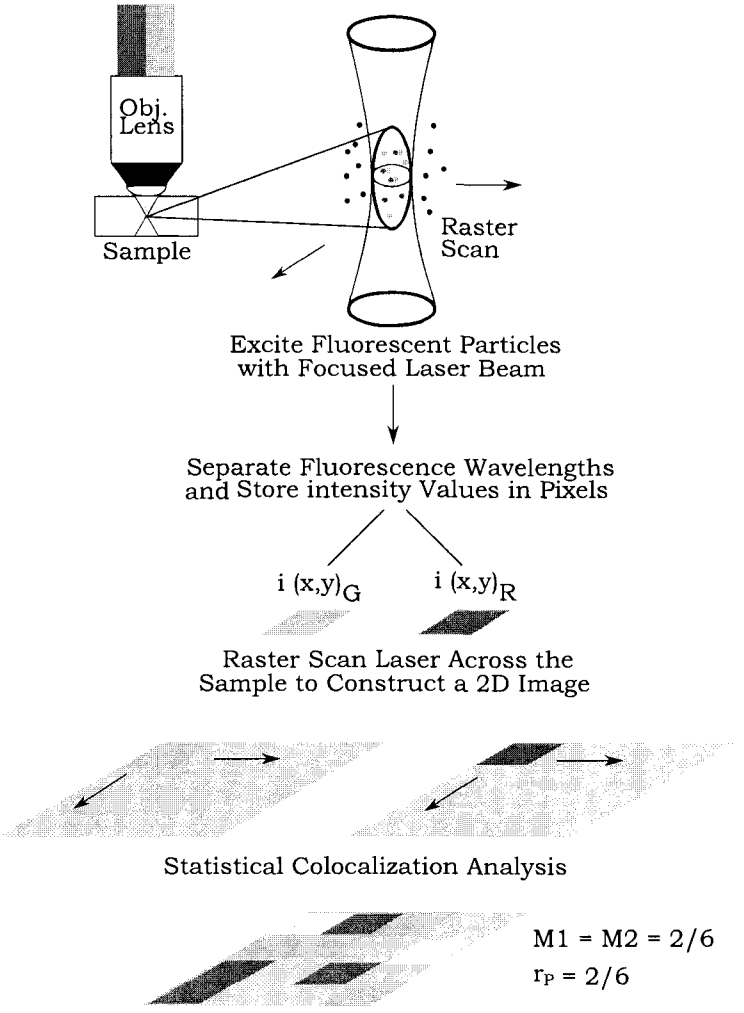

Figure 1.13: Each pixel pair in images recorded in two detection channels, $i(x,y)_G$ and $i(x,y)_R$, is recorded by measuring the emitted fluorescence that results from excitation of fluorescent dyes within a diffraction-limited laser beam focus. Two fluorescence images are acquired by raster scanning two aligned excitation laser beams across the sample, and separating the resulting fluorescence into the two spectrally resolved detection channels. The two images can then be analyzed for the presence of colocalized pixels by calculation of coefficients, $M1$ and $M2$, which are calculated from the ratio of the pixel intensities that are deemed colocalized ($i(x,y)_G$ & $i(x,y)_R > i_{Threshold}$ to the total intensity for a given detection channel [88] (Eq. 2.22). Pearson's correlation coefficient, r_P, is a single-parameter measure of the covariance between two signals and can be used as a measure of colocalization in dual-color fluorescence images when the concentrations of particles in each detection channel image are equivalent [89] (Eq. 2.23).

ization between two channel images. Pearsons correlation coefficient, r_P (Eq. 2.23), is a measure of the covariance between two signals and was first applied to measure colocalization within two channel fluorescence images of biological samples by Manders and co-workers, but was limited to samples with approximately equal number densities detected in each channel [89]. To overcome this limitation, Manders and co-workers introduced a method to calculate colocalization coefficients, $M1$ and $M2$ (Fig. 1.13), which has become the most widespread approach for quantitative colocalization measurements via fluorescence microscopy [88]. The authors demonstrated, using the analysis of simulation and fixed cell images, that $M1$ and $M2$ were sensitive measures of the degree of colocalization in doubly labeled systems and were therefore particularly useful when the two species of interest differed in total number. The correct identification of colocalized pixels pairs is essential to the accurate evaluation of $M1$ and $M2$, and is accomplished by defining a threshold value for each detection channel. Specific pixels will contribute to the colocalized signal, only if both channel intensities are above their respective threshold values. For a particular channel, the ratio of the colocalized pixel intensities to the total pixel intensities, define the interacting fraction for that species. Recent work by Costes and co-workers has shown that automatic determination of the colocalization threshold is possible by testing a variable intensity threshold and finding the highest intensity value for which evaluation of r_P for pixels with intensities below this threshold yield an r_P value of zero [90]. Their automatic colocalization algorithm proved to be a fast, reliable method for calculating $M1$ and $M2$ and eliminated ambiguity in threshold determination. The method, however, was not evaluated at higher particle densities or for different density ratios detected between channels.

Similar to ICCS analysis, spatial correlation techniques that measure r_P as a function of spatial lag in one or two dimensions have been applied previously to two channel images, but did not take full advantage of the information contained within the correlation function [91, 92]. Barbarese and co-workers defined a correlation index,

γ, to measure the colocalization of protein translation components in oligodendrocytes using such an approach, but did not determine the amount of colocalization with respect to each detection channel. Defining the amount of colocalization present between two images using a single parameter is often difficult to interpret and cannot fully characterize the system.

The popularity of two detection channel fluorescence image colocalization analyses stems from the developments in fluorescence labeling techniques, confocal imaging and image processing software. In fact, several algorithms, including those for calculating Manders' colocalization coefficients, $M1$ and $M2$, are commercially available, or freely shared, which accounts for why these types of colocalization measurements are so widely used. Most methods, however, have not been rigorously tested, and provide absolutely no indication of failure, which is why it is extremely important to know the limitations of any particular technique before applying it to a given biological system.

Bibliography

[1] R. Hooke. *Micrographia: or, Some physiological descriptions of minute bodies made by magnifying glasses.* J. Martyn and J. Allestry, 1st edition, 1665.

[2] B. Alberts, D. Bray, A. Johnson, J. Lewis, M. Raff, K. Roberts, and P. Walter. *Essential Cell Biology: An introduction to the Molecular Biology of the Cell.* Garland Publishing, Inc., 1998.

[3] L. A. Moran, K. G. Scrimgeour, H. R. Horton, R. S. Ochs, and J. D. Rawn. *Biochemistry.* Prentice-Hall, Inc., 2nd edition, 1994.

[4] J. V. Small, K. Rottner, I. Kaverina, and K. I. Anderson. Assembling an actin cytoskeleton for cell attachment and movement. *Biochimica et Biophysica Acta*, 1404(3):271–281, 1998.

[5] A. J. Ridley, M. A. Schwartz, K. Burridge, R. A. Firtel, M. H. Ginsberg, G. Borisy, J. T. Parsons, and A. R. Horwitz. Cell migration: Integrating signals from front to back. *Science*, 302(5651):1704–1709, 2003.

[6] D. Tomkiewicz, N. Nouwen, and A. J. M. Driessen. Pushing, pulling and trapping - modes of motor protein supported protein translocation. *FEBS Letters*, 581(15):2820–2828, 2007.

[7] B. Hille. *Ion Channels of Excitable Membranes.* Sinauer Associates, Inc., 3rd edition, 2001.

[8] J. A. Pitcher, N. J. Freedman, and R. J. Lefkowitz. G protein-coupled receptor kinases. *Annual Review of Biochemistry*, 67:653–692, 1998.

[9] K. Vuori. Integrin signaling: Tyrosine phosphorylation events in focal adhesions. *J. Membrane Biol.*, 165(3):191–199, 1998.

[10] D. L. Nelson and M. M. Cox. *Lehninger Principles of Biochemistry.* W. H. Freeman, 4th edition, 2004.

[11] D. O. Morgan. *The Cell Cycle: Principles of Control.* New Science Press, Ltd., 2006.

[12] D. G. Nicholls and S. J. Ferguson. *Bioenergetics.* Academic Press, Inc., 3rd edition, 2002.

[13] M. M. Silva, P. H. Rogers, and A. Arnone. A third quaternary structure of human hemoglobin A at 1.7- å resolution. *J. Biol. Chem.*, 267(24):17248–17256, 1992.

[14] B. Alberst, A. Johnson, J. Lewis, M. Raff, K. Roberts, and P. Walter. *Molecular biology of the Cell.* Garlan Science, 4th edition, 2002.

[15] C. J. Marshall. Speificity of receptor tyrosine kinase signaling: Transient versus sustained extracellular signal-regulated kinase activation. *Cell*, 80(2):179–185, 1995.

[16] R. J. Davis. The mitogen-activated protein kinase signal transduction pathway. *The Journal of Biological Chemistry*, 268(20):14553–14556, 1993.

[17] F. Verde, D. J. Wiley, and P. Nurse. Fission yeast *orb*6, a ser/thr protein kinase related to mammalian rho kinase and mytonic dystrophy kinase, is required for maintenance of cell polarity and coordinates cell morphogenesis with the cell cycle. *Proc. Natl. Acad. Sci*, 95(13):7526–7531, 1998.

[18] D. Ratner. The interaction of bacterial and phage proteins with immobilized *Escherichia coli* RNA polymerase. *J. Mol. Biol.*, 88:373–383, 1974.

[19] E. M. Phizicky and S. Fields. Protein-protein interactions: Methods for detection and analysis. *Microbiological Reviews*, 59(1):94–123, 1995.

[20] D. P. Lane and L. V. Crawford. T antigen is bound to a host protein in sv40-transformed cells. *Nature*, 278(5701):261–263, 1979.

[21] M. Eisenstein. Identification of associated proteins by coimmunoprecipitation. *Nature Methods*, 2(6):475–476, 2005.

[22] K. H. Young. Yeast two-hybrid: So many interactions, (in) so little time... *Biology of Reproduction*, 58:302–311, 1998.

[23] S. Fields and O.-K. Song. A novel genetic system to detect protein-protein interactions. *Nature*, 340(6230):245–246, 1989.

[24] C.-T. Chien, P. L. Bartel, R. Sternglanz, and S. Fields. The two-hybrid system: A method to identify and clone genes for proteins that interact with a protein of interest. *Proc. Natl. Acad. Sci.*, 88(21):9578–9582, 1991.

[25] P. Uetz, L. Giot, G. Cagney, T. A. Mansfield, R. S. Judson, J. R. Knight, D. Lockshon, V. Narayan, M. Srinivasan, P. Pochart, A. Qureshi-Emili, Y. Li, B. Godwin, D. Conover, T. Kalbfleisch, G. Vijayadamodar, M. Yang, M. Johnston, S. Fields, and J. M. Rothberg. A comprehensive analysis of protein-protein interactions in *Saccharomyces cerevisiae*. *Nature*, 403(6670):623–627, 2000.

[26] G. Forgacs, S. H. Yook, P. A. Janmey, H. Jeong, and C. G. Burd. Role of the cytoskeleton in signaling networks. *J. Cell Sci.*, 117(13):2769–2775, 2004.

[27] C. M. Deane, L. Salwiński, I. Xenarios, and D. Eisenberg. Protein interactions: Two methods for assessment of the reliability of high throughput observations. *Mol. Cell Proteomics*, 1(5):349–356, 2002.

[28] S. Fields. High-throughput two-hybrid analysis. *FEBS journal*, 272(21):5391–5399, 2005.

[29] D. A. Calderwood. Integrin activation. *J. Cell Sci.*, 117(5):657–666, 2004.

[30] R. De Francesco, A. Pastore, G Vecchio, and R. Cortese. Circular dichroism study on the conformational stability of the dimerisation domain of the transcriptional factor LFB1. *Biochemistry*, 30(1):143–147, 1991.

[31] D. Grunwald, M. C. Cardoso, H. Leonhardt, and V. Buschmann. Diffusion and binding properties investigated by fluorescence correlation spectroscopy (FCS). *Current Pharmaceutical Biotechnology*, 6(5):381–386, 2005.

[32] P. Schuck. Reliable determination of binding affinity and kinetics using surface plasmon resonance biosensors. *Curr. Opin. Biotechnol.*, 8(4):498–502, 1997.

[33] M. Doyle. Characterization of binding interactions by isothermal titration microcalorimetry. *Curr. Opin. Biotechnol.*, 8(1):31–35, 1997.

[34] R. W. Kriwacki, J. Wu, G. Siuzdak, and P. E. Wright. Probing protein/protein interactions with mass-spectrometry and isotropic labelling-analysis of the p21/cdk2 complex. *J. Am. Chem. Soc.*, 118(22):5320–5321, 1996.

[35] R. P. Gonçalves, G. Angus, P. Sens, C. Houssin, B. Bartenlian, and S. Scheuring. Two-chamber AFM: probing membrane proteins separating two aqueous compartments. *Nature Methods*, 3(12):1007–1012, 2006.

[36] J. F. W. Herschel. On a case of superficial colour presented by a homogeneous liquid internally colourless. *Phil. Trans. Roy. Soc. (London)*, 135:143–145, 1845.

[37] Joseph R. Lakowicz. *Principles of Fluorescence Spectroscopy.* Springer Science+Business Media, LLC, 3rd edition, 2006.

[38] J. T. Vivian and P. R. Callis. Mechanisms of tryptophan fluorescence shifts in proteins. *Biophys. J.*, 80(5):2093–2109, 2001.

[39] D. M. Jameson and W. H. Sawyer. Fluorescence anisotropy applied to biomolecular interactions. *Methods Enzymol.*, 246:283–300, 1995.

[40] J. B. Pawley. *Handbook of Biological Confocal Microscopy.* Springer Science+Business Media, LLC, 3rd edition, 2006.

[41] A. Diaspro. *Confocal and Two-Photon Microscopy: Foundations, Applications, and Advances.* Wiley-Liss, Inc., 2002.

[42] D. Axelrod. Total internal reflection fluorescence microscopy in cell biology. *Traffic*, 2(11):764–774, 2001.

[43] A. D. Douglass and R. D. Vale. Single-molecule microscopy reveals plasma membrane microdomains created by protein-protein networks that exclude or trap signaling molecules in T cells. *Cell*, 121(6):937–950, 2005.

[44] E. J. ezratty, M. A. Partridge, and G. G. Gundersen. Microtubule-induced focal adhesion disassembly is mediated by dynamin and focal adhesion kinase. *Nat. Cell Biol.*, 7:581–590, 2005.

[45] B. N. G. Giepmans, S. R. Adams, M. H. Ellisman, and R. Y. Tsien. The fluorescent toolbox for assessing protein location and function. *Science*, 312(5771):217–224, 2006.

[46] M. Zimmer. Green fluorescent protein (GFP): Applications, structure, and related photophysical behavior. *Chem Rev.*, 102(3):759–781, 2002.

[47] X. Michalet, F. F. Pinaud, L. A. Bentolila, J. M. Tsay, S. Doose, J. J. Li, G. Sundaresan, A. M. Wu, S. S. Gambhir, and S. Weiss. Quantum dots for live cells, *in Vivo* imaging, and diagnostics. *Science*, 307(5709):538–544, 2005.

[48] E. Harlow and D. Lane. *Antibodies: A laboratory manual.* Cold Spring Harbor Laboratory Press, 1998.

[49] G. Köhler and C. Milstein. Continuous cultures of fused cells secreting antibody of predefined specificity. *Nature*, 256(5517):495–497, 1975.

[50] R. Kroschewski, A. Hall, and I. Mellman. Cdc42 controls secretory and endocytic transport to the basolateral plasma membrane of MDCK cells. *Nature Cell Biology*, 1(1):8–13, 1999.

[51] M. Sitbon, J. Nishio, K. Wehrly, D. Lodmell, and B. Chesebro. Use of a focal immunofluorescence assay on live cells for quantitation of retroviruses: Distinction of host range classes in virus mixtures and biological cloning of dual-tropic murine leukemia viruses. *Virology*, 141(1):110–118, 1985.

[52] O. Shimomura, F. Johnson, and Y. Saiga. Extraction, purification and properties of aequorin, a bioluminescent protein from the luminous hydromedusan, *Aequorea*. *Journal of Cellular and Comparative Physiology*, 59(3):223–239, 1962.

[53] H. Morise, O. Shimomura, F. Johnson, and J. Winant. Intermolecular energy transfer in the bioluminescent system of *Aequorea*. *Biochemistry*, 13(12):2656–2662, 1974.

[54] D. Prasher, V. Eckenrode, W. Ward, F. Prendergast, and M. Cormier. Primary structure of the *Aequorea victoria* green-fluorescent protein. *Gene*, 111(2):229–233, 1992.

[55] M. Chalfie, Y. Tu, G. Euskirche, W. Ward, and D. Prasher. Green fluorescent protein as a marker for gene expression. *Science*, 263(5148):802–805, 1994.

[56] R. Y. Tsien. The Green Fluorescent Protein. *Annu. Rev. Biochem.*, 67:509–544, 1998.

[57] M. Ormö, A. B. Cubitt, K. Kallio, L. A. Gross, R. Y. Tsien, and S. J. Remington. Crystal structure of the *Aequorea victoria* green fluorescent protein. *Science*, 273(5280):1392–1395, 1996.

[58] F. Yang, L. G. Moss, and G. N. Phillips Jr. The molecular structure of green fluorescent protein. *Nature Biotechnology*, 14(10):1246–1251, 1996.

[59] C. W. Cody, D. C. Prasher, W. M. Westler, F. G. Prendergast, and W. W. Ward. Chemical structure of the hexapeptide chromophore of the *Aequorea* green-fluorescent protein. *Biochemistry*, 32(5):1212–1218, 1992.

[60] R. Heim, A. B. Cubitt, and R. Y. Tsien. Improved green fluorescence. *Nature*, 373(6516):663–664, 1995.

[61] G. H. Patterson, S. M. Knobel, W. D. Sharif, S. R. Kain, and D. W. Piston. Use of the green fluorescent protein and its mutants in quantitative fluorescence microscopy. *Biophys. J.*, 73(5):2782–2790, 1997.

[62] R. Heim and R. Y. Tsien. Engineering green fluorescent protein for improved brightness, longer wavelengths and fluorescence resonance energy transfer. *Current Biology*, 6(2):178–182, 1996.

[63] R. E. Campbell, O. Tour, A. E. Palmer, P. A. Steinbach, G. S. Baird, D. A. Zacharias, and R. Y. Tsien. A monomeric red fluorescent protein. *Proc. Natl. Acad. Sci.*, 99(12):78777882, 2002.

[64] B. Rao, M. Kemple, and F. Prendergast. Proton nuclear magnetic resonance and fluorescence spectroscopic studies of segmental mobility in aequorin and a green fluorescent protein from *Aequorea forskalea*. *Biophys. J.*, 32(1):630–632, 1980.

[65] S. H. Bokman and W. W. Ward. Renaturation of *Aequorea* green-fluorescent protein. *Biochem. Biophys. Res. Commun.*, 101(4):1372–1380, 1981.

[66] R. Rizzuto, M. Brini, P. Pizzo, M. Murgia, and T. Pozzan. Chimeric green fluorescent protein as a tool for visualizing subcellular organelles in living cells. *Current Biology*, 5(6):635–642, 1995.

[67] J. D. Plautz, R. N. Day, G. M. Dailey, S. B. Welsh, J. C. Hall, S. Halpain, and S. A. Kay. Green fluorescent protein and its derivatives as versatile markers for gene expression in living drosophila melanogaster, plant and mammalian cells. *Gene*, 173(1):83–87, 1996.

[68] C. Humbert, M. S. Santiseban, Y. Usson, and M. Robert-Nicoud. Intranuclear colocation of newly replicated DNA and PCNA by simultaneous immunofluorescent

labeling and confocal microscopy in MCF-7 cells. *J. Cell Sci.*, 103(1):97–103, 1992.

[69] S. E. Ward, C. Martinez, C. Vaccara, J. Zhou, Q. Tang, and R. J. Ober. From sorting endosomes to exocytosis: Association of Rab4 and Rab11 GTPases with the Fc receptor, FcRn, during recycling. *Mol. Biol. Cell*, 16(4):2028–2038, 2005.

[70] R. M. Lynch, K. E. Fogarty, and F. S. Fay. Modulation of hexokinase association with mitochondria analyzed with quantitative three-dimensional confocal microscopy. *J. Cell Biol.*, 112(3):385–395, 1991.

[71] K. L. Taneja, L. M. Lifshitz, F. S. Fay, and R. H. Singery. Poly(A) RNA codistribution with microfilaments: Evaluation by in situ hybridization and quantitative digital imaging microscopy. *J. Cell Biol.*, 119(5):1245–1260, 1992.

[72] D. Demandolx and J. Davoust. Multicolor analysis and local image correlation in confocal microscopy. *J. Microsc.*, 185(1):21–36, 1997.

[73] Q. Li, A. Lau, T. J. Morris, L. Guo, C. B. Fordyce, and E. F. Stanley. A syntaxin 1, G_{α_o} and N-type calcium channel complex at a presynaptic nerve terminal: Analysis by quantitative immunocolocalization. *J. Neurosci.*, 24(16):4070–4081, 2004.

[74] I. E. G. Morrison, I. Karakikes, R. E. Barber, N. Fernandez, and R. Cherry. Detecting and quantifying colocalization of cell surface molecules by single particle fluorescence imaging. *Biophys. J.*, 85(6):4110–4121, 2003.

[75] W. Trabesinger, B. Hecht, U. P. Wild, G. J. Schutz, H. Schindler, and Th. Schmidt. Statistical analysis of single-molecule colocalization assays. *Anal. Chem.*, 73(6):1100–1105, 2001.

[76] I. Koyama-Honda, K. Ritchie, T. Fujiwara, R. Lino, H. Murakoshi, R. S. Kasai,

and A. Kusumi. Fluorescence imaging for monitoring the colocalization of two single molecules in living cells. *Biophys. J.*, 88(3):2126–2136, 2005.

[77] A. A. Angers, A. Salahpour, E. Joly, S. Hilairat, D. Chelsky, M. Dennis, and M. Bouvier. Detection of β_2-adrenergic receptor dimerization in living cells using bioluminescence resonance energy transfer (BRET). *Proc. Natl. Acad. Sci. USA*, 97(7):3684–3689, 2000.

[78] C. Janetopoulos, T. Jin, and P. Devreotes. Receptor-mediated activation of heterotrimeric G-proteins in living cells. *Science*, 291(5512):2408–2411, 2001.

[79] T. Heyduk. Measuring protein conformational changes by FRET/LRET. *Curr. Opin. Biotechnol.*, 13(4):292–296, 2002.

[80] Q. Qu and F. J. Sharom. FRET analysis indicates that the two ATPase active sites of the P-glycoprotein multidrug transporter are closely associated. *Biochemistry*, 40(5):1413–1422, 2001.

[81] A. K. Kenworthy, N. Petranova, and M. Edidin. High-resolution FRET microscopy of cholera toxin B-subunit and GPI-anchored proteins in cell plasma membranes. *Mol. Biol. Cell*, 11(5):1645–1655, 2000.

[82] J. van Rheenen, M. Langeslag, and K. Jalink. Correcting confocal acquisition to optimize imaging of fluorescence resonance energy transfer by sensitized emission. *Biophys. J.*, 86:25172529, 2004.

[83] E. A. Jares-Erijman and T. M. Jovin. FRET imaging. *Nat. Biotech.*, 21(11):1387–1395, 2003.

[84] A. Hoppe, K. Christensen, and J. A. Swanson. Fluorescence resonance energy transfer-based stoichiometry in living cells. *Biophys. J.*, 83(6):3652–3664, 2002.

[85] P. Schwille, F.-J. Myer-Almes, and R. Rigler. Dual color fluorescence cross-correlation spectroscopy for multicomponent diffusional analysis in solution. *Biophys. J.*, 72(4):1878–1886, 1997.

[86] N. O. Petersen, P. L. Hoddelius, P. W. Wiseman, O. Seger, and K. E. Magnusson. Quantitation of membrane receptor distributions by image correlation spectroscopy: Concept and application. *Biophys. J.*, 65(3):1135–46, Sep 1993.

[87] P. W. Wiseman and N. O. Petersen. Image correlation spectroscopy. II. Optimization for ultrasensitive detection of preexisting platelet-derived growth factor-beta receptor oligomers on intact cells. *Biophys. J.*, 76(2):963–77, Feb 1999.

[88] E. M. M. Manders, F. J. Verbeek, and J. A. Aten. Measurement of co-localization of objects in dual color confocal images. *J. Microsc.*, 169:375–382, 1993.

[89] E. M. M. Manders, J. Stap, G. J. Brakenhoff, R. Van Driel, and J. A. Aten. Dynamics of three-dimensional replication patterns during the S-phase analyzed by double labeling of DNA and confocal microscopy. *J. Cell Sci.*, 103(3):857–862, 1992.

[90] S. V. Costes, D. Daelemans, E. H. Cho, Z. Dobbin, G. Pavlakis, and S. Lockett. Automatic and quantitative measurement of protein-protein colocalization in live cells. *Biophys. J.*, 86(6):3993–4003, 2004.

[91] E. barbarese, D. E. Koppel, M. P. Deutscher, C. L. Smith, K. Ainger, F. Morgan, and J. H. Carson. Protein translation components are colocalized in granules in oligodendrocytes. *J. Cell. Sci.*, 108(8):2781–2790, 1995.

[92] B. van Steensel, E. van Binnendijk, C. Hornsby, H. van der Voort, Z. Krozowski, E. de Kloet, and R. van Driel. Partial colocalization of glucocorticoid and mineralocorticoid receptors in discrete compartments in nuclei of rat hippocampus neurons. *J. Cell Sci.*, 109(4):787–792, 1996.

2

Theory

In this chapter, the basic theory of two methods that measure the amount interaction between two fluorescently labeled molecules will be discussed. Both methods predict the fraction of labeled species that interact with a second, distinctly labeled species on the molecular level, from the statistical analysis of two images recorded in separate detection channels. Spatial image cross-correlation spectroscopy (ICCS) is an intensity fluctuation correlation technique that is capable of measuring the absolute numbers of both interacting and non-interacting molecules from two detection channel images. The theory of ICCS will be presented in terms of its development from another fluctuation correlation technique, fluorescence correlation spectroscopy (FCS). The second method that will be discussed, which measures molecular interactions from two images, is called automatic colocalization. Unlike ICCS, in this method, the absolute number of interacting particles is not determined, but the ratio of the interacting particles to that of the total number of particles is evaluated by classifying pixel pairs within the two images as 'colocalized'. These colocalized pixels can then be used to calculate the interaction fraction (IF) within the image, which is interpreted as a strong indication of intermolecular interaction between the two labeled molecules themselves.

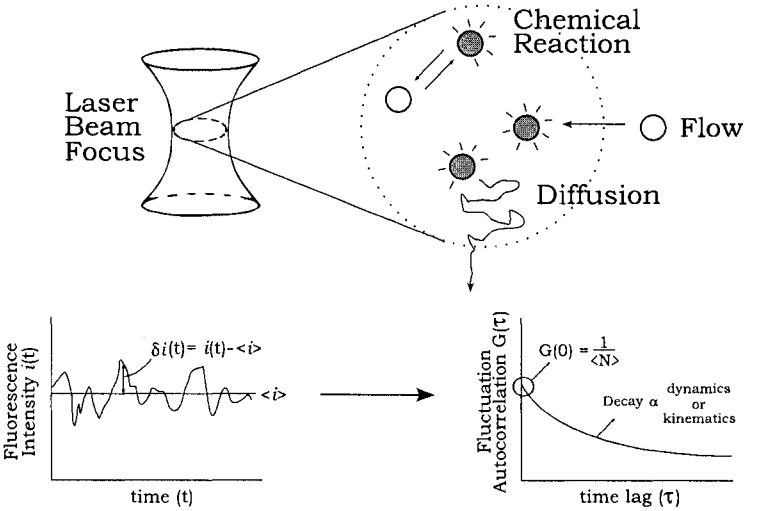

Figure 2.1: Fluctuations in fluorescence intensity arise from changes in the concentration of fluorescent molecules within an excitation volume defined by the focus of a laser beam. Autocorrelation of the intensity fluctuations leads to characterization of the transport properties giving rise to the fluctuations as well as the average particle number density. Adapted from [5].

2.1 *Fluorescence Correlation Spectroscopy (FCS)*

Stochastic fluctuations of a concentration dependent signal about a mean value may resemble random noise, but, as shown in numerous dynamic light scattering experiments carried out in the past [1], these fluctuations contain a wealth of information about the molecular dynamics of the species from which they are measured. In order to facilitate the application of the principles of fluctuation analysis to monitor the motion of molecules in the presence of high concentrations of other species, as well as the investigation of chemical reaction kinetics, Elson, Webb and Magde exploited the sensitivity and specificity of fluorescence in the development of the fluctuation method called fluorescence correlation spectroscopy (FCS) [2–4]. By applying the same theory developed for the analysis of fluctuations in scattered laser light to fluctuations in fluorescence intensity, they showed that the molecular details accessible through fluctuation analysis could be exploited in new and exciting systems, especially in the biological realm.

Spontaneous fluctuations in fluorescence intensity, $\delta i(t)$, arise from changes in the

concentration of fluorescent molecules that are driven by thermal energy, as they enter and exit a small, stationary, excitation volume defined by the focus of a laser beam. The fluctuation is formally defined as the difference between the intensity of a given time point in the time series, $i(t)$, and the mean intensity for the time series, $\langle i \rangle$:

$$\delta i(t) = i(t) - \langle i \rangle . \tag{2.1}$$

In order to extract the dynamic properties of the observed molecules, such as, diffusion coefficients or chemical rate constants, a large number of fluctuations must be recorded and statistically analyzed. In FCS, statistical analysis of the fluctuation record is performed by calculation of a normalized time-averaged autocorrelation function (ACF), $\mathrm{G}(\tau)$, whose functional decay and time-zero amplitude contain information about the dynamic properties and the average number density of the molecules within the laser beam excitation volume, respectively. The ACF is calculated as:

$$G(\tau) = \frac{\langle \delta i(t) \delta i(t+\tau) \rangle}{\langle i \rangle^2}, \tag{2.2}$$

where τ is the time-lag variable and the angular brackets represent the time average over all possible time lags.

Fluorescence correlation spectroscopy relies on theoretical models to predict the functional form of the time correlation function decay, which are required to extract the transport coefficients. The appropriate decay model must be used to fit the observed data and extract the relevant information. For the case of a single population of particles that are freely diffusing in 3-dimensions (3D), and are excited by a laser beam that is assumed to have a Gaussian intensity profile in x, y, and z, the decay of the time autocorrelation function is governed by the following equation (for derivation see [6]):

$$G(\tau) = BM(\tau) = B \frac{1}{\left(1 + \frac{\tau}{\tau_d}\right)} \frac{1}{\sqrt{1 + \left(\frac{\omega_0}{z_0}\right)^2 \frac{\tau}{\tau_d}}}, \tag{2.3}$$

where ω_0 and z_0 are the experimentally determined lateral and axial e^{-2} radii of the laser focal volume, respectively, and $\tau_d = \frac{\omega_0^2}{4D}$ is the characteristic lateral diffusion

time, which is inversely proportional to the diffusion coefficient, D. The zero-time lag amplitude is given by, B, and $M(\tau)$ represents the appropriate decay model for a defined transport/dynamic process.

Regardless of the dynamics occurring within the system (e.g. diffusion, flow, etc.), which will change the shape and rate of decay of the correlation function, the amplitude, B, is inversely proportional to the average number of independent fluorescent entities within the excitation volume, assuming they are ideal (non-interacting). This is shown below by evaluation of the correlation function when $\tau = 0$. First, let us describe the measured fluorescence intensity, i, in terms of the local concentration of fluorescent particles within the excitation volume, C:

$$\langle i \rangle = \eta \langle C \rangle \int W(\mathbf{r}) dV \tag{2.4}$$

$$\delta i(t) = \eta \int \delta C(\mathbf{r}, t) W(\mathbf{r}) dV, \tag{2.5}$$

where the integral is taken over all 3D space. η is the product of the excitation intensity, overall photon detection efficiency, absorption cross-section and the fluorescence quantum yield, and $W(\mathbf{r})$ describes the beam focus excitation volume, which is usually approximated as a 3D Gaussian:

$$W(\mathbf{r}) \approx e^{-2\frac{x^2+y^2}{\omega_0^2}} e^{-2\frac{z^2}{z_0^2}}, \tag{2.6}$$

where the ω_0 and z_0 are the lateral and axial distances, respectively, at which the function decays to $1/e^2$. Substituting Eq. 2.4 and 2.5 into Eq. 2.2, and assuming all fluctuations in the fluorescence intensity can be attributed to fluctuations in particle number, we get:

$$G(\tau) = \frac{\int \int W(\mathbf{r}) W(\mathbf{r}') f(\mathbf{r}, \mathbf{r}', \tau) dV dV'}{\left[\langle C \rangle \int W(\mathbf{r}) dV\right]^2}, \tag{2.7}$$

where

$$f(\mathbf{r}, \mathbf{r}', \tau) = \langle \delta C(\mathbf{r}, t + \tau) \delta C(\mathbf{r}', t) \rangle$$

is the concentration correlation function. When τ is equal to zero, the concentration correlation function for noninteracting particles, $f(\mathbf{r}, \mathbf{r}', 0)$, is nonzero only if $r = r'$,

i.e., particles are correlated at the same time, only at the same position. Therefore,

$$G(0) = \frac{\int\int W(\mathbf{r})W(\mathbf{r}')\,\langle C\rangle\,\delta(\mathbf{r}-\mathbf{r}')dVdV'}{\left[\langle C\rangle \int W(\mathbf{r})dV\right]^2} \tag{2.8}$$

$$= \frac{1}{\langle C\rangle}\frac{\int W^2(\mathbf{r})dV}{\left(\int W(\mathbf{r})dV\right)^2} \tag{2.9}$$

$$= \frac{1}{\langle C\rangle\, V_{eff}} = \frac{1}{\langle N\rangle}, \tag{2.10}$$

where we have defined the integral ratio of the beam excitation volume as the effective focal volume, V_{eff}, and $\langle N\rangle$ is the average number of particles per laser excitation beam volume.

Evaluation of the amplitude of the autocorrelation function is therefore a direct measure of the average number of particles within the focal volume. The amplitude, $G(0) = \frac{\langle(\delta i)^2\rangle}{\langle i\rangle^2}$, however, cannot be calculated directly from the intensity fluctuation data due to various white noise sources, and is usually obtained by fitting to the appropriate model without weighting the zero-lag value and extrapolating the fit to $\tau = 0$.

Due to the stochastic nature of the fluorescence intensity fluctuations, it is imperative that a sufficient number of spontaneous fluctuations be recorded, if accurate transport coefficients are to be measured. Experimentally, this criterion was met by minimization of the excitation volume (< 1 fL) to ensure a reasonably small residence time (< 1 s) within the volume for each molecular species, which defines a single fluctuation. By minimizing the time in which a single fluctuation occurs, hundreds or thousands can be sampled in a matter of seconds ensuring reasonable statistics to extract phenomenological data from the correlation of the intensity fluctuations. The small excitation volume also leads to very low numbers of particles within the focus at any particular time (~1-2 particles), which ensures the size of the fluctuations are large enough to be measured. Low concentrations are essential for FCS since the relative fluctuations, $\frac{\delta N}{N}$, are proportional to $\frac{1}{\sqrt{N}}$. The reduction in the focal volume was made possible by the use of confocal pinholes to restrict the size of

the illuminated volume [7] in combination with extremely sensitive photon detectors (e.g. avalanche photodiodes) to capture the brief bursts of fluorescence that occur as molecules rapidly diffuse in solution ($\sim 9 \times 10^{-7} \frac{cm^2}{s}$ for GFP in water [8]) through the excitation volume.

Due to several technological advances in fluorescence detection and data acquisition, FCS is sensitive to dynamic processes occurring on the μs to ms timescale, and since its inception in the early 1970's, has led to the measurement of intersystem crossing rates [9], translational [10–12] and rotational [13, 14] diffusion coefficients, flow rates [15], molecular weights [16], particle aggregation [17], as well as several other applications, including detection and quantification of interactions through extension of FCS to cross-correlation analysis (see [18] for a detailed review).

2.1.1 *Fluorescence Cross-Correlation Spectroscopy (FCCS)*

Molecular interactions between different macromolecules are the basis for almost all biochemical reactions. To measure these interactions using the principles of fluorescence fluctuation spectroscopy it is advantageous to introduce a second, spectrally distinct fluorescent label in order to record intensity fluctuations from two separate detection channels simultaneously. Three different time-averaged correlation functions can be calculated from this type of data including the two autocorrelation functions for each detection channel, in addition to a cross-correlation function (CCF) between the two signals.

The value of the cross correlation function will be non zero, only if the fluctuations recorded in the two detection channels are correlated in time. In such a case, the CCF contains information regarding the number densities and dynamics of those particles which are moving in unison, i.e. those that are interacting. Analogous to Eq. 2.5, one can define equations for the fluorescence intensity fluctuations for the two separate detection channels, but they will include contributions from both interacting and

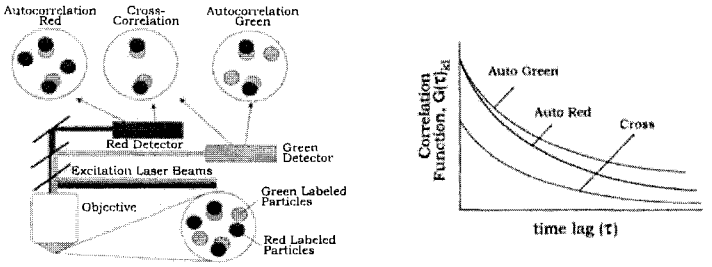

Figure 2.2: Schematic diagram of an FCCS experiment. Fluorescently labeled particles (green and red) move in and out of the excitation laser beam focus. The green detection channel contains fluorescence intensity contributions from all of the green labeled particles, as well as the interacting green/red particles that are moving together. Similarly, the red detection channel contains fluorescence intensity contributions from all of the red particles and the interacting particles. Temporal cross-correlation of the two detection channels will only contain contributions from those particles which are interacting. The ratio of the zero-lag amplitude of the cross-correlation function to that of the autocorrelation functions, provides a measure of the fraction of interacting molecules, while the decay of each of the correlation functions provides information on the dynamics of each of the three distinct molecular species (green, red and interacting, green-red particles). Adapted from [19].

non-interacting particles:

$$\delta i_1(t) = \eta_1 \int \delta \left(C_1(\mathbf{r},t) + C_{12}(\mathbf{r},t) \right) W_1(\mathbf{r}) dV \tag{2.11}$$

$$\delta i_2(t) = \eta_2 \int \delta \left(C_2(\mathbf{r},t) + C_{12}(\mathbf{r},t) \right) W_2(\mathbf{r}) dV, \tag{2.12}$$

where N_{12} is the number density of interacting particles and N_k is the number density of non-interacting particles detected in channel, $k = 1$ or 2, and W_k defines the beam focus excitation volume for channel k. By assuming that there is sufficient separation between the emission spectra of the two fluorescent labels such that negligible spectral bleed-through of signal between channels exists, and that the effective detection volumes of the two channels are equivalent, then the autocorrelation function for channel k may be written as,

$$G_k(\tau) = \frac{\langle C \rangle_k M_k(\tau) + \langle C \rangle_{12} M_{12}(\tau)}{V_{eff} \left(\langle C \rangle_k + \langle C \rangle_{12} \right)^2}, \quad k = 1, 2 \tag{2.13}$$

and the cross-correlation function as,

$$G_{12}(\tau) = \frac{\langle C_{12} \rangle M_{12}(\tau)}{V_{eff} \left(\langle C_1 \rangle + \langle C_{12} \rangle \right) \left(\langle C_2 \rangle + \langle C_{12} \rangle \right)}, \tag{2.14}$$

where $M(\tau)$ is the model that describes the decay dynamics for either the singly labeled species, M_k, or the interacting species, M_{12}, (see Eq. 2.3). Therefore, fitting the two auto- and cross-correlation curves with the appropriate functional model will yield the number densities (at $\tau = 0$) and dynamic properties of both interacting and non-interacting species, which makes FCCS a potentially powerful tool for real-time monitoring of small concentrations of interacting particles *in vitro* and in cells.

The first experimental realization of FCCS was performed by Schwille et al. in 1997, who used two separate laser lines to excite two distinct fluorophores attached to DNA strands and successfully followed the renaturation of DNA using this method [19]. Fluorescence cross-correlation spectroscopy has since been used for kinetic binding studies [20, 21], detection of molecular interactions in the presence of large concentrations of non-interacting species [22], and has even been extended to the analysis of triple-color labeled systems to monitor higher order complex formation [23].

2.2 Image Correlation Spectroscopy (ICS)

Image correlation spectroscopy (ICS) is an extension of FCS in that fluorescence intensity excited in a diffraction-limited laser beam focal volume is recorded, followed by correlation of the intensity fluctuations, although unlike FCS, the laser focus is rapidly scanned across the sample and the intensity is recorded in a two-dimensional (2D) image pixel array, and the scanning can be repeated in time to generate an image time series [24]. In principle, ICS can be applied to molecules that are free to move in three dimensions, but is typically performed on systems that are restricted to 2D, such as proteins that are embedded in the planar cell membrane. The image collection is typically achieved by employing a confocal laser scanning microscope, but practically any fluorescence imaging system would suffice. With ICS therefore, two distinct types of fluctuations are recorded; spatial fluctuations as a function of pixel position within a given image (i.e. a single time sample), and fluctuations in time defined for each pixel position through the entire image time series (Fig. 2.3).

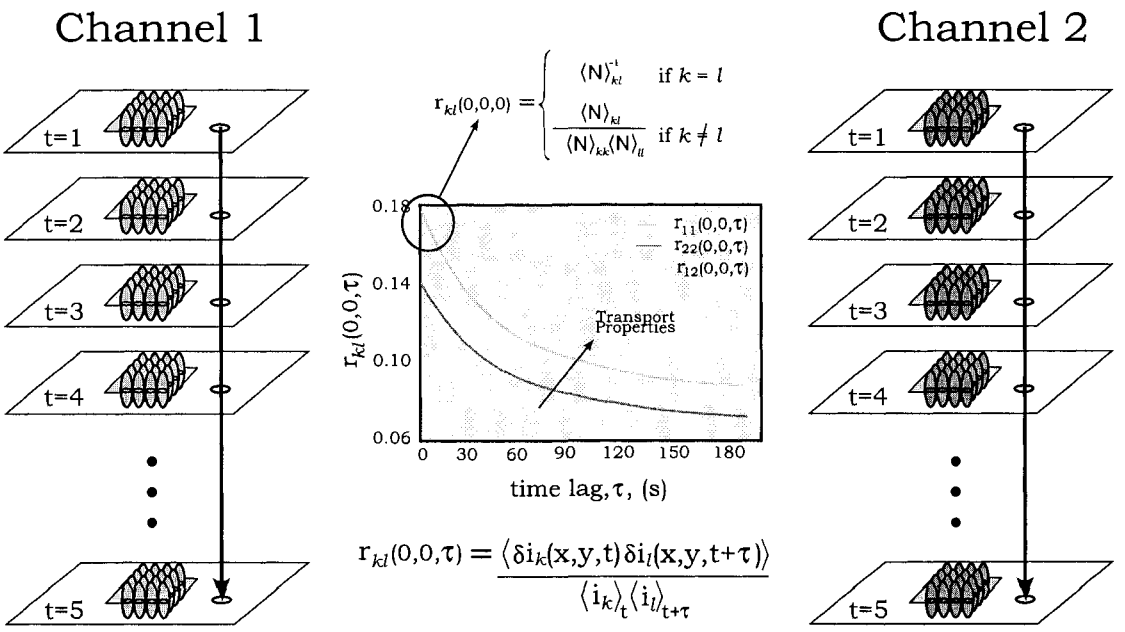

Figure 2.3: Image series are recorded in two separate detection channels, k and l, at different emission wavelength windows. The images are subsequently correlated in time and averaged over all pixel positions, (x, y). The images sampled in channel 1 or 2 can be correlated with themselves (autocorrelation), or with each other (cross-correlation). The decay of the resulting time correlation functions can then be used to extract the transport properties of the system and the amplitudes used to determine the number of particles per beam area (BA) in channel 1, $\langle N \rangle_1$, channel 2, $\langle N \rangle_2$ and the number of interacting particles per BA, $\langle N \rangle_{12}$.

The spatio-temporal fluctuation is defined as the difference between the fluorescence intensity recorded at pixel position, (x, y), and time, t, and the mean intensity of the image sampled at that time:

$$\delta i(x, y, t) = i(x, y, t) - \langle i \rangle_t \,, \tag{2.15}$$

where $\langle i \rangle_t$ is the average intensity over the image. It should be noted that in this definition all the pixels in a given image are assumed to be recorded simultaneously, even though a typical 256×256 pixel image may take $\sim$0.5 s to be acquired on a laser scanning microscope. This assumption is not problematic as long as the dynamics of the system are slower than the image acquisition rate while correlations for those species that move faster than the imaging rate will be lost.

By incorporating spatial fluctuations in addition to those recorded in time, ICS

can access processes that occur at much slower time scales than that of FCS, without having to extend sampling time periods excessively. This is because the ICS measurement is effectively performed in a quasi parallel fashion over a region of the sample ($> 10\ \mu m^2$) as opposed to the single point collection set-up employed in FCS. Image correlation also allows for visual inspection of the system of interest via the image, which is advantageous for cellular applications.

Analogous to FCS (and dynamic light scattering), the correlation of fluctuations in fluorescence intensity to generate an ACF that is fit with the appropriate model, will allow determination of the average number density and quantification of transport properties. For ICS, this involves the calculation of a normalized 2D intensity fluctuation spatio-temporal correlation function from the intensity fluctuations for the image time series. The general form of this 2D spatio-temporal correlation function from which all of the related ICS techniques are derived is written as,

$$r\left(\xi,\eta,\tau\right)_{kl} = \frac{\left\langle\left\langle \delta i_k\left(x,y,t\right)\delta i_l\left(x+\xi,y+\eta,t+\tau\right)\right\rangle\right\rangle}{\left\langle i_k\left(x,y,t\right)\right\rangle_t\left\langle i_l\left(x,y,t+\tau\right)\right\rangle_{t+\tau}}, \tag{2.16}$$

where ξ and η are spatial lag (or shift) variables, τ is the temporal lag variable, and the angular brackets in the denominator represent the average intensity of the images sampled at time, t and $t+\tau$. The inner angular brackets in the numerator represent a spatial average over all equivalent spatial lag values, and the outer angular brackets are included for cases in which temporal averaging is performed over equivalent time lags. Subscripts, k and l, are included to allow for the possibility of correlating fluorescence fluctuations recorded in two separate detection channels. The function, $r(\xi,\eta,\tau)_{kl}$, is an autocorrelation function when $k = l$ and a cross-correlation function when $k \neq l$.

Several methods exist to analyze the correlation of spatio-temporal fluctuations in order to extract different types of information. The decay of the zero spatial-lags temporal autocorrelation function, $r(0,0,\tau)_{kl}$, can be followed as a function of τ to provide analogous information on transport dynamics as those measured using FCS (see Fig. 2.1). This temporal ACF would also be fit with the appropriate decay func-

tion to measure dynamic processes that occur on the s to min timescale, such as the relatively slow transport of membrane proteins. This approach is referred to as temporal ICS (TICS) [25]. Similar dynamic information may be obtained by Fourier transforming each image in the time series prior to correlation and fitting the decay of $r(k_x, k_y, \tau)_{kl}$ to the appropriate model. The advantage of performing the time correlation on the Fourier transformed image time series is that any fluorescence intensity fluctuations that arise from the motion of the labeled molecules are separated from the intensity fluctuations due to photobleaching or intermittent blinking of the fluorescence probe. This approach is referred to as k-space image correlation spectroscopy (kICS) [26]. By correlating in space and time to generate a full space-time correlation function, $r(\xi, \eta, \tau)_{kl}$, and then tracking the center, (υ, ν), as a function of time lag, τ, high resolution vector maps of the velocities of fluorescently labeled molecules can be produced. This approach is referred to as space time image correlation spectroscopy (STICS) [27, 28]. In order to measure particle dynamics on faster time scales (μs to s) than those described above, the inherently fast time structure contained within a CLSM acquired image is exploited. Although it may take 0.5 s or longer to acquire a full 256×256 pixel image, each pixel is acquired on the order of μs, and each line of pixels on the order of ms. Therefore, spatial correlations, $r(\xi, \eta, 0)_{kl}$, along the fast raster scan direction of the image, which account both for the movement of molecules and the time of the raster scan, can be used to extract the fast dynamics of molecules in solution or in cells. This approach is referred to as raster image correlation spectroscopy (RICS) [29, 30].

Finally, the spatial correlation function, $r(\xi, \eta, 0)_{kl}$, can be calculated for a given time sample (image) whose amplitude is inversely proportional to the average number of independent particles within the excitation laser beam area (BA) [31]. This technique is referred to spatial ICS and will be the focus of subsequent chapters. The spatial correlation function is expected to have the form of a 2D Gaussian function due to the profile of the excitation laser beam used to excite the fluorescently la-

beled particles. In practice, the spatial correlation function for a given time sample is efficiently calculated by use of a fast Fourier transform algorithm,

$$r\left(\xi,\eta,0\right)_{kl}=\frac{F^{-1}\left\{F\left(\mathbf{I_k}(x,y,t)\right)F^{*}\left(\mathbf{I_l}(x,y,t)\right)\right\}}{\left\langle\mathbf{I_k}(x,y,t)\right\rangle_t\left\langle\mathbf{I_l}(x,y,t)\right\rangle_t}-1, \tag{2.17}$$

where F and F^{-1} represent the Fourier and inverse Fourier transform respectively, F^{*} is its complex conjugate and $\mathbf{I_k}(x,y,t)$ and $\mathbf{I_l}(x,y,t)$ are the 2D pixel image arrays recorded in detection channel, k and l, respectively, at time t.

Assuming that the particles are uniformly randomly distributed over the entire area of interest, are smaller than the point spread function (PSF) of the microscope, and that the excitation laser BA at the focus can be approximated by a 2D Gaussian function, then the spatial correlation function, $r(\xi,\eta,0)_{kl}$, will decay as a 2D Gaussian function. A 5-parameter, nonlinear least squares fit of the spatial ACF to the following Gaussian function is therefore used to extract all possible information contained therein.

$$r\left(\xi,\eta,0\right)_{kl}=\mathbf{r}\left(\mathbf{0,0,0}\right)_{\mathbf{kl}}\exp\left[-\frac{\left(\xi+\upsilon\right)^2+\left(\eta+\nu\right)^2}{{\omega_o}^2}\right]+\boldsymbol{r_\infty}. \tag{2.18}$$

where the fit parameters are in shown in bold and are the zero-lags amplitude, $r(0,0,0)_{kl}$, the e^{-2} laser beam radius, ω_0, the position of the maximum, (υ,ν), and an offset parameter, r_∞, to account for long-range spatial correlations. Spatial ICS can be used to measure particle number densities in single images of fixed cells [32], and by employing the spatial cross-correlation of two detection channel images, can be used to measure molecular interactions in fixed or living cells. Since spatial ICS will be the focus of subsequent chapters the techniques will be explained in more detail in the following section.

2.2.1 *Image Cross-Correlation Spectroscopy (ICCS)*

For single photon, confocal laser scanning microscopy ICCS, two separate laser lines are usually used to excite two spectrally distinct fluorophores and the fluorescence emission is separated and collected in two detection channels. As in the previously

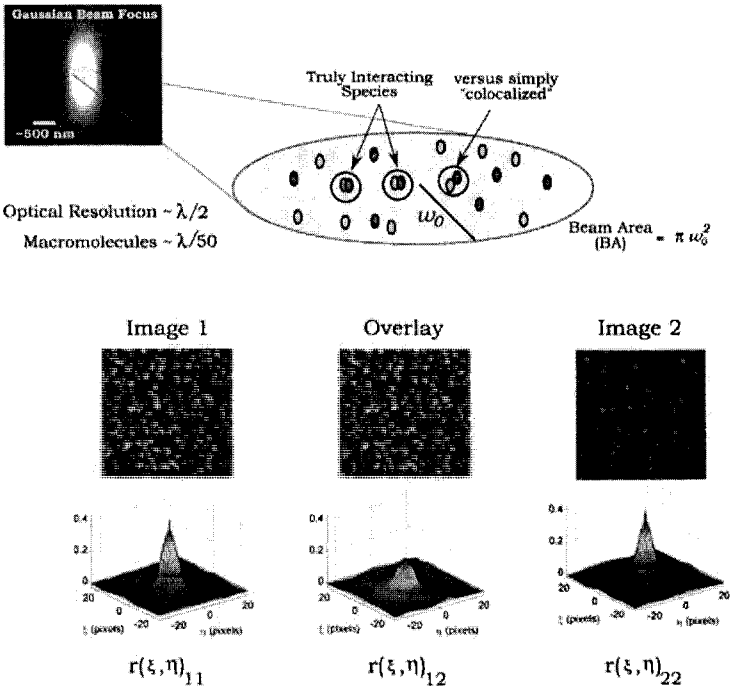

Figure 2.4: In order to determine the amount of particle colocalization present between two images, image cross-correlation spectroscopy (ICCS) relies on direct measurement of the ratio of the number of interacting particles to that of the total number of particles in a given detection channel, by evaluation of the amplitude of the spatial cross-correlation and autocorrelation functions respectively. Due to the statistical nature of the measurement, ICCS is well-equipped to distinguish the amount of interacting (colocalized) particles from those which are simply found by chance in close proximity. Note the sharp peak at the zero spatial-lags position of the autocorrelation functions, which is due to the presence of white noise in the respective images.

discussed fluctuation techniques, the inverse of the number of particles per beam area (BA) for channel k, including both interacting and noninteracting species, is equal to the square relative fluctuation,

$$\langle N \rangle_k^{-1} = \frac{\langle (\delta i_k)^2 \rangle}{\langle i_k \rangle^2}. \tag{2.19}$$

In practice, white noise sources contributing to every pixel intensity within the image prevent a direct calculation of the square relative fluctuation, thus necessitating its indirect evaluation via extrapolation of the best fit function (Eq. 2.18) to the zero-lags amplitude of the normalized spatial intensity fluctuation correlation function (Eq. 2.16). By definition, the spatio-temporal correlation function described by Eq. 2.16 is a spatial correlation function when $\tau = 0$ and, therefore, the time-lag value of zero will be omitted in subsequent references to spatial auto- or cross-correlation functions, i.e $r(\xi, \eta, 0)_{kl} \equiv r(\xi, \eta)_{kl}$.

If there is complete spatial overlap of the foci of the two laser beams and no quenching or fluorescence enhancement upon interaction of the two fluorescent species, the zero-lags amplitude of the spatial cross-correlation function is directly proportional to $\langle N \rangle_{kl}$, the average number of interacting particles per beam area [33]:

$$\langle N \rangle_{kl} = \frac{r(0,0)_{kl}}{r(0,0)_{kk} r(0,0)_{ll}} \frac{A_l}{A_k} \tag{2.20}$$

where the number of interacting particles may be determined directly from the fitted amplitudes of the cross-correlation function, and the two autocorrelation functions, as well as the ratio of the effective areas defined by the focal spots of the two lasers ($A_l > A_k = \pi\omega_k^2$). The effective area ratio, which is included in Eq. 2.20 when the two excitation and detection volumes differ by a small amount [34], can be measured directly from the fitted beam radii for each detection channel.

For each pair of images collected, a spatial autocorrelation function can be calculated for each detection channel, along with a cross-correlation function. Each correlation function is fit to a 2D Gaussian (Eq. 2.18) to obtain best fit $r(0,0)_{11}$, $r(0,0)_{22}$, and $r(0,0)_{12}$ values. Particle colocalization coefficients, $M1_{ICCS}$ and $M2_{ICCS}$, which

are defined as the ratio of the number of interacting particles to the total number of particles per beam area for a particular detection channel, are determined using the following equations [35]:

$$M1_{ICCS} = \frac{r(0,0)_{kl}}{r(0,0)_{ll}} = \frac{\langle N \rangle_{kl}}{\langle N \rangle_{kk}} \qquad M2_{ICCS} = \frac{r(0,0)_{kl}}{r(0,0)_{kk}} = \frac{\langle N \rangle_{kl}}{\langle N \rangle_{ll}} \tag{2.21}$$

The colocalization coefficients are the parameters which are measured to characterize the interaction between the two fluorescently tagged species. Due to the importance of molecular interactions in regulating biochemical reaction pathways, and the readily available fluorescent probes, many approaches have been developed to measure such interactions from two fluorescence images recorded in separate detection channels. One group of image analysis techniques relies on the statistical calculation of interaction fractions (IFs) based on correlation coefficients determined for overlapping pixels in the two detection channel images. These techniques are referred to as automatic colocalization, and will be described in detail in the following section.

2.3 *Automatic Colocalization*

Few would have anticipated the widespread application of the statistical colocalization coefficients, $M1$ and $M2$, since being introduced by Manders et al. almost 15 years ago. The need for a relatively simple, robust approach to measuring colocalized signals in dual labeling fluorescence imaging experiments, however, led to commercial availability of the technique and numerous applications in different biological systems [36, 37].

For automatic colocalization, pixels in the two detection channels are classified as either colocalized or not based on comparison to a predetermined intensity threshold, and the colocalization coefficients are then calculated from the ratio of the sum of the

intensities of colocalized pixels to the total intensity in each channel.

$$M1 = \frac{\sum\limits_{(x,y)} i_{1,coloc}}{\sum\limits_{(x,y)} i_1} \qquad M2 = \frac{\sum\limits_{(x,y)} i_{2,coloc}}{\sum\limits_{(x,y)} i_2}, \tag{2.22}$$

where $i_{1,coloc} = i_1(x,y)$ if $i_2(x,y) > i_{\text{threshold}}$ and $i_{1,coloc} = 0$ if $i_2(x,y) \leq i_{\text{threshold}}$. $i_{2,coloc} = i_2(x,y)$ if $i_1(x,y) > i_{\text{threshold}}$ and $i_{2,coloc} = 0$ if $i_1(x,y) \leq i_{\text{threshold}}$. The sum is taken over all pixels in the image. Originally, the colocalization threshold value was chosen to be zero. Due to the size of the PSF, however, this choice leads to significant contributions from random overlap of adjacent pixels and therefore results in overestimation of the colocalization coefficients at relatively moderate particle densities. Manual determination of the threshold value, such as estimation of the background noise level, aids the situation somewhat, but still includes randomly overlapping pixels of higher intensities as the particle density increases.

Recently, Costes et al. developed an automatic method to determine the colocalization threshold used to calculate $M1$ and $M2$ based on Pearson's correlation coefficient, r_P [38]. Note that r_P is a statistical correlation coefficient and not a correlation function as discussed earlier. Pearson's correlation coefficient is an accurate measure of colocalization when the densities of the two species of interest are approximately equal [39, 40]. Pearson's correlation coefficient ranges from -1, for perfect anticorrelation, to +1 for perfect correlation between the two variables. For the two channel image data sets, it is calculated as,

$$r_P = \frac{\sum\limits_{(x,y)} (i_1(x,y) - \langle i_1 \rangle)(i_2(x,y) - \langle i_2 \rangle)}{\sqrt{\sum\limits_{(x,y)} (i_1(x,y) - \langle i_1 \rangle)^2 \sum\limits_{(x,y)} (i_2(x,y) - \langle i_2 \rangle)^2}}, \tag{2.23}$$

where $i_1(x,y)$ and $i_2(x,y)$ are the intensities in detection channel 1 and 2, respectively; the angular brackets indicate an image average of the intensity; and the sum is over all pixels.

Costes' automatic threshold method relies on determination of the threshold intensity value, $T_{critical}$, below which pixels yield an r_P value of zero, i.e, no correlation

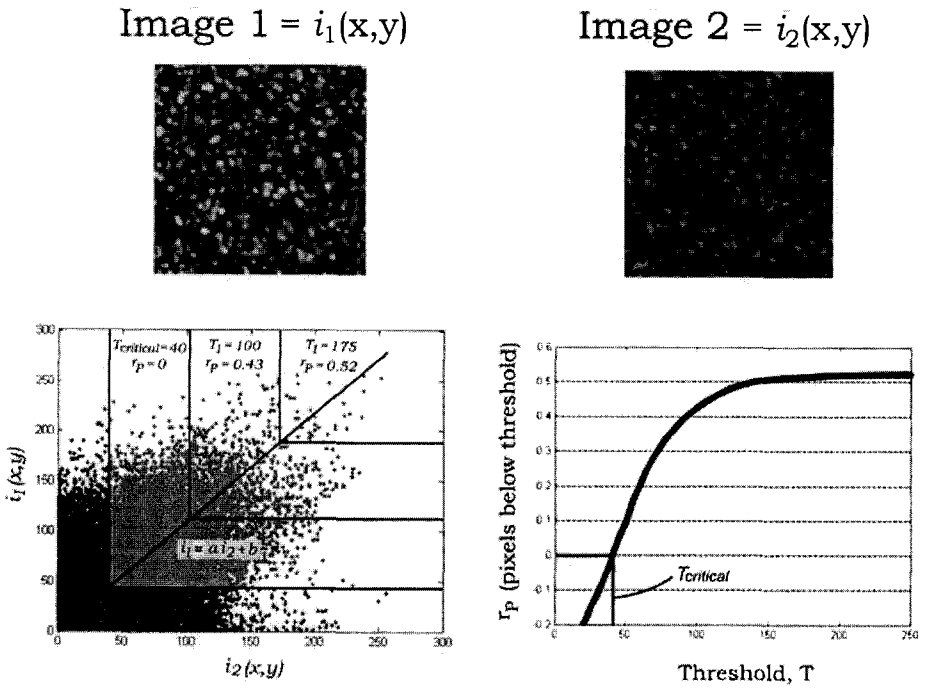

Figure 2.5: Automatic colocalization proceeds by successively lowering pixel intensity thresholds, T_1 and $T_2 = aT_1 + b$, and determining Pearson's correlation coefficient, r_P, for all pixel positions below both threshold values. The slope, a, and intercept b, which define the brightness relationship between image 1 and image 2, are determined from orthogonal linear regression of the two channel pixel intensities. Pearson's correlation coefficient decreases as the thresholds are lowered, eventually reaching zero when no correlation between pixels of image 1 and image 2 exists. The pixel intensity value, $T_{critical}$, which leads to the r_P value of zero is subsequently used for calculation of the colocalization coefficients for the two images as defined by Eq. 2.24.

remains. The idea stems from the fact that, in general, colocalized, or positively correlated pixels are of higher intensity than non-correlated pixels and the intensity threshold value that separates these two populations can be found by successive evaluation of a correlation coefficient between the two images (Fig. 2.5). The automatically determined threshold can then be used to evaluate Manders' colocalization coefficients as follows:

$$M1_{Auto} = \frac{\sum_{i_1(x,y)>T_1 \ \& \ i_2(x,y)>T_2} i_1(x,y)}{\sum_{\text{All } i_1(x,y)} i_1(x,y)} \qquad M2_{Auto} = \frac{\sum_{i_1(x,y)>T_1 \ \& \ i_2(x,y)>T_2} i_2(x,y)}{\sum_{\text{All } i_2(x,y)} i_2(x,y)} \tag{2.24}$$

Both $i_1(x,y) > T_1$ and $i_2(x,y) > T_2$ must be true for pixel intensities $i_1(x,y)$ and $i_2(x,y)$ to contribute to the sum in the numerator of their respective colocalization coefficient. Pixels below the channel threshold value contribute zero to the sum in the numerator. The colocalization threshold values, T_1 and T_2, are found by first performing orthogonal linear regression on the two-dimensional histogram of pixel intensities (i.e., a plot of $i_1(x,y)$ versus $i_2(x,y)$, see Fig. 2.5) to account for differences in intensity between the two channels. Once the slope, a, and intercept, b, of this line are determined, an initial threshold, $T_{initial}$, is chosen and the locations of all pixels below $T_1 = T_{initial}$ and the $T_2 = aT_1 + b$ are found. If the r_P value calculated for the pixels below T_1 and T_2 is positive, then the colocalization threshold, $T_{initial}$, is lowered and the process is repeated incrementally until the chosen threshold, $T = T_{critical}$, leads to $r_P = 0$ for those pixels below T_1 and T_2. The colocalization thresholds are then used in calculation of $M1_{Auto}$ and $M2_{Auto}$ via Eq. 2.24.

2.3.1 *Colocalization Significance Test*

Automatic colocalization relies on intensity threshold determination via calculation of Pearson's correlation coefficient. Calculation of r_P, however, for two uncorrelated images will still lead to non-zero values, which places a fundamental limit on the minimum interaction fraction that can be detected using this type of statistical analysis. Therefore, a colocalization significance test was outlined by Costes et al. [38] based

on previous statistical tests [41], which was intended to assess whether or not a pair of images contained 'true' colocalization. This test was designed to be performed prior to automatic colocalization analysis in order to decide whether to proceed with the automatic determination of the colocalization coefficients, $M1_{Auto}$ and $M2_{Auto}$. This test will be discussed in the context of colocalization analyses in subsequent chapters and will therefore be discussed here. Briefly, subregions of one image, approximately the size of the Gaussian convolution function (simulating the PSF or beam focus), are randomly permuted in space and then used together with the second, non-permuted image, to calculate r_P. A large number ($\sim$2000) of r_P values are calculated that correspond to different random permutations of one of the images. If r_P calculated between the two unaltered images is greater than the correlation between 97% of the permuted images, then the images are said to have significant colocalization see Fig. 2.6.

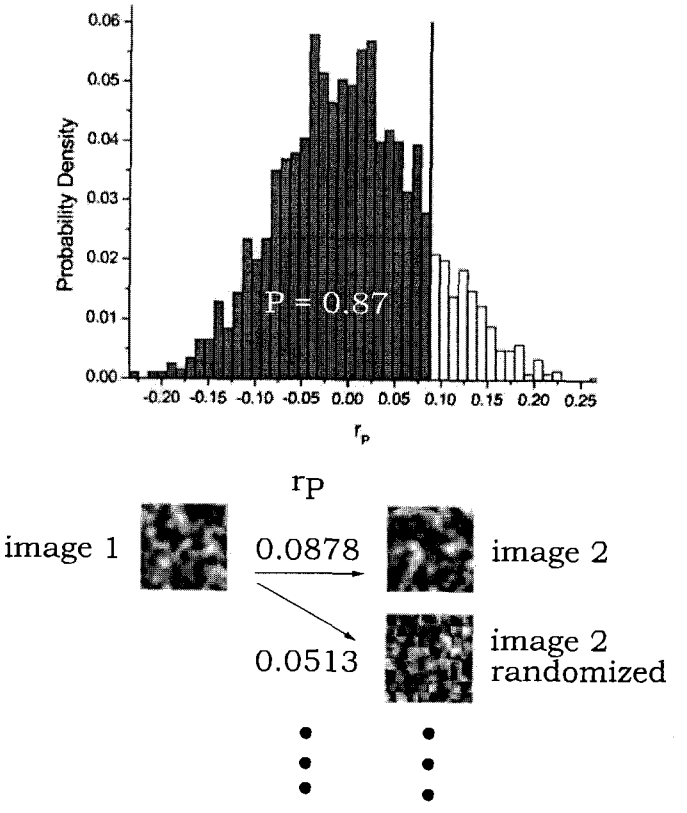

Figure 2.6: The colocalization significance test is applied to two images that are suspected to contain colocalized pixels intensities due to the presence of molecular interaction. The test is designed to be performed prior to automatic colocalization analysis in order to identify whether or not 'true' colocalization exists between the two images. Pearson's correlation coefficient is calculated between the first image, and a large number of randomized versions of the second image. In this case, two images were simulated with 2% interaction, and 2000 permutations of the second image were performed. The distribution of the r_P values calculated for the 2000 image pairs is shown in the histogram. The shaded area represents the probability, P, that r_P calculated with the randomized images will be less than r_P calculated between the two original images. A line is plotted at $r_P = 0.0878$, which is the value calculated for the two original images. If $P > 0.97$, then the images are said to contain significant colocalization and automatic colocalization analysis can be performed to quantify the IF. In this case $P = 0.87$, and therefore, automatic colocalization analysis is not applicable to this image pair. Adapted from [38].

Bibliography

[1] B. J. Berne and R. Pecora. *Dynamic Light Scattering: With Applications to Chemistry, Biology, and Physics.* Dover, 2000.

[2] D. Magde, E. Elson, and W. W. Webb. Thermodynamic fluctuations in a reacting system – measurement by fluorescence correlation spectroscopy. *Phys. Rev. Lett.* , 29(11):705–708, 1972.

[3] E. L. Elson and D. Magde. Fluorescence correlation spectroscopy. I. Conceptual basis and theory. *Biopolymers*, 13:1–27, 1974.

[4] D. Magde, E. L. Elson, and W. W. Webb. Fluorescence correlation spectroscopy. II. An experimental realization. *Biopolymers*, 13(1):29–61, Jan 1974.

[5] N. L. Thompson. Fluorescence correlation spectroscopy. In Joseph R. Lakowicz, editor, *Topics in Fluorescence Correlation Spectroscopy, Volume 1: Techniques*, pages 337–378. Plenum Press, 1991.

[6] O. Krichevsky and G. Bonnet. Fluorescence correlation spectroscopy: The technique and its applications. *Rep. Prog. Phys.*, 65(2):251–297, 2002.

[7] R. Rigler, Ü. Mets, J. Widengren, and P. Kask. Fluorescence correlation spectroscopy with high count rate and low background: Analysis of translational diffusion. *Eur. Biophys. J.*, 22(3):169–175, 1993.

[8] C. W. Mullineaux, A. Nenninger, N. Ray, and C. Robinson. Diffusion of green fluorescent protein in three cell environments in *Escherichia Coli. Journal of Bacteriology*, 188(10):34423448, 2006.

[9] J. Widengren, Ü. Mets, and R. Rigler. Fluorescence correlation spectroscopy of triplet states in solution: A theoretical and experimental study. *J. Phys. Chem.*, 99(36):13368–13379, 1995.

[10] P. F. Fahey, D. E. Koppel, L. S. Barak, D. E. Wolf, E. L. Elson, and W. W. Webb. Lateral diffusion in planar lipid bilayers. *Science*, 195(4275):305–306, 1977.

[11] P. F. Fahey and W. W. Webb. Lateral diffusion in phospholipid bilayer membranes and multilamellar liquid crystals. *Biochemistry*, 17(15):3046–3053, 1978.

[12] J. Korlach, P. Schwille, W. W. Webb, and G. W. Feigenson. Characterization of lipid bilayer phases by confocal microscopy and fluorescence correlation spectroscopy. *Proc. Natl. Acad. Sci. USA*, 96(15):8461–8466, Jul 1999.

[13] M. Ehrenberg and R. Rigler. Rotational brownian motion and fluorescence intensity fluctuations. *Chem. Phys.*, 4(3):390–401, 1974.

[14] P. Kask, P. Piksarv, Ü. Mets, M. Pooga, and E. Lippmaa. Fluorescence correlation spectroscopy in the nanosecond time range: Rotational diffusion of bovine carbonic anhydrase B. *European Biophysics Journal*, 14(4):257–261, 1987.

[15] D. Magde, W.W. Webb, and E.L. Elson. Fluorescence correlation spectroscopy. III. Uniform translation and laminar flow. *Biopolymers*, 17:361–376, 1978.

[16] M. Weissman, H. Schindler, and G. Feher. Determination of molecular weights by fluctuation spectroscopy: Application to DNA. *Proc. Natl. Acad. Sci.*, 73(8):2776–2780, 1976.

[17] M. Pitschke, R. Prior, M. Haupt, and D. Riesner. Detection of single amyloid β-protein aggregates in the cerebrospinal fluid of Alzheimer's patients by fluorescence correlation spectroscopy. *Nature Medicine*, 4(7):832–834, 1998.

[18] R. Rigler and E. S. Elson, editors. *Fluorescence correlation spectroscopy: Theory and applications.* Springer, 2001.

[19] P. Schwille, F.-J. Myer-Almes, and R. Rigler. Dual color fluorescence cross-correlation spectroscopy for multicomponent diffusional analysis in solution. *Biophys. J.*, 72(4):1878–1886, 1997.

[20] U. Kettling, A. Koltermann, P. Schwille, and M. Eigen. Real-time enzyme kinetics monitored by dual-color fluorescence cross-correlation spectroscopy. *Biochemistry*, 95(4):1416–1420, 1998.

[21] J. L. Swift, M. C. Burger, D. Massotte, T. E. S. Dahms, and D. T. Cramb. Two-photon excitation fluorescence cross-correlation assay for ligand-receptor binding: Cell membrane nanopatches containing the human μ-opioid receptor. *Anal. Chem.*, 79(17):6783–6791, 2007.

[22] P. S. Pyenta, D. Holowka, and B. Baird. Cross-correlation analysis of inner-leaflet-anchored green fluorescent protein co-redistributed with IgE receptors and outer leaflet lipid raft components. *Biophys. J.*, 80(5):2120–2132, 2001.

[23] K. G. Heinze, M. Jahnz, and P. Schwille. Triple-color coincidence analysis: One step further in following higher order molecular complex formation. *Biophys. J.*, 86(1):506–516, 2004.

[24] N. O. Petersen, P. L. Hoddelius, P. W. Wiseman, O. Seger, and K. E. Magnusson. Quantitation of membrane receptor distributions by image correlation spectroscopy: Concept and application. *Biophys. J.*, 65(3):1135–46, Sep 1993.

[25] P.W. Wiseman, J.A. Squier, M.H. Ellisman, and K.R. Wilson. Two-photon image correlation spectroscopy and image cross-correlation spectroscopy. *J. Microsc.*, 200(Pt 1):14–25, Oct 2000.

[26] D. L. Kolin, D. Ronis, and P. W. Wiseman. k-space image correlation spectroscopy: A method for accurate transport measurements independent of fluorophore photophysics. *Biophys. J.*, 91(8):3061–3075, 2006.

[27] B. Hebert, S. Costantino, and P. W. Wiseman. Spatio-temporal image correlation spectroscopy (STICS) theory, verification, and application to protein velocity mapping in living CHO cells. *Biophys. J.*, 88:3601–3614, May 2005.

[28] P. W. Wiseman, C. M. Brown, D. J. Webb, B. Hebert, N. L. Johnson, J. A. Squier, M. H. Ellisman, and A. F. Horwitz. Spatial mapping of integrin interactions and dynamics during cell migration by image correlation microscopy. *J. Cell Sci.*, 117(23):5521–5534, 11 2004.

[29] M.A. Digman, P. Sengupta, P.W. Wiseman, C.M. Brown, A.R. Horwitz, and E. Gratton. Fluctuation correlation spectroscopy with a laser-scanning microscope: Exploiting the hidden time structure. *Biophys. J.*, 88:L33–L36, 2005.

[30] M.A. Digman, C.M. Brown, P. Sengupta, P.W. Wiseman, A.R. Horwitz, and E. Gratton. Measuring fast dynamics in solutions and cells with a laser scanning microscope. *Biophys. J.*, 89:1317–1327, 2005.

[31] P. W. Wiseman and N. O. Petersen. Image correlation spectroscopy. II. Optimization for ultrasensitive detection of preexisting platelet-derived growth factor-beta receptor oligomers on intact cells. *Biophys. J.*, 76(2):963–77, Feb 1999.

[32] S. Costantino, J. W.D. Comeau, D. L. Kolin, and P. W. Wiseman. Accuracy and dynamic range of spatial image correlation and cross-correlation spectroscopy. *Biophys. J.*, 89:1251–1260, 2005.

[33] R. Rigler, Z. Foldes-Papp, F.-J. Meyer-Almes, C. Sammet, M. Volcker, and A. Schnetz. Fluorescence cross-correlation: A new concept for polymerase chain reaction. *J. biotechnol.*, 63(2):97–109, 1998.

[34] P. Schwille. Cross-correlation analysis in FCS. In R. Rigler and E.S. Elson, editors, *Fluorescence Correlation Spectroscopy: Theory and Applications*, pages 360–378. Springer, 2001.

[35] J. W. D. Comeau, S. Costantino, and P. W. Wiseman. A guide to accurate colocalization measurements. *Biophys. J.*, 91(12):4611–4622, 2006.

[36] K. N. Storch, D. J. Taatjes, N. A. Bouffard, S. Locknar, N. M. Bishop, and H. M. Langevin. Alpha smooth muscle actin distribution in cytoplasm and nuclear invaginations of connective tissue fibroblasts. *Histochem. Cell Biol.*, 127(5):523530, 2007.

[37] M. Franz, T. Hansen, L. Borsi, C. Geier, P. Hyckel, P. Schleier, P. Richter, A. Altendorf-Hofmann, H. Kosmehl, and A. Berndt. A quantitative co-localization analysis of large unspliced tenascin-C_L and laminin-5/γ2-chain in basement membranes of oral squamous cell carcinoma by confocal laser scanning microscopy. *J. Oral Pathol. Med.*, 36(1):6–11, 2007.

[38] S. V. Costes, D. Daelemans, E. H. Cho, Z. Dobbin, G. Pavlakis, and S. Lockett. Automatic and quantitative measurement of protein-protein colocalization in live cells. *Biophys. J.*, 86(6):3993–4003, 2004.

[39] E. M. M. Manders, J. Stap, G. J. Brakenhoff, R. Van Driel, and J. A. Aten. Dynamics of three-dimensional replication patterns during the S-phase analyzed by double labeling of DNA and confocal microscopy. *J. Cell Sci.*, 103(3):857–862, 1992.

[40] E. M. M. Manders, F. J. Verbeek, and J. A. Aten. Measurement of co-localization of objects in dual color confocal images. *J. Microsc.*, 169:375–382, 1993.

[41] L. M. Lifshitz. Determining data independence on a digitized membrane in three dimensions. *IEEE Trans. Med. Imaging*, 17(2):299–303, 1998.

3

Materials and Methods

3.1 *Computer Simulated Images with Interacting Populations of Point Emitters*

All the computational work, including image simulations, correlation function, and automatic colocalization calculations, was performed using custom written MatLab 7.0 (TheMathWorks, Natick,MA) routines and two toolboxes (Image Processing Toolbox and Optimization Toolbox) running on a personal computer equipped with a 1.5 GHz processor and 512 Mbytes of RAM. Computer simulated images were created to model those obtained with a two channel CLSM of fluorescently tagged membrane receptors in two-dimensional cellular membranes and the simulations were run with user set particle densities and interaction fractions. Three matrices were created in the image simulations. Matrix **C** contained the locations of the colocalized point emitters, with particle positions being generated by randomly choosing both x and y coordinates within a $N_x \times N_y$ matrix (usually 256×256 for most studies). Ones were inserted into the matrix at the randomly selected particle positions, while all other matrix elements were set to zero. It is possible that the same coordinates may be chosen at random more than once, especially at higher particle densities. In this case, the recorded value was the sum of the unity values for each particle located at that position, thus simulations did not model excluded volume effects. Matrix **C** was then convolved with a two-dimensional Gaussian function with an e^{-2} radius of

five pixels to simulate excitation of point emitters with a focused TEM_{00} (Gaussian) laser beam typical of CLSM imaging. Two more image matrices, **G** and **R**, with variable particle numbers were generated in the same fashion as **C** to represent the noninteracting components imaged in each detection channel. The addition of the colocalized particle matrix, **C**, to each of the noninteracting particle matrices, **G** and **R**, resulted in two images with a known percentage of interaction and fully defined particle densities. The interaction fraction, with respect to channel G, is given by $N_C/(N_C + N_G)$, while that of channel R is given by $N_C/(N_C + N_R)$, where N_i is the number of species, $i = C$(colocalized), G(green), R(red), per image.

Both ICCS and automatic threshold colocalization determination were then applied to these two images and the results analyzed. Between 20 and 100 images were generated for each set of simulation parameters so that statistics could be calculated for each colocalization method and their accuracy and precision could be compared.

To study the effects of photon detection shot or counting noise, a noise matrix was added to each image before the colocalization analyses were performed. The noise matrices, **U** and **H**, consisted of random numbers with a Gaussian distribution around zero and a standard deviation of one, multiplied by the square-root of the pixel intensity. The standard deviation of this matrix was varied with a scaling coefficient defined as the width factor (*WF*). The *WF* represents the ratio of the real PMT signal intensity standard deviation to that of a purely Poisson distribution to model analogue detection typical of a CLSM. Therefore, the intensities, $K_{x,y}$ and $L_{x,y}$, of each pixel (x, y) in the final image set were defined as follows,where $a_{x,y}$ and $b_{x,y}$ are the image matrix elements with known interaction fraction as described above:

$$K_{x,y} = a_{x,y} + WF_K\sqrt{a_{x,y}}u_{x,y}$$

$$L_{x,y} = b_{x,y} + WF_L\sqrt{b_{x,y}}h_{x,y}$$

The effects of uniform background noise were investigated by adding different

noise matrices, **U** and **H**, to each image. For background noise, the noise matrix elements were randomly chosen from the absolute values of a normal distribution with a mean of zero and a standard deviation of one. The standard deviation of the normal distribution was varied with a scaling coefficient to alter the total amount of noise present in the final images. This approach simulates the residual background count left after subtraction of a mean background from each pixel, as is standard practice for image background correction. Using this definition of background noise, the final pixel values in each image were defined as follows:

$$K_{x,y} = a_{x,y} + \sigma_K u_{x,y}$$

$$L_{x,y} = b_{x,y} + \sigma_L h_{x,y}$$

The signal/noise ratio in a simulation image set was then defined as the ratio of the signal (maximum of image matrix **A** or **B**) to the standard deviation of the noise (σ). In practice, the signal is calculated as the mean of the most intense pixels to help minimize the artifacts introduced by abnormally bright pixels,

$$S/B_{K \text{ or } L} = \frac{max\,(\mathbf{A} \text{ or } \mathbf{B})}{\sigma_{K \text{ or } L}}.$$

To simulate images resulting from a species with two binding sites for a particular ligand, Eq. 6.9 was used to calculate the expected distribution of interacting complexes given the single site-binding constant, K_C, the amount of free ligand, N_{RFree}, and the total number of target molecules, N_{GTotal}, (the molecule with two binding sites). The x and y pixel coordinates were generated as described above for the free receptor molecules (only channel 1), the free ligand molecules (only channel 2), and the interacting molecules, $N(GR_1)$ and $N(GR_2)$, (channels 1 and 2). To generate the image from channel 1, ones were placed at the pixel coordinates of the free target molecules as well as at the locations of all the interacting species. The channel 2 image was generated similarly, by placing ones at the pixel coordinates of the free

ligand and the interacting $N(GR_1)$ species. In addition, twos were placed at the pixel locations of the $N(GR_2)$ particles to simulate a twofold increase in brightness when two ligands are bound to one target molecule.

3.2 Antibodies

The primary antibody used for cell labeling and *in vitro* controls was a monoclonal anti-platelet derived growth factor β-receptor (IgG PDGF-β 4.3 mg IgG/mL) (isotype 2b), and was purchased from Sigma-Aldrich (Cat. No. P7679, St. Louis, MO). The primary antibody binds to an epitope located on the extracellular domain of the PDGF-β receptor and only recognizes human and pig receptors. One of the secondary antibodies used for immunofluorescent staining of the primary IgG was a fluorescein isothiocyanate (FITC) conjugated goat anti-mouse IgG (Fab-specific, Cat. No. F5262, Sigma-Aldrich). It had a protein concentration of 4.7 mg/mL, a dye/protein molar ratio of 5, and showed no binding to the Fc fragment. The other secondary antibody used in these experiments was Alexa Fluor 633 goat anti-mouse IgG_{2b} (Fc-specific, Cat. No. A-21146, Molecular Probes, Eugene, OR). The Alexa Fluor 633 conjugated antibody had a concentration of 2 mg/mL and a dye/protein molar ratio of 2.

3.3 Antibody Adsorption on Glass

The primary antibody was diluted 1:1000 in phosphate-buffered saline (PBS, pH 7.4) and incubated for 20 min at room temperature on a 35 mm, No. 1.5 glass-bottom microwell dish (P35G-1.5-14-C, MatTek, Ashland, MA). The dishes were then rinsed twice with PBS. Both the FITC and Alexa 633 conjugated secondary IgGs were mixed and diluted 1:1000 in PBS. This mixture of secondary antibodies was then incubated on the microwell dish at room temperature for times ranging from 15 min to overnight. Control measurements were performed without the presence of primary antibody (i.e., a mixture of fluorescent secondary antibodies was adsorbed on bare

glass surface). The spreading of the solution on the surface was greatly reduced when the primary IgG was not present, and resulted in large clusters of antibody. This was significantly different than samples prepared in the presence of the primary mouse IgG, which resulted in complete spreading on the glass surface and completely uniform secondary antibody distributions.

3.4 Cell Culture and PDGF-β Labeling

Human foreskin fibroblasts (AG01523) were purchased from the NIA Aging Cell Culture Repository, Coriell Institute for Medical Research (Camden, NJ). The cells were cultured in Dulbeccos Modified Eagles Medium supplemented with 10% fetal bovine serum, 4 mM L−glutamine, 100 units/ mL penicillin, 0.1 mg/mL streptomycin, and 0.1 mM nonessential amino acids (Gibco, Carlsbad, CA). Cells were maintained in a humidified 5.0% CO_2 atmosphere at 37°C. Cells were plated on 35 mm microwell dishes (MatTek) and grown for 2-3 days. Cells were incubated with 50 ng/mL of platelet-derived growth factor-BB (PDGF-BB) (R&D Systems, Minneapolis, MN) for 60 min at 37°C to promote clustering of the PDGF-β receptors [1]. Cells were rinsed once with PBS and then fixed with 4% (w/v) paraformaldehyde for 20 min at room temperature. Cells were incubated with 0.2% (v/v) Triton X-100 (Sigma-Aldrich) for 5 min at room temperature followed by rinsing three times with PBS. To reduce nonspecific antibody binding, cells were incubated for 30 min with 1% (w/v) bovine serum albumin (BSA) (Sigma- Aldrich) in PBS at room temperature. Cells were then incubated with IgG PDGF-β diluted 1:500 in 1% BSA for 40 min and washed with PBS. Goat anti-mouse IgG FITC conjugate was diluted 1:200 in 1% BSA and incubated 40 min followed by rinsing in PBS. The final step in the labeling process was to incubate the cells for 40 min with goat anti-mouse IgG Alexa 633 conjugate diluted 1:200 in 1% BSA followed by rinsing in PBS. Control samples were prepared in the same manner just described, except labeling with the primary IgG PDGF-β antibody was omitted.

3.5 Transfection of YFP-Talin constructs in CHO-K1 cells

Chinese hamster ovary (CHO-K1) cells (Sigma-Aldrich) were cultured in Dulbeccos Modified Eagles Medium supplemented with 10% fetal bovine serum, 4 mM L−glutamine, 100 units/ mL penicillin, 0.1 mg/mL streptomycin, and 0.1 mM nonessential amino acids (Gibco, Carlsbad, CA). Cells were maintained in a humidified 5.0% CO_2 atmosphere at 37°C. Cells were plated on 6-well dishes (VWR) and grown for 2 days. Two solutions were prepared for each well to be transfected (12 solutions total). The first set of solutions was prepared by diluting 5 μL of lipofectamine (Invitrogen, Carlsbad, CA) in 50 μL of OptiMEM (Invitrogen). The second set of solutions was prepared by diluting 1 μL DNA plasmid endcoding for YFP-talin (Prof. Horwitz Lab, University of Virginia) in 50 μL OptimMEM. These two sets of solutions were mixed and left at room temperature for 20 min. The resulting 100 μL lipofectamine/DNA solutions were then added to the 6-well plates containing the cells, and were incubated for 6 h at 37°C, and 5.0% CO_2. After the 6 h incubation time, the liquid was removed from each well and replaced with normal growth media. After 25 h, the cells were removed from the surface of the 6-well plate by addition of a 0.25% (w/v) trypsin solution. The cells were then incubated at 37°C on 35 mm microwell dishes (MatTek) that had been coated with fibronectin. These dishes were coated by incubation for 1 h at 37°C with a 2 μg/mL solution of fibronectin in PBS. The cells were then fixed with a 4% (w/v) paraformaldehyde solution for 10 min at room temperature and imaged using an Olympus FV300 (Olympus America, Melville, NY) confocal laser scanning microscope (CLSM), as described in the next section.

3.6 Microscopy

Human foreskin fibroblast cells as well as antibodies adsorbed on glass were imaged using an Olympus FV300 (Olympus America, Melville, NY) CLSM. Simultaneous excitation of FITC and Alexa 633 was provided by the 488 nm line of an Ar ion laser as well as the 633 nm line of a HeNe laser, respectively. Emission from both

dyes was collected with an Olympus 60x PlanApo oil immersion objective (NA 1.4). The resulting fluorescence was split with a 570 nm dichroic mirror, and wavelengths between 510 nm and 530 nm were selected using BA510IF and BA530RIF emission filters (Chroma, Rockingham, VT) and detected with a PMT. Longer wavelength emission was collected using another PMT and a LP660 filter (Chroma Technology, Rockingham, VT). The PMT voltages were adjusted such that no pixels were saturated in the image and no threshold was applied. The pixel resolution for cell images was 0.23 μm/pixel while a digital zoom was used to achieve a resolution of 0.058 μm/pixel for images of the antibody on glass. Mean background intensity levels were calculated from image regions outside of the cells. For the case of antibody adsorption on glass where the entire field of view appeared to contain signal, a region in the middle of the image was deliberately photobleached and the post-bleach mean intensity in that region was used as a measure of background noise. Identical background levels were obtained for control images of primary antibody-coated coverslips in the absence of the fluorescent secondary antibody. All images before ICCS or automatic colocalization analysis were corrected for background noise by subtracting the mean background, plus one standard deviation from all pixels. Bleedthrough between channels was measured by excitation with the 488 nm laser line and collecting the resulting fluorescence in both channels. No detectable cross talk was observed for these experiments.

The CLSM analogue noise width factor was measured at a particular PMT voltage by recording images of a sample slide with a high concentration of embedded fluorophore (Chroma Technology), and then comparing the standard deviation of the image to the square root of the mean.

CHO-K1 cells that were transfected with YFP-talin protein fusion constructs were imaged using the Olympus FV300 CLSM described above. YFP was excited using the 514 nm laser line of an Ar ion laser. Emission was collected with an Olympus 60x PlanApo oil immersion objective (NA 1.4). The resulting fluorescence was collected

using a 535-565 band pass emission filter (Chroma, Rockingham, VT) and detected with a PMT (V = 550). The pixel resolution was 0.12 μm/pixel.

Human embryonic kidney (HEK293) cells were plated on 35 mm glass-bottomed culture dishes and transfected with hemagglutinin-tagged angiotensin II type 1 receptor (HA-AT1R), β-arrestin2-CFP, small interfering RNA (siRNA) β2-adaptin and wild-type siRNA resistant β2-adaptin-YFP or Y737F mutant. The HEK293 cells were imaged at several time points following addition of a 1 μM solution of angiotensin II (Ang II) using a Zeiss LSM-510 Meta laser scanning microscope (Carl Zeiss Canada Ltd., Toronto, Ontario). Excitation of cyan fluorescent protein (CFP) and yellow fluorescent protein (YFP) were provided by the 458 nm and 514 nm lines, respectively, of an argon-ion laser. Emission from both dyes was collected with a Zeiss Plan-Neofluar 40x oil immersion objective (NA 1.3) and was split into two detection channels with a 490−nm dichroic mirror. Further wavelength selectivity was provided in the CFP channel by use of a 470-500 nm band pass filter and in the YFP channel by use of a 530-600 nm band pass filter. Fluorescence in both channels was recorded with two separate PMTs whose voltage was adjusted to obtain maximal signal but avoid large numbers of saturated pixels. Two adjustable pinholes were set at 90 μm and 76 μm for the CFP and YFP channels respectively. The pixel resolution varied between images from 0.08-0.11 μm/pixel. Due to the overlap between the emission spectra of CFP and YFP, images were recorded in multi-track mode to ensure no bleedthrough of the CFP emission into the YFP detection channel. In this mode, each detection channel image is acquired sequentially on a line-by-line basis. A single line scan of the sample is performed with the 458 nm laser line, which in turn, is followed by a single line scan with the 514 nm laser line. Since at no time do both lasers excite the sample simultaneously, the detection of CFP in the YFP channel is greatly reduced, which facilitates subsequent colocalization analysis of the acquired dual-channel images.

Prior to ICCS analysis, images were corrected for background noise by subtracting the mean plus one standard deviation of the noise from all pixels as measured from

image regions outside of the cell. S/B ratios were calculated from the maximum of the image and the remaining standard deviation of the noise following background correction. For each time point recorded following the addition of Ang II, ICCS measurements were performed on manually selected areas of the cell. Approximate locations and sizes of the selected areas were kept as similar as possible but due to the large alterations in cell shape following stimulation with Ang II it was impossible to perform the ICCS analyses on identical regions of the cell.

Bibliography

[1] A. Tingstrom, C. Reuterdahl, P. Lindahl, C.-H. Heldin, and K. Rubin. Expression of platelet-derived growth factor-β receptors on human fibroblasts. Regulation by recombinant platelet-derived growth factor-BB, IL-1, and tumor necrosis factor-alpha. *J. Immunol.*, 148(2):546–554, 1992.

4

Accuracy and Dynamic Range of Colocalization Measurements

Since the theory of image cross-correlation spectroscopy was established over a decade ago, only a handful of experiments have been performed to date [1, 2], and the possibility of measuring interactions in single images using spatial ICCS in particular, has not been extensively investigated. In order to unequivocally demonstrate the fact that ICCS is a viable technique for assessing the amount of colocalization present between two fluorescently tagged species imaged at high particle densities, and, for the first time, to determine the dynamic range and accuracy of ICCS for such measurements, a complete systematic study of the spatial fluctuation correlation technique was performed with comparison to a more commonly employed automatic colocalization method.

In order to fully characterize the statistical accuracy and dynamic range of ICCS, hundreds of simulated images were created and analyzed under varying conditions of particle number densities, interaction fractions, and noise levels. Simulations are essential in such a study to provide the level of control necessary to assess the quality of the technique employed in recovering the simulation input parameters. For the details of how the simulated images were created the reader is referred to the Materials and Methods section (3.1).

Some example simulation images created to model a sample consisting of two fluorescent species with 50% interaction (i.e half of the particles share complete spatial overlap) detected in two separate detection channels of a confocal laser scanning microscope are shown in Fig. 4.1. The total input particle surface numbers for the

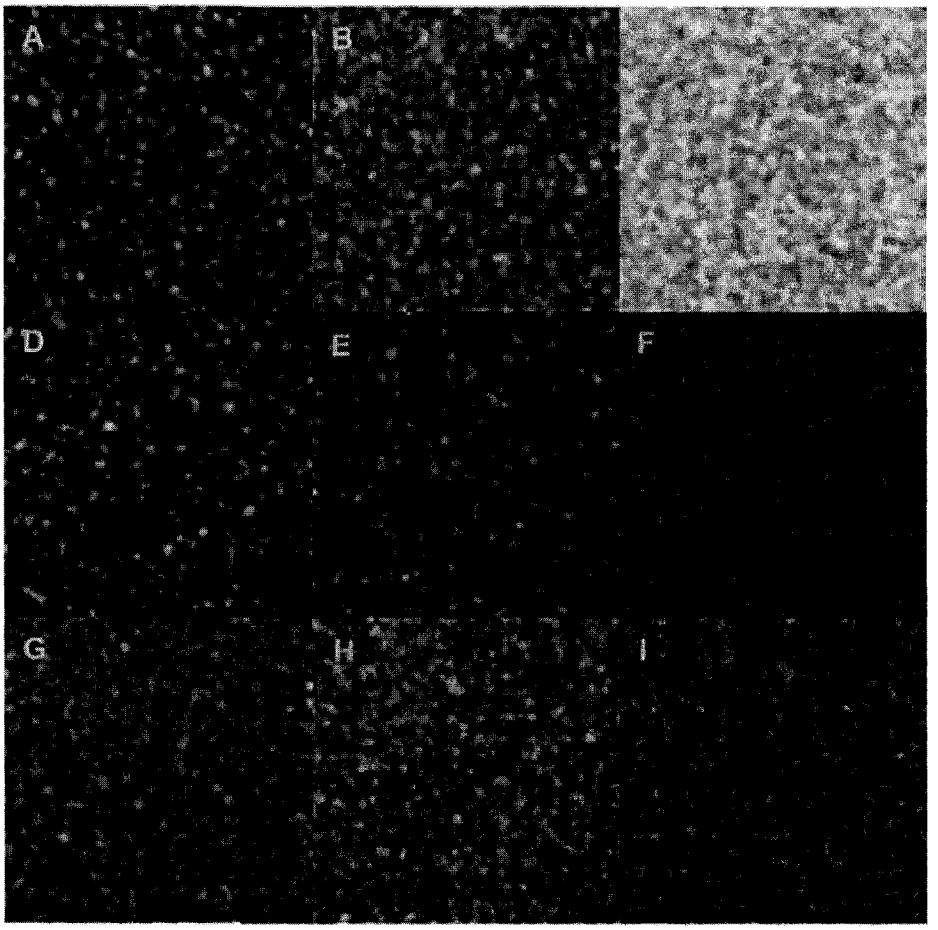

Figure 4.1: Simulated overlay images of two particle populations detected in two channels corresponding to a 50% interaction fraction between the two interacting species. The two-channel overlaid images consist of N_t total particles, $N_t/4$ are noncolocalized for each color (red and green), and $N_t/4$ particles are colocalized, with each color emitting equal intensity signals for both channels, which appear as yellow (i.e, $N_1 = N_2 = N_t/2$). The particles were randomly distributed in an image matrix of 256×256 pixels, and convolved with a Gaussian function with e^{-2} radius of 5 pixels. The first row shows different particle densities per image all with 50% interaction. (A) $N_t = 2 \times 10^3$ (2.4 particles/BA), (B) $N_t = 2 \times 10^4$ (24 particles/BA) (C) $N_t = 2 \times 10^5$ (240 particles/BA). In the second row, background noise was added to images with $N_t = 2 \times 10^3$ as described in Materials and Methods. (D) $S/B = 190$, (E) $S/B = 14$, (F) $S/B = 1.7$. In the third row, the counting noise WF was varied in images with $N_t = 2 \times 10^4$. (G) $WF = 1$, (H) $WF = 5$, (I) $WF = 15$.

images shown in Fig. 4.1 A-C, were 2×10^3, 2×10^4, 2×10^5 particles, respectively, per 256×256 pixel array, which corresponds to 2.4, 24 and 240 particles/beam area (BA), due to the fact that the area of the Gaussian convolution function (simulated BA) that was used to create these images was 78.5 pixels^2. Most subsequent references to particle densities will be expressed in units of particles/BA because, as shown explicitly in the following section, the BA represents a single spatial fluctuation sample, and is therefore an important parameter in the characterization of ICCS accuracy and precision. The channel 1 particles are displayed as green, channel 2 particles as red, and the overlay image of the two contains yellow pixels as a visual aid in identifying areas of colocalization. It becomes obvious that at higher particle number densities (Fig. 4.1 C), yellow pixels dominate the display, and it is therefore extremely difficult to distinguish, by eye, any true colocalized areas from regions with randomly overlapping independent particles.

4.1 Simulation Results

4.1.1 Colocalization Detection Limits

To investigate the minimum interaction fraction (IF) that can be detected by the two colocalization analyses, images were simulated in which the interaction fraction was varied while the total particle densities in channels 1 and 2 were held constant and equal. This procedure was repeated at different total particle densities in each channel (but still equal numbers per channel) in order to see if the overall particle density had any effect on the measured detection limit.

Automatic colocalization led to accurate results at low densities for all interaction fractions > 3% which is the detection limit as determined by the colocalization significance test described in Section 2.3.1. At higher particle densities (~100 particles/BA), automatic colocalization significantly overestimates the amount of interacting particles at large interaction fractions (> 60%), but the detection limit remains at 3% (Fig. 4.2). The standard deviation of the measurement was calculated from

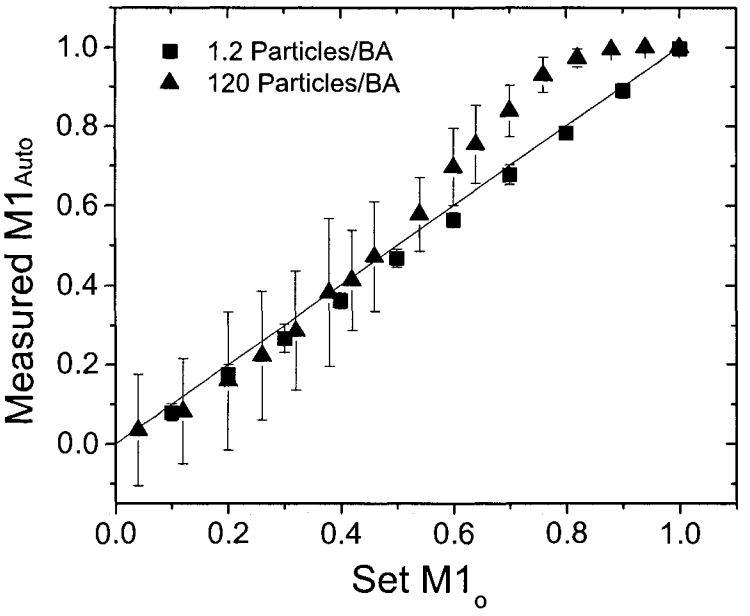

Figure 4.2: Automatic colocalization measured interaction fractions (IF) ($M1_{Auto}$) as a function of the simulation input interaction fraction, $M1_0$ for two different particle densities. Each point is an average of 50 image sets with error bars representing the standard deviation of the measurements.

the results of 50 simulations under identical conditions for each data point and was seen to increase with increasing particle density.

The detection limits of spatial ICCS were significantly worse than those of automatic colocalization, varying from between 5% for 512×512 pixel images to almost 75% for the much smaller 16×16 pixel images. These values were not dependent on the total particle density per channel, which was varied from < 0.1 particles/BA to 120 particles/BA. The minimum interaction fraction that could be detected by ICCS was determined by successively decreasing the number of interacting particles for a given particle density until the two-dimensional Gaussian fit of the cross-correlation function failed (Fig. 4.3). A failed fit was defined as more than half of the 20 trials returning a fitted e^{-2} beam radius outside a range of ±50% of the simulation input value, or the fitted peak position, (υ, ν), was shifted by more than 2 pixels from the center, $(\xi = 0, \eta = 0)$. This second criterion was included because it was found that in some instances, large off-center peaks would appear as well-defined Gaussian func-

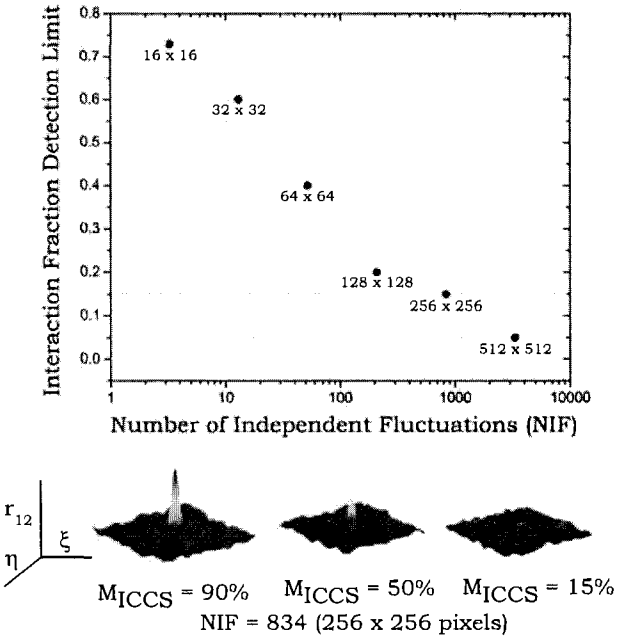

Figure 4.3: The minimum interaction fraction that could be detected using ICCS analysis as a function of the number of independent fluctuations (NIF) in the analyzed images. Both channel densities were held constant and equal (8 particles/BA) as the number of interacting particles was decreased. The minimum IF was determined by successively decreasing the number of interacting particles until the two-dimensional Gaussian fit of the cross-correlation function failed (i.e. the detection limit was reached when more than half of the 20 trials returned a fitted e^{-2} beam radius outside a range of $\pm 50\%$ of the simulation input value, or the fitted peak position, (υ, ν), was shifted more than 2 pixels from the center, $(\xi = 0, \eta = 0)$. Shown below are three cross-correlation functions calculated for 256×256 pixel images at three different IFs. As the IF approaches values <0.15, the amplitude of the central peak of the cross-correlation function is reduced to the same level as that of the noise due to random spatial correlations

tions that would pertrub the fitting of the central peak. It should be noted that to obtain the ICCS detection limits reported, the full correlation function was cropped around the central peak before fitting of the Gaussian function. Excluding long-range correlations (large spatial lag values) led to better fits, especially as the interaction fraction was decreased. In all cases, the number of points fit was at least six-times that of the e^{-2} Gaussian convolution radius to ensure complete decay of the central, zero-lags, correlation peak. All interaction fractions above the limit of detection led to relative errors of $< 15\%$ for ICCS. The poorer ICCS detection limits as the size of the image is decreased is a direct result of the difference in the number of independent (spatial) fluctuations (NIF) sampled for different image sizes. The NIF is defined as the ratio of the total image area to the area of the Gaussian convolution function, which simulates the area of the beam focal spot, and represents one fluctuation area sampled [3]. Similarly, greater sampling of temporal fluctuations has been shown in FCS to increase the statistical accuracy of the measurement [4], which is analogous to the decrease in the interaction fraction detection limit shown here with increased spatial fluctuation sampling.

4.1.2 Dynamic Range

The effect of density on the accuracy of both types of colocalization methods was investigated by varying the particle density in both channels independently, while fixing the amount of interaction with respect to channel 1 at 50% ($M1 = 0.5$). This interaction fraction was chosen as it was above the measured detection limits and allowed a reasonable range of densities to be explored and still have interacting particles in the simulation images. The results of these simulations are summarized in the 2D surface plot in Fig. 4.4. From this plot it is possible to see that the correct result is obtained, with relatively low error over the entire particle density range, only when the density ratio between the two channels is <10. When the channel 1 to channel 2 density ratio is larger than one order of magnitude, it is not possible to fit

the spatial cross-correlation Gaussian function with the proper beam radius (±50% ω_{input}), and it becomes easy to reject the result with confidence. In this limit, the failed fit is due to the calculated correlation between randomly overlapping particles being approximately equal in magnitude to the correlation between truly interacting particles. This is demonstrated by the fact that it becomes increasing difficult to differentiate the central zero-lags peak of the cross-correlation function from the random noise due to the statistical correlations that occur over the entire spatial-lag scale (this can also be seen in Fig. 4.3). As shown in Fig. 4.4, however, the ratio between random and nonrandom correlation was only a function of the ratio of the densities between channels (i.e., when one of the interaction fractions is $< 5\%$) and not the total density, which allowed ICCS to provide accurate results at extremely high particle densities even when random overlap appears to dominate the overlay image by eye. The top right of the surface plot in Fig. 4.4 corresponds to densities one order of magnitude greater than those shown in the simulation image depicted in Fig. 4.1C.

The accuracy of automatic colocalization is more severely affected by the particle density of the two images than ICCS as shown in Fig. 4.5. The pronounced V-shape of this plot illustrates the fact that the absolute value of the relative error in $M1_{Auto}$ was small only when the particle densities in each channel were almost equal. As the density ratio of the two species of particles deviated from one, the absolute value of the relative error in $M1_{Auto}$ increased dramatically, up to ~80% when the particle density of channel 1 was only twice that of channel 2. It is important to note that even though the algorithm led to a relative error of 80% in this case, the colocalization significance test, which only gives an indication as to whether or not true colocalization exists, was positive and, therefore, the experimenter would have no way of knowing the result obtained was inaccurate. This is in stark contrast to ICCS analysis where large errors in the measured interaction fraction were not observed due to the failed fits that occurred well outside the depicted density range. The error

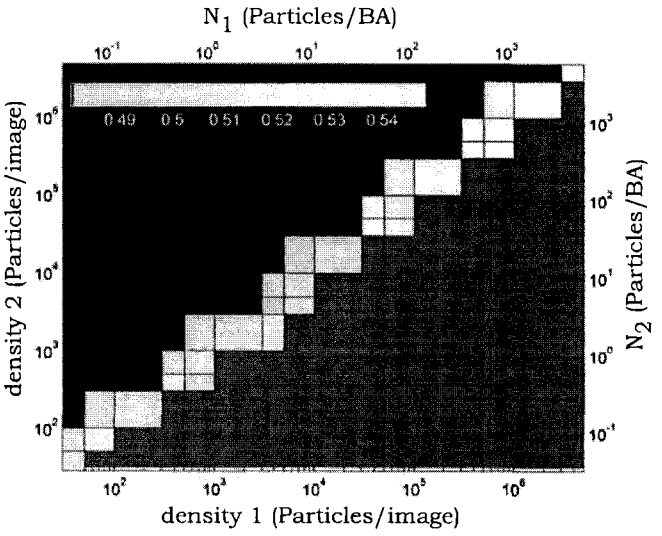

Figure 4.4: 2D Surface plot of the ICCS measured interaction fraction as a function of the densities of particles in both simulated image detection channels. The interaction fraction was set to 50% of channel 1 for all the simulations, and the total number of particles was varied independently for both types of particles. The bottom-right red area of the plot corresponds to regimes where the fit of a Gaussian to the spatial cross-correlation function failed and the upper-left black area to densities that cannot exist, given the restriction that 50% of the particles of channel 1 are interacting. The mean result for 50 trials for each set of conditions is plotted. The images consisted of 256×256 pixels, and the e^{-2} radius of the Gaussian convolving function was set to 5 pixels. ©Biophysical Journal 89, 1251-1260 (2005).

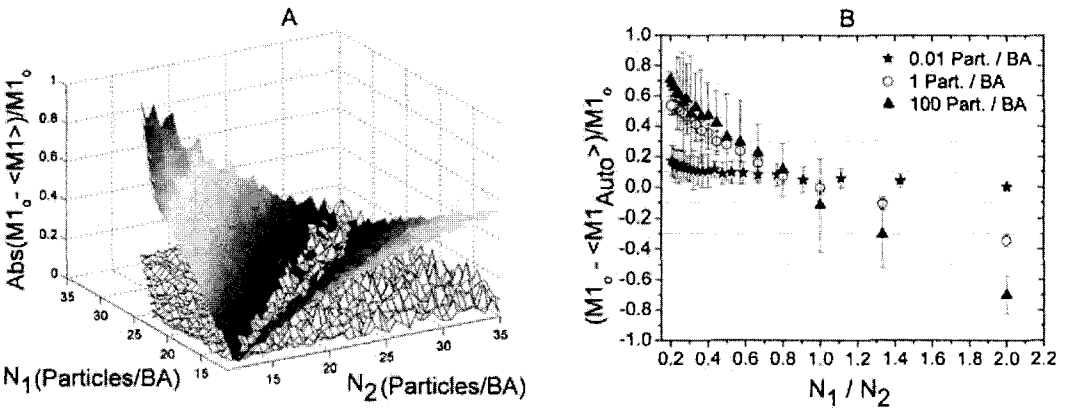

Figure 4.5: (A) Plot of the absolute value of the relative error in $M1_{Auto}$ (solid color) and $M1_{ICCS}$ (mesh) as a function of set particle density in each detection channel. Relative errors were calculated from the mean of 20 different sets of simulated images with an input $M1_0$ value of 0.5. (B) Plot of the relative error in $M1_{Auto}$ as a function of the particle density ratio between channel 1 and channel 2. $M1_0$ was set to 0.5 and $N1$ was kept constant at either 0.01 particle/BA, 1 particle/BA, or 100 particles/BA while $N2$ was varied. ©Biophysical Journal 91, 4611-4622 (2006).

in $M1_{ICCS}$ (Fig 4.4) over the density range investigated for automatic colocalization analysis is also plotted (mesh) in Fig. 4.5A for comparison purposes (note: in this case, the same image pairs were analyzed by both automatic colocalization and ICCS analysis).

It is not apparent in Fig. 4.5A, but the relative error in $M1_{Auto}$ was a function of the total density as well. This effect is shown more clearly in Fig. 4.5B by plotting the relative error in $M1_{Auto}$ as a function of the particle density ratio between channels for three different densities that span five orders of magnitude. Here, the particle density of channel 1 and $M1$ (0.5) were kept constant while varying the particle density of channel 2. For densities on the order of 0.01 particles/BA, the relative error in the automatic colocalization measurement was $< 15\%$ for all density ratios. As the total density increases, the slope of the line increases, which demonstrates an increased sensitivity to the density ratio between channels. The relative error was close to zero at a density ratio of one, but increased rapidly for larger and smaller ratios, reaching values of $> 50\%$ at a density ratio of 1:5 (Ch1/Ch2), when the total density was on the order of one particle/BA. The relative error at this N_1/N_2 ratio rose to even

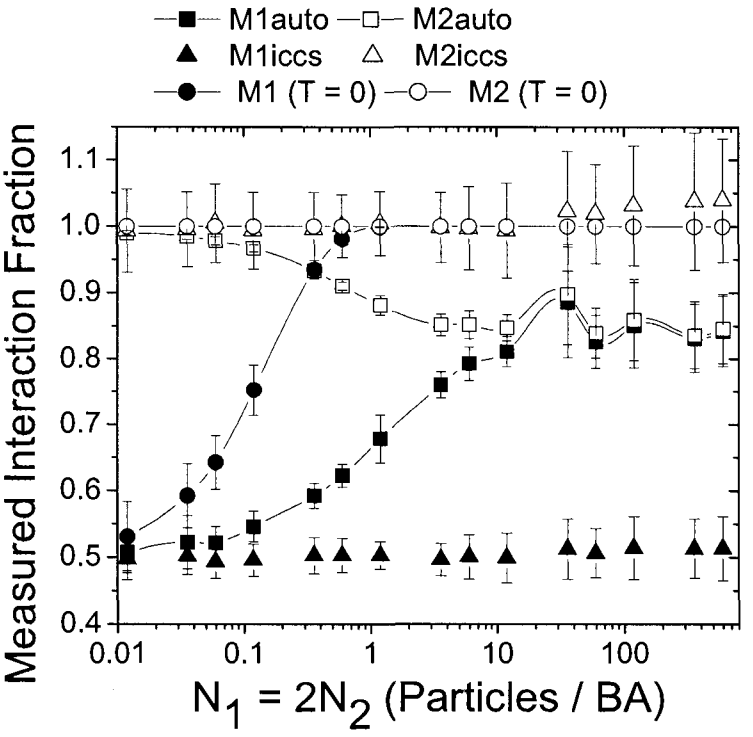

Figure 4.6: The measured interaction fraction calculated using ICCS, automatic colocalization and automatic colocalization with threshold zero (T=0) as a function of simulation set particle density. Each point is an average of 100 simulations, and error bars are the corresponding standard deviations. $M1_0$ and $M2_0$ input values were set at 0.5 and 1, respectively. ©Biophysical Journal 91, 4611-4622 (2006).

higher values as the total density increased. It should be noted that in all of the results, the relative error in $M2$ showed the same trends as that for $M1$.

Fig. 4.6 presents a more detailed view of the density dependence of the colocalization coefficients at a fixed N_1/N_2 ratio of 2, and clearly shows that as the density is increased, $M1_{Auto}$ and $M2_{Auto}$ converge to the same value, which is significantly different than the actual set interaction fractions, $M1_0$ and $M2_0$. In Fig. 4.6, $M1_0$ and $M2_0$ were held constant at 0.5 and 1, respectively, while the particle density was varied. When the density reached one particle/BA, the error in $M1_{Auto}$ had climbed to ~35% and leveled off at ~60% at densities > 10 particles/BA. At this density ratio, the calculation of $M1_{ICCS}$ and $M2_{ICCS}$ was accurate over all densities simulated. Also shown in Fig. 4.6 is $M1$ calculated with a colocalization threshold of zero

($M1$ ($T = 0$)), which has been used as a first approximation when the contribution from all noise sources was known precisely [5]. In this case, however, $M1$ is extremely sensitive to random particle overlap because all pixel pairs are classified as colocalized unless one of the pixels has a value of zero. $M1$ calculated in this manner classifies all randomly overlapping pixels as colocalized and therefore approached unity very quickly as the particle density increased. The same trend was observed when evaluating colocalization between two independent images of randomly distributed noninteracting particles using a threshold of zero, in which case, the measured interaction fraction rose steadily until reaching one at a density of ~0.6 particles/BA.

4.1.3 *Effect of Noise on Colocalization Measurements*

A careful consideration of noise contributions that are inherently present in real images is important to evaluate in any quantitative image analysis method. To simulate the overall uncertainty in analogue photon detection using a PMT on a CLSM, a counting noise width factor (WF) was introduced that broadens the underlying expected Poisson distribution that governs shot noise. The WF is intended to model the additional sources of noise inherent in photon detection on an analog CLSM system (i.e., signal amplification, digitization, etc.). It is not an attempt to model the underlying physical processes but rather simulate the overall statistical result observed in the acquisition of real CLSM images (see Materials and Methods 3.1, and Fig. 4.10).

Background noise is also considered that is uniform across the image and independent of the fluorescence signal in each pixel. The background noise simulates fluorescence intensity that remains after correcting images for noise through mean subtraction of a background. Real background noise originates from dark current, autofluorescence, or scattered light. In practice, both counting and background noise are present in real images simultaneously, but have been separated here to examine their contributions individually. In the following set of simulations, equal magnitudes of either counting or background noise were added to the images of channel 1 and

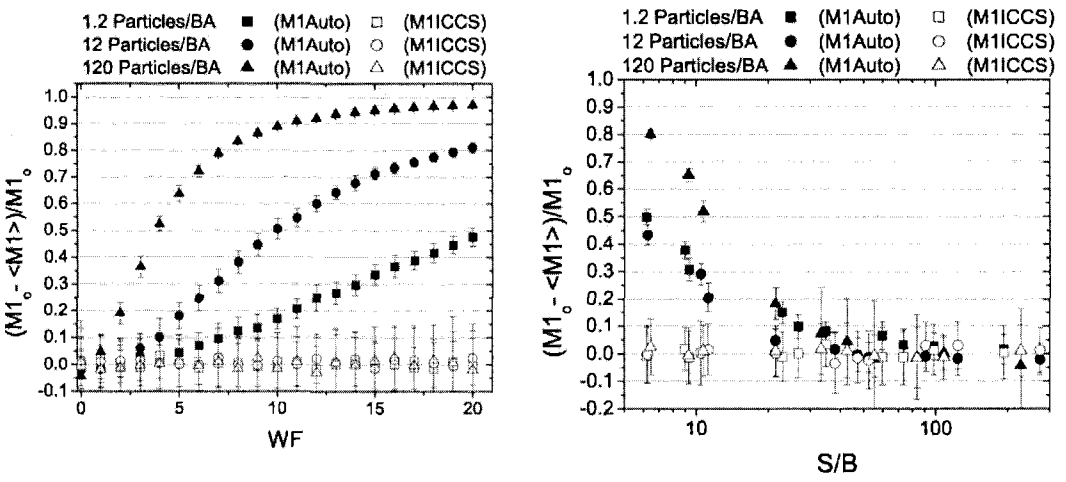

Figure 4.7: Plot of relative error in measured $M1$ as a function of the counting noise width factor (WF) (A) and the signal-to-background ratio of the image (S/B) (B). The densities in each channel were equal and $M1_0$ and $M2_0$ were both set at 0.5. Each point is an average of 50 simulations and the error bars are standard deviations. ©Biophysical Journal 91, 4611-4622 (2006).

channel 2.

The effect of photon counting noise on error in automatic colocalization measurements increases as the overall density is increased. This is demonstrated in Fig. 4.7A, where the relative error in $M1_{Auto}$ approaches 1 (i.e., $M1_{Auto}$ approaches 0), as a function of increasing width factor. As a consequence of the increased noise, r_P goes to zero at very high threshold values, which results in only a small fraction of pixels being identified as colocalized (i.e., above threshold). In contrast, the error in ICCS analysis is small and constant as a function of the width factor for all the densities investigated. Low signal-to-background (S/B) ratios will affect the error in $M1_{Auto}$, especially when the overall image density is large as shown in Fig. 4.7B. As was seen in the case of counting noise, the S/B ratio has little effect on the accuracy of the interaction fraction measured with ICCS. This is not the case, however, for the measured number densities. The error in the particle density measured by ICCS for each channel increases as the S/B decreases, and this effect is more pronounced for lower particle densities. For example, for lower densities ($<$ 10 particles/BA) with S/B

ratios < 10, the error in the measured absolute densities is > 60% for ICCS. At this same S/B ratio of 10, but densities > 100 particles/BA, the error in the measured absolute channel densities is $\sim$ 20%. Essentially, these errors cancel out when calculating the interaction fraction as long as the background noise in each channel is comparable.

In real images obtained using CLSMs or other types of imaging systems, however, the S/B ratio measured with respect to each detection channel, $(S/B)_1$ and $(S/B)_2$, will quite often differ by varying amounts. Therefore, in order to determine to what extent these differences in the S/B ratio alter the measured interaction fractions for both ICCS and automatic colocalization analysis, the S/B ratio was varied in each channel independently and both colocalization detection methods were applied to each set of two channel images simulated. The results are plotted in Fig. 4.8 where the densities of each image were held constant and equal at 1.2 particles/BA, and the amount of colocalization was set to 50% ($M1_0 = M2_0 = 0.5$). The diagonal of these plots, in which both images have equal S/B ratios, is equivalent to Fig. 4.7B, where we see that the absolute value of the relative error in $M1_{ICCS}$ is small (<5%) and constant, while the error in $M1_{Auto}$ increases to >50% when the S/B ratios of both channels are small but equal ($S/B < 10$). The more interesting result is illustrated by the off-diagonal values, in which the S/B ratios of each image are significantly different. In this case, we see that the error in both $M1_{ICCS}$ and $M1_{Auto}$ are quite similar, ranging from 20-60%, with the exception of the upper left corner of the plot ($(S/B)_1 << (S/B)_2$), where the error in $M1_{ICCS}$ is over three times larger than that of $M1_{Auto}$. This observation can be explained by the fact that $M1_{ICCS}$ is calculated from the ratio of the cross-correlated particle number density, N_{12}, to the total particle number density in channel 1, N_1. At low $(S/B)_1$ ratios, the error in N_1 is significantly larger than the error in N_{12}, which leads to very large errors in the calculated $M1_{ICCS}$ values. This also explains why the absolute error in $M1_{ICCS}$ as a function of both $(S/B)_1$ and $(S/B)_2$ is non-symmetrical around the diagonal. In fact, the magnitudes

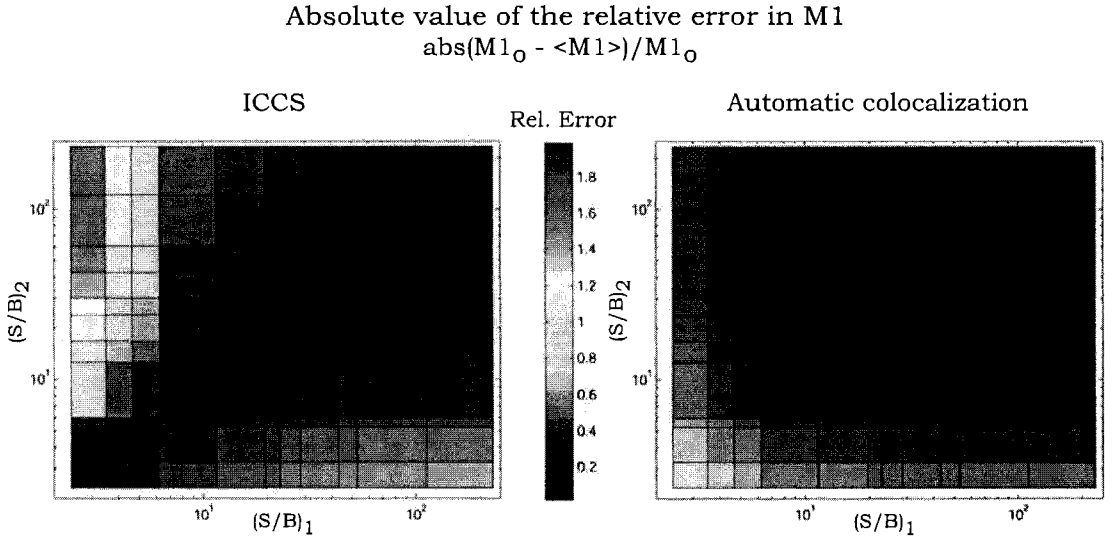

Figure 4.8: 2D surface plot of the absolute value of the relative error in $M1$ as a function of the signal to background ratio in each image, $(S/B)_1$ and $(S/B)_2$. The densities in each channel were 1.2 particles/BA and $M1_0$ and $M2_0$ were both set at 0.5. Each point is an average of 25 simulations.

of the absolute errors in $M2_{ICCS}$ were identical to those plotted in Fig. 4.8 except that the largest errors were found at the lower right corner where $(S/B)_1 >> (S/B)_2$.

Identical trends were observed in the relative error of $M1_{ICCS}$ and $M2_{ICCS}$ as a function of both $(S/B)_1$ and $(S/B)_2$ for greater total particle densities equaling 120 particles/BA. The magnitude of the relative errors, however, was $\sim$5 times lower in the highest-error regions of the surface plot than those measured for N_1 and N_2 densities of 1.2 particles/BA as described above. This is simply due to the fact that for a given S/B ratio, the error in any of the measured number densities, N_1, N_2, or N_{12}, is significantly lower as N increases. The relative error in $M1_{Auto}$ and $M2_{Auto}$ were relatively unchanged as a function of overall particle density.

Differences in the counting noise width factor, WF, between the two images had no effect on the measured ICCS interaction fractions, $M1_{ICCS}$ and $M2_{ICCS}$, which were determined with accuracies of <10% regardless of the respective WF channel values and irrespective of the particle densities in each channel. This is due to the fact that even high WF values led to relatively small errors in the measured number

densities. The error in M_{Auto} as a function of both WF_1 and WF_2 was similar to the errors plotted in Fig. 4.7A in that the error was relatively high, especially as the overall particle densities increased, as long as one of the images had an elevated WF value.

4.2 Experimental Results

4.2.1 Adsorption of Antibody on Glass

To examine the results of the simulations in the context of real systems with high particle densities imaged using a typical CLSM, fluorescently labeled antibodies adsorbed to a glass coverslip were imaged and analyzed for the presence of colocalization. After coating a coverslip with mouse monoclonal anti-PDGF β-receptor IgG, a mixture of secondary anti-mouse IgGs conjugated with either fluorescein isothiocyanate (FITC) or Alexa 633 (Fab- and Fc-specific, respectively) were incubated on the coverslip for varying amounts of time. The calculated colocalization, as measured by either ICCS or automatic colocalization analysis, is plotted as a function of secondary antibody incubation time in Fig. 4.9. ICCS analysis showed the expected increase in interaction fraction as the incubation time was increased. The overall density was between 100 and 400 particles/BA for each channel and automatic colocalization failed to detect any interactions for this high density sample.

In order to estimate the accuracy of these colocalization measurements by comparison to the simulation results under similar conditions, it was necessary to measure the contributions of both background and counting noise present in the recorded images. To estimate the S/B ratio of the images as defined in the Materials and Methods (3.1), the signal was calculated as the maximum image intensity due to the ease at which it can be measured, and the background as the standard deviation of an image area devoid of specific fluorescence signal. Due to the fact that the fluorescently tagged antibodies covered the entire field of view, the fluorescence signal was photobleached by repeating many scans and the mean intensity of the bleached region

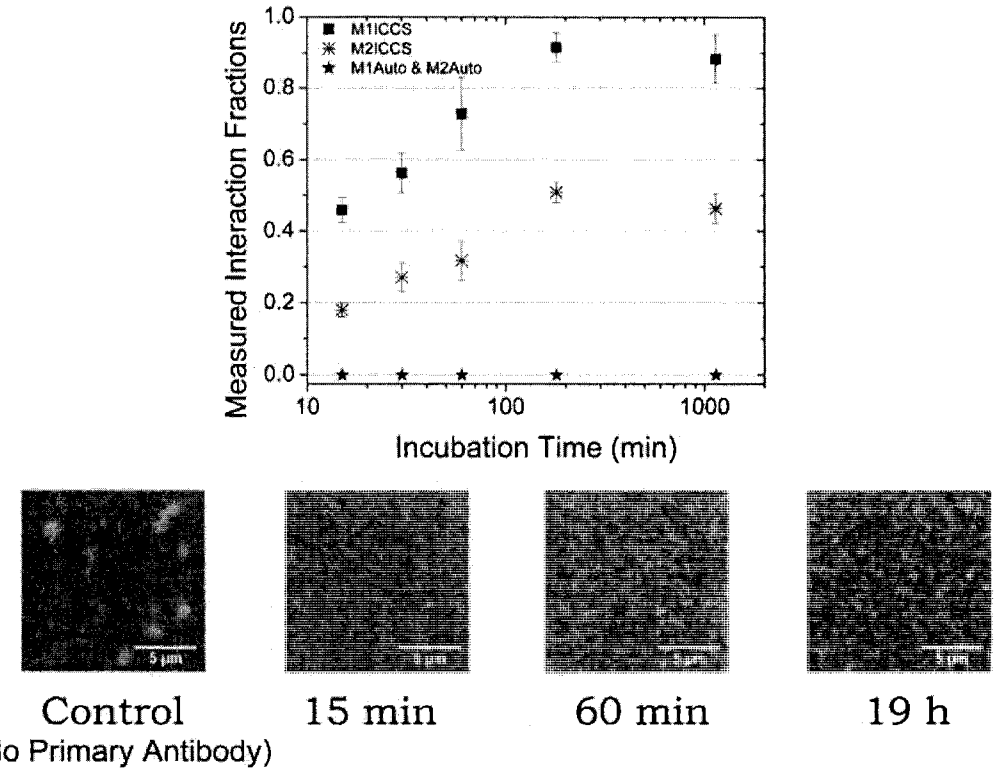

Figure 4.9: Plot of the measured interaction fractions as a function of incubation time for a secondary FITC goat-anti-mouse IgG (Fab-specific), and a secondary Alexa 633 goat-anti-mouse IgG (Fc-specific) incubated on a coverslip coated with mouse monoclonal IgG. Each point is an average of 10 dual color image analyses recorded from different regions of the sample. Error bars are propagated standard errors of the mean. Shown below are representative images taken at different incubation time points and a control image prepared in the absence of primary antibody, which shows significant clustering in contrast to the specifically bound antibodies. ©Biophysical Journal 91, 4611-4622 (2006).

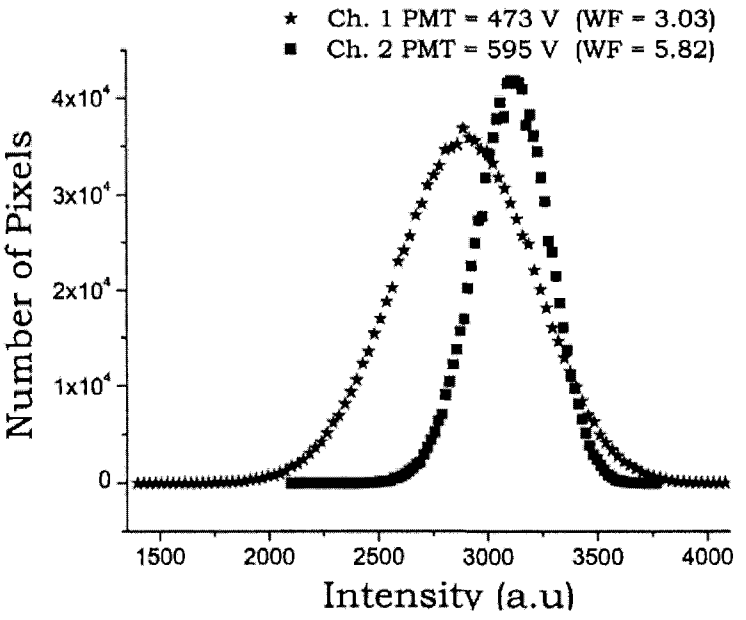

Figure 4.10: Fluorescence intensity histograms of images of highly concentrated fluorescence dyes recorded in the two detection channels used to collect fluorescence from FITC and Alexa 633 are plotted. The ratio of the standard deviation to the square root of the mean of these histograms was used as a measure of the CLSM width factors for the experimental set-up employed in the two-channel fluorescently tagged antibodies adsorbed on glass experiments.

was used as an approximation of the background noise. The signal/background ratio defined in this manner can be biased if there is an abnormally bright pixel in the image. This may occur as a result of random overlap of multiple molecules, especially at low particle densities. To verify that this was not the case, the mean of the 50 brightest pixels was taken as a measure of the signal and compared to that of using the global maximum as a measure of the signal. Both values were very similar and led to identical accuracies in these measurements. Unlike the S/B, the WF cannot be measured directly from acquired images, and was therefore evaluated for identical detector settings (PMT voltages) as those used in the antibody imaging by employing highly concentrated dye samples (3.6, Fig. 4.10).

At the measured densities of between 100 and 400 particles/BA determined from the autocorrelation amplitudes, and the measured noise levels, the error in ICCS was <10% ($S/B_1 = 69-158$, $S/B_2 = 100175$, and $WF_1 = 3.0$, $WF_2 = 5.9$), but automatic

colocalization greatly overestimated the colocalization threshold, which led to a severe underestimation of the interaction fraction ($M1_{Auto}$ and $M2_{Auto} = 0$). The difference in the $M1_{ICCS}$ and $M2_{ICCS}$ values shown in Fig. 4.9 are a result of the significantly greater amount of free red species (Alexa 633 IgG) compared to that of the free green species (FITC IgG). This trend was observed for several different initial concentration ratios between the red and green labeled antibodies for a given incubation time as well as for the PDGF-β labeling on human fibroblasts (see Fig 4.11). Control samples were prepared in the absence of the primary anti-PDGF β-receptor IgG antibody. For the control samples, the spreading of the secondary IgG mixture on the glass coverslip was significantly reduced and resulted in large clusters of antibody on the glass coverslip, which was considerably different than samples prepared in the presence of the primary antibody (see control image in Fig. 4.9).

4.2.2 *Analysis of PDGF-β Receptor Labeled AG01523 Human Foreskin Fibroblasts*

To compare the two colocalization methods for measurements at much lower particle densities than those described above for adsorption on glass, experiments were conducted on cells. The PDGF-β receptor expressed in chemically fixed AG01523 human foreskin fibroblasts was immunolabeled using the same antibodies as the previous experiment on glass, and hence tagged with the two distinct fluorophores, FITC and Alexa 633, and then imaged by CLSM. An overlay, two channel confocal image of the cells is shown in Fig. 4.11 with boxes to indicate the regions analyzed. In the region outlined by the blue box, the low density of the receptors ($\sim$0.01 particles/BA) is such that both methods give similar results. After correcting for background noise and nonspecific binding of antibodies, the following colocalization coefficients were calculated: $M1_{ICCS} = 0.98$, $M2_{ICCS} = 1.0$, $M1_{Auto} = 0.96$, and $M2_{Auto} = 0.94$. These coefficients are expected to be close to one because the cells were pretreated with PDGF-BB to promote clustering of the PDGF-β receptors. The images were

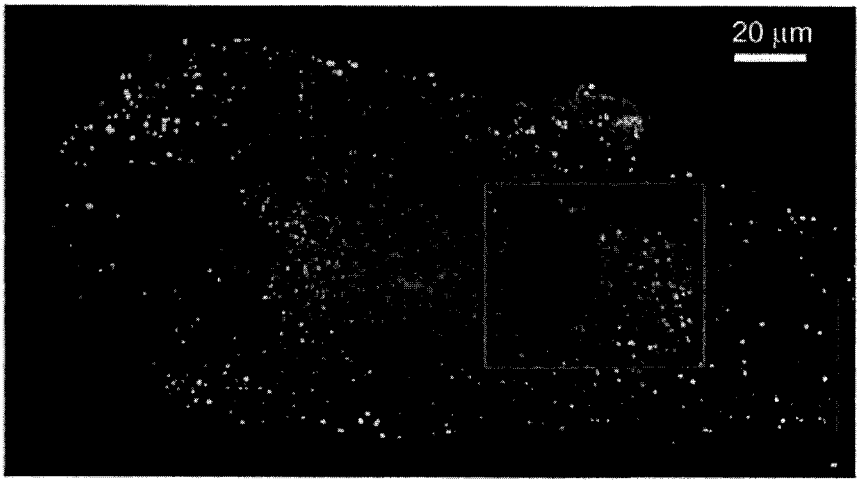

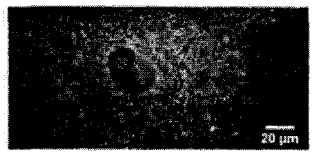

Nonspecific Binding Control

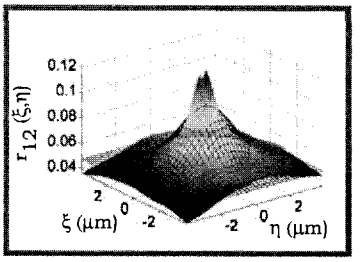

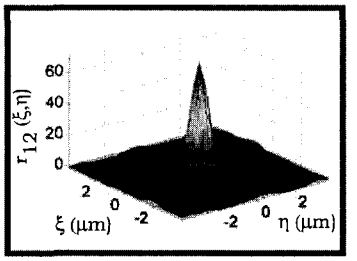

Figure 4.11: Two-channel overlay RGB image of PDGF-β receptors on human foreskin fibroblast cells immunolabeled with FITC (green) and Alexa 633 (red). The boxes indicate the regions chosen for colocalization analysis. Both methods lead to analogous results in the region indicated by the blue box ($M1_{ICCS} = 0.98$, $M2_{ICCS} = 1.0$, $M1_{Auto} = 0.96$, and $M2_{Auto} = 0.94$). ICCS fails in the region indicated by the red box due to the edge boundaries of the nuclear region while automatic colocalization works well in this regime ($M1_{Auto} = 0.92$ and $M2_{A}uto = 0.35$). Shown below are the corresponding spatial cross-correlation functions for the ICCS analysis of the two regions of analysis. The solid colored plot is the raw cross-correlation function and the mesh is the corresponding fit. Note the poor Gaussian fit of the nuclear region of analysis due to edge effects. A nonspecific control (no primary antibody) image is shown for comparison and was used to correct for nonspecific fluorescence signals. ©Biophysical Journal 91, 4611-4622 (2006).

corrected for nonspecific antibody binding before the colocalization analyses by subtraction of the mean intensity value of cells labeled in the absence of primary antibody. Some pixels, however, will still contain residual, nonspecific intensity contributions, especially when the measured nonspecific intensity distribution is broad. The red box indicates a region around the nucleus where ICCS analysis fails due to the heterogeneous nature of this part of the cell (edge boundaries). The corresponding correlation function is highly non-Gaussian due to the edges, which prevented fitting for the ICCS analysis. This type of situation is often encountered when the particle distribution in the region of analysis deviates from that of a purely uniform distribution. If it is not feasible to choose a more uniform area within the cell, then spatial ICCS is no longer a valid method for colocalization analysis and another technique should be used. It should be noted, however, that ICCS does not lead to false-positive results in these situations because the failed fit is readily apparent. On the other hand, automatic colocalization does not require a uniform distribution of labeled species, and successfully located the colocalized pixels for this lower density receptor system ($M1_{Auto} = 0.92$, $M2_{Auto} = 0.35$). The low value measured for $M2_{Auto}$ is a direct result of the larger amount of nonspecific binding of the Alexa 633 (red) tagged antibody that was observed around the nucleus, as compared with all other regions of the cell.

The results of this systematic study of the factors affecting colocalization measurements in fluorescence microscopy images are tabulated in Table 4.1. By applying spatial ICCS and automatic colocalization analysis to a range of simulated image sets, images of high density fluorescent antibodies and PDGF-β receptor labeled cells, we have developed important experimental guidelines to consider when performing fluorescence microscopy colocalization measurements. Taken together, automatic colocalization and ICCS provide a large dynamic range for accurate measurements within dual-color fluorescence microscopy images. This study demonstrated that the intrinsic variable of the particle number density, which is often overlooked, must carefully be considered when measuring colocalization.

	Automatic Colocalization	ICCS
Colocalization Detection Limit	$< 3\%$	75%-5% for NIF $\approx 3 - 3300$
Applicable Density Range	$\frac{N_2}{2} < N_1 < 2N_2$ at 1 particle/BA $N_1 = N_2$ at 100 particles/BA	$\frac{N_2}{10} < N_1 < 10N_2$ for all densities
Variable Binding Ratios	not applicable	$< 10\%$ error
Pixel Shifts	sensitive	not sensitive
Image Heterogeneity	not sensitive	sensitive

Table 4.1: Automatic Colocalization vs. ICCS

Bibliography

[1] C. M. Brown, M. G. Roth, Y. I. Henis, and N. O. Petersen. An internalization-competent influenza hemagglutinin mutant causes the redistribution of AP-2 to existing coated pits and is colocalized with AP-2 in clathrin free clusters. *Biochemistry*, 38(46):15166–15173, 1999.

[2] P.W. Wiseman, J.A. Squier, M.H. Ellisman, and K.R. Wilson. Two-photon image correlation spectroscopy and image cross-correlation spectroscopy. *J. Microsc.*, 200(Pt 1):14–25, Oct 2000.

[3] S. Costantino, J. W.D. Comeau, D. L. Kolin, and P. W. Wiseman. Accuracy and dynamic range of spatial image correlation and cross-correlation spectroscopy. *Biophys. J.*, 89:1251–1260, 2005.

[4] D.E. Koppel. Statistical accuracy in fluorescence correlation spectroscopy. *Phys. Rev. A*, 10:1938–1945, 1974.

[5] E. M. M. Manders, F. J. Verbeek, and J. A. Aten. Measurement of co-localization of objects in dual color confocal images. *J. Microsc.*, 169:375–382, 1993.

5

In vivo studies of AP-2/β-arrestin Complexes

In the previous chapter, important experimental guidelines were established for the application of ICCS and automatic colocalization methods to measure interactions from data sets of dual-color fluorescence microscopy images. These were established by systematically studying the dynamic range and accuracy of these techniques by both simulation and experimental approaches. It was clear that for fluorescence images with uniform particle distributions, ICCS led to lower errors than automatic colocalization under most of the experimental conditions investigated, such as, elevated noise levels, and differing particle number densities for each detection channel. In addition to the significantly lower error in the recovered interaction fractions under these experimental conditions, ICCS provides a built-in check as to whether it actually works under these conditions, because it returns a failed fit to the 2D spatial cross-correlation function when it is applied outside of its dynamic range. This is not the case for the automatic colocalization method, which will always return a value for the colocalization coefficients.

In this chapter, ICCS is applied to accurately measure interactions from single pairs of dual-color fluorescence images to determine the nature of the interaction between two important components of the clathrin-mediated endocytic pathway, which together, regulate the cell signaling activity of a large family of membrane receptors. By approaching these cellular measurements with a better understanding of the strengths and weaknesses of spatial ICCS, we were able to optimize the measurement and quantify the interaction between these two endocytic adaptor proteins in live

human embryonic kidney cells.

5.1 Introduction

G protein-coupled receptors (GPCRs) are the largest family of eukaryotic transmembrane receptors that regulate a wide variety of coordinated cellular responses to a large number of external stimuli. GPCRs are 'sensing' molecules that bind extracellular proteins or small ligand molecules in order to activate signal transduction pathways within the cell, which in turn, ultimately lead to specific cellular responses. Physiological responses derived directly from the activation of specific GPCRs include vision, olfaction, regulation of the immune system, neurological activity, as well as numerous other important processes (see [1] for review). Due to the wide array of processes regulated by GPCRs, deficiencies in these transmembrane receptors have been implicated in various disease states, and as such, are the target of a large fraction of the medicinal drugs available on the market today [2].

All GPCRs share a similar structure that consists of a single amino acid chain that spans the plasma membrane seven separate times, an extracellular ligand-binding domain, and an intracellular G protein-binding domain [3](Fig. 5.1). The extracellular binding of specific ligands (agonists) to GPCRs induces a conformational change within the intracellular domain of the receptor, thus enabling the binding of a receptor-specific G protein, i.e. a guanine nucleotide binding protein that resides on the cytoplasmic side and binds to the GPCR at the membrane. All heterotrimeric G proteins are structurally similar, consisting of three separate protein subunits, α, β, and γ, and function by similar mechanisms. The α subunit is bound to guanosine diphosphate (GDP) in the inactivated state and contains intrinsic GTPase activity, that is, the ability to catalyze the hydrolysis of guanosine triphosphate (GTP) to GDP. Binding of a G protein to the GPCR results in separation of the GDP-bound α subunit from the rest of the heterotrimeric G protein and exchange of GDP for GTP. The resulting 'activated' α and $\beta\gamma$ subunits dissociate from the GPCR and diffuse

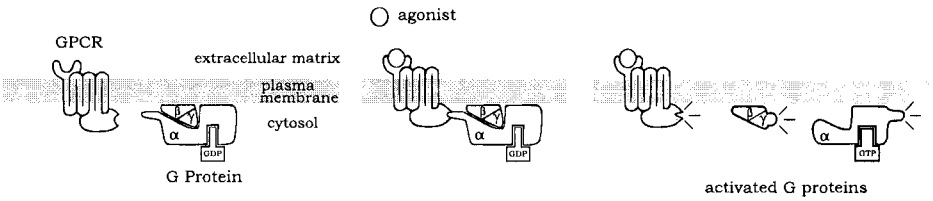

Figure 5.1: G protein-coupled receptors (GPCRs) are heptahelical transmembrane receptor proteins that transduce chemical stimuli into sensory signals within cells. Extracellular ligand binding induces conformational changes within the GPCR, which allows binding of a trimeric intracellular membrane-associated guanine nucleotide binding protein (G protein). This causes 'activation' of the G protein by separation of the α subunit from the $\beta\gamma$ subunit and exchange of guanosine diphosphate (GDP) for guanosine triphosphate (GTP). The activated G protein subunits interact with target molecules along the plasma membrane, which propagate the signal downstream to subsequent signaling molecules. The signal is 'shut off' by recombination of the two activated protein subunits, which is triggered by hydrolysis of GTP to GDP by the the GTPase activity of the α subunit. This process occurs on the order of a few seconds following activation of the G protein. Adapted from [4].

along the plasma membrane where they activate other target effector proteins by increasing their binding affinity for other secondary messenger molecules. The eventual hydrolysis of the bound GTP to GPD by the α subunit causes dissociation from the target protein and recombination of the α and $\beta\gamma$ subunits. This completes the activation/deactivation cycle of the G protein, which may be repeated by subsequent re-binding to the specific GPCRs that triggered the cycle initially. The activation of target proteins by the activated G protein subunits forms the basis of the initial steps in many cell signaling pathways that control many important physiological responses.

From the discussion above, it is clear that the *activation* of GPCRs is an extremely important signaling mechanism that occupies a central role in the regulation of many biochemical signaling pathways. Equally important, however, is the *deactivation* mechanism for GPCRs, which functions to reduce the coordinated cellular responses induced by the specific binding of extracellular ligands. A class of proteins called arrestins are entrusted with this critical task. Three types of arrestin proteins have been identified including those that regulate light responsiveness via interaction with rhodopsin (v-arrestin)[5], as well as β-arrestin1 and β-arrestin2, which together, regulate all other non-visual processes [6]. There are two mechanisms by which β-

arrestins desensitize GPCRs; first, by binding to activated, phosphorylated GPCRs thus preventing the binding and subsequent activation of associated G proteins, and secondly, by linking the receptor to elements of the endocytic pathway that results in its removal from the plasma membrane (internalization). The fate of internalized GPCRs is determined in subsequent steps along the endocytic pathway where they are processed for re-incorporation back into the membrane (receptor recycling) or the complete degradation of the receptor altogether in lysosomal compartments within the cell [7].

In addition to its role as a GPCR-desensitizing-endocytic adaptor protein, mounting evidence has shown that β-arrestin plays an active role in the various cell signal transduction pathways initiated at GPCRs, by sequestering several different types of signaling molecules to the activated receptors in an agonist-dependent manner [8]. Recruitment of the nonreceptor tyrosine kinase, c-Src, by β-arrestin for instance, facilitates activation of the well-studied mitogen-activated protein kinase (MAPK) signaling pathway, which results in cell division and differentiation [9]. The dual role of β-arrestin as both an endocytic and signaling adaptor has made this protein and its interacting partners the focus of many studies that attempted to unravel the key features of GPCR activation and deactivation [10–12].

5.2 β-arrestin Mediated Endocytosis

Endocytosis is the process by which cells actively transport material (e.g. small molecules, proteins, microorganisms) from the exterior to the interior of the cell without the need of direct passage through the non-polar environment of the plasma membrane. This occurs by invagination of the cell membrane, incorporating extracellular fluid in the process, which eventually pinches off from the membrane itself to form a lipid-bilayer bounded vesicle within the cytosol of the cell. Perhaps the most common method employed by cells to internalize various molecular species in a highly specific manner is through receptor-mediated endocytosis [13]. Receptor ligand

binding causes clustering of the receptors in small pits on the plasma membrane following the recruitment to, and 'coating' of, the intracellular membrane by a trimeric, triskelion-shaped protein known as clathrin. Development and growth of clathrin-coated pits causes the membrane to bend and invaginate, and within minutes leads to the formation of clathrin-coated vesicles (CCVs) composed of the regions of the membrane where the clathrin-coat was formed, thus facilitating the specific transport of receptors and ligands into the interior of the cell for further processing. The CCV endocytic pathway has been extensively studied and is responsible for transporting cholesterol that is present in low density lipoproteins in the blood stream to the interior of the cell through specific cell-surface receptors. The cholesterol is then used as an important component in future synthesis of the cell membrane [14].

An important component of CCVs is the heterotetrameric adaptor protein, AP-2, which links intracellular-destined membrane cargo to the clathrin lattice. This link is provided by direct interaction of the $\beta 2$ subunit of AP-2, $\beta 2$-adaptin, with both clathrin and specific amino acid sequences on the membrane receptor protein itself [15]. β-arrestin has also been shown to interact directly with $\beta 2$-adaptin [16], and mutants that lack the ability to bind to the AP-2 subunit fail to target GPCRs to clathrin-coated pits [17, 18].

A schematic diagram is shown in Fig. 5.2 outlining the sequence of events in β-arrestin mediated endocytosis following GPCR activation (associated G proteins are omitted for clarity). β-arrestin is a cytosolic protein that translocates to GPCRs following agonist binding and subsequent phosphorylation of the receptor by G protein-coupled receptor kinase (GRK) [21]. An important signaling kinase, c-Src, and the clathrin adaptor protein, AP-2, both of which can bind directly to β-arrestin, are sequestered to the phosphorylated GPCR-β-arrestin complex. This is followed by initiation of clathrin cage formation through direct interactions of $\beta 2$-adaptin (the $\beta 2$ subunit of AP2) as well as β-arrestin [19] with clathrin monomers, eventually leading to the formation of CCVs containing the entire complex, or, as is observed most

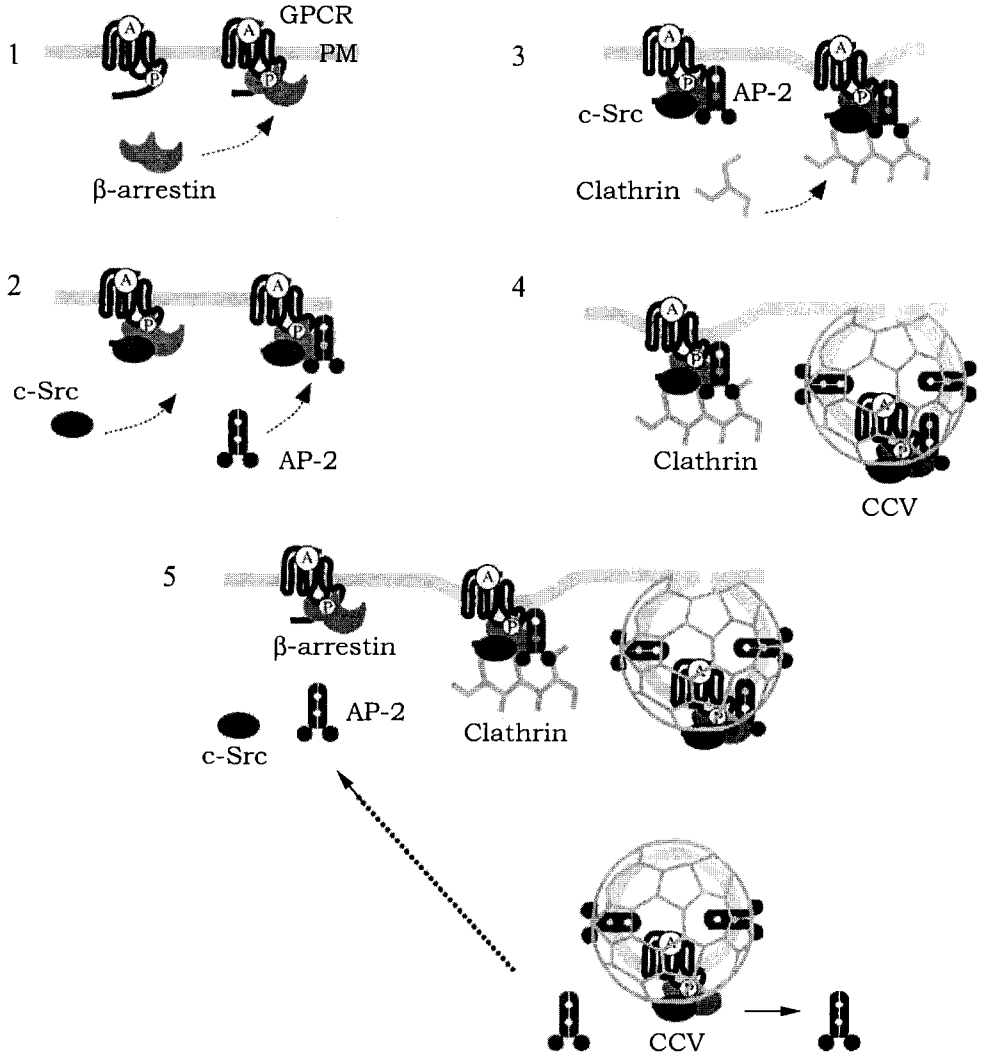

Figure 5.2: Desensitization of GPCRs by β-arrestin mediated endocytosis. 1) Following agonist binding to GPCRs and subsequent phosphorylation of the receptor by G protein-coupled receptor kinase (not shown), β-arrestin translocates to punctated areas of the plasma membrane and binds the activated GPCR. 2) β-arrestin recruits clathrin adaptor protein, AP-2, and the tyrosine kinase, c-Src, to the receptor by directly binding to both proteins. c-Src is known to be a key component in many cell signaling pathways and plays a key role here in regulating the interaction between β-arrestin and the β2-subunit of AP-2 (β2-adaptin). 3) and 4) Clathrin-coated pits begin to bud from the plasma membrane, and eventually, the formation and internalization of clathrin-coated vesicles containing the ternary GPCR complexes is triggered by the presence of multiple complexes and other molecules involved in the endocytic pathway such as the protein dynamin (not shown). 5) As the vesicles are internalized, c-Src promotes the dissociation of β2-adaptin from β-arrestin, which allows for recycling of AP-2 for further internalization cycles. GCPR; G coupled-protein receptor. A; Agonist. P; Phosphorylated site. PM; Plasma membrane. AP-2; Adaptor protein 2. CCV; Clathrin-coated vesicle. Adapted from [19] and [20].

frequently, multiple complexes are sequestered into single vesicles. Internalization of the GPCR proceeds as the CCVs detach from the plasma membrane and enter the cellular interior. Subsequently, the internalized receptor complex dissociates and the adaptor protein returns to the membrane to repeat the cycle of CCV formation, while the GPCR itself continues along either a degradation or recycling pathway [20]. The focus of the following study is to identify and quantify the nature of the dissociation of the endocyctic complex formed between GPCRs, β-arrestin, and AP-2 in living cells, as well as the role of c-Src in regulating this dissociation reaction.

5.3 *Regulation of the Interaction between β-arrestin and AP-2 investigated by Image Cross-Correlation Spectroscopy*

It was recently shown that both the c-Src kinase and the clathrin adaptor protein, AP-2, form a complex with β-arrestin following stimulation of angiotensin II type 1 receptor (AT1R), which is a GCPR involved in the regulation of vasoconstriction and hormone synthesis and secretion [20]. Not only was c-Src identified as part of the complex, but was explicitly shown to phosphorylate three tyrosine residues (Y737, Y874, Y926) in the C-terminal ear domain of β2-adaptin in an agonist-dependent manner [22]. Phosphorylation of β2-adaptin by c-Src, followed by incubation with β-arrestin, was shown to significantly decrease the association of the two proteins as analyzed by Western blotting, and phosphorylation of the Y737 residue, in particular, showed the greatest effect on regulation of this interaction. These experiments demonstrated that the c-Src phosphorylation of Y737 in the C-terminal ear domain of β2-adaptin reduces its ability to bind to β-arrestin. Moreover, a point mutation in β2-adaptin that disrupted its interaction with β-arrestin eliminated the ability of β2-adaptin to be phosphorylated following AT1R stimulation with angiotensin II (Ang II). These results suggested that formation of a complex of the three proteins, β-arrestin/AP-

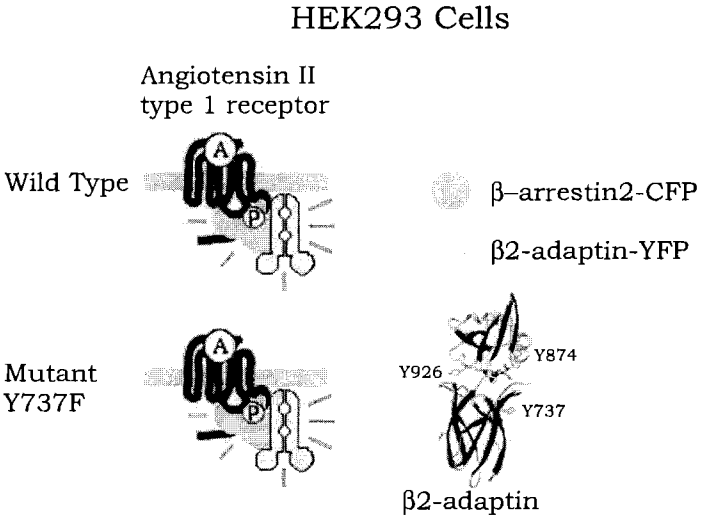

Figure 5.3: Two distinct types of human embryonic kidney (HEK293) cells were generated by transfection of fluorescent-fusion proteins for dual-color confocal imaging. Angiotensin II type 1 receptor (AT1R) along with a fluorescent β-arrestin2 construct of cyan fluorescent protein (CFP) were transfected into the HEK293 cells. In one set of cells, referred to as 'wild type', a second, yellow fluorescent protein (YFP) tagged β2-adaptin subunit was introduced and expressed. In a second set of cells, referred to as 'mutant', a mutated form of the fluorescently tagged β2-adaptin was expressed in which the tyrosine 737 residue was replaced with the non-phosphorylatable amino acid phenylalanine (Y737F). The three tyrosine residues, Y926, Y874, and Y737, that are phosphorylated by c-Src (not shown), are labeled in the crystal structure of β2-adaptin shown in the bottom right portion of the figure. A; agonist, angiotensin II. P; phosphorylated site. Crystal structure adapted from supplemental material of [22].

2/c-Src, following addition of the agonist, Ang II, is necessary for phosphorylation of β2-adaptin by c-Src, which in turn, regulates the interaction between β2-adaptin and β-arrestin. Whether this interaction is regulated by c-Src in live cells, and to what extent the phosphorylation of β2-adaptin alters its affinity for β-arrestin remains to be seen.

In order to address these questions, ICCS was used to measure the persistence of the interaction between β2-adaptin and β-arrestin over time by analyzing two channel confocal fluorescence images of doubly labeled cells. To carry out this investigation, human embryonic kidney cells (HEK293) were transfected with AT1R, and fluorescent constructs of both β-arrestin2 (β-arrestin2-CFP) and β2-adaptin (β2-

adaptin-YFP). In addition, a non-phosphorylatable mutant form of β2-adaptin was engineered by substituting phenylalanine for tyrosine 737 (Y737F) and transfected into the HEK293 cells (see Fig. 5.3). Small interfering RNA (siRNA) was also synthesized and transfected into the HEK293 cells in order to significantly reduce the expression of endogenous β2-adaptin with respect to its fluorescent analogue. All constructs and transfection procedures were performed by the lab of Stéphane Laporte in the department of medicine at McGill University.

Two channel confocal fluorescence images of both wild type and mutant cells were acquired at 37°C at several time points following the addition of a 1 μM solution of Ang II ($t = 0$ s). Following the addition of Ang II, β-arrestin2 translocated to activated GPCRs and punctate areas on the cell membrane appeared in the images, which in most cases, was accompanied by significant changes in cell shape (Fig. 5.4). Due to these cell-shape changes after stimulation, microscope refocusing was usually performed prior to acquisition of subsequent images. Large vesicles were formed after several minutes following the addition of agonist. These vesicles are most likely internalized at this stage, although, due to the size of the plasma membrane (~5 nm) with respect to axial radius of the microscope PSF (~500 nm), it is impossible to resolve the exact location of these vesicles in the cell.

In order to quantitatively assess the observed colocalization between β-arrestin2-CFP (channel 1) and β2-adaptin-YFP (channel 2) in images such as those shown in Fig. 5.4, spatial ICCS was applied to manually selected regions of each set of two channel images that were acquired as a function of the time after the addition of Ang II. The measured spatial cross-correlation and respective detection channel autocorrelation functions were fit to 2D Gaussian functions as in Eq. 2.18 and the fitted amplitudes and beam radii were used in Eq. 2.20 to calculate the number of interacting particles/BA (BA = beam area), and in Eq. 2.21 to calculate the two interaction fractions, $M1_{ICCS}$ and $M2_{ICCS}$. In each colocalization measurement, the NIF (number of independent fluctuations) contained within the manually selected

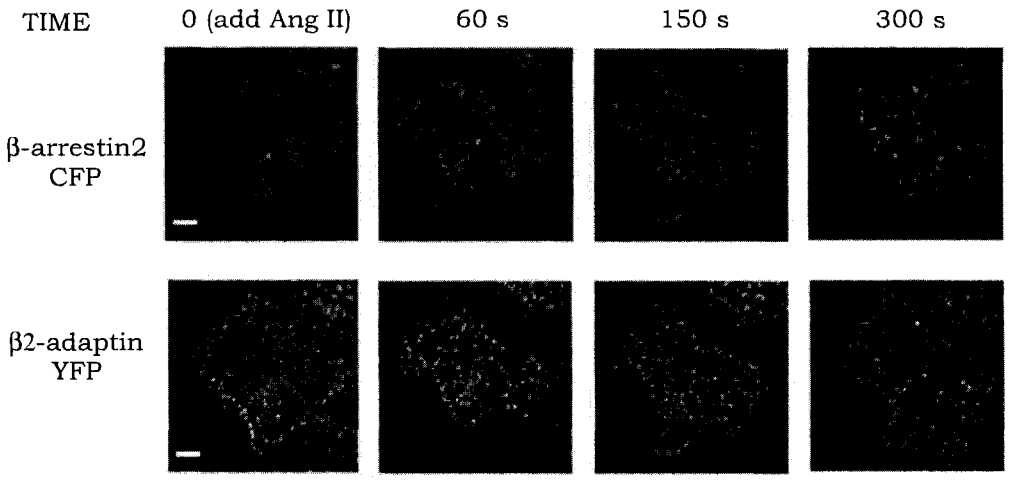

Figure 5.4: Two channel confocal laser scanning microscopy images of β-arrestin2-CFP and β2-adaptin-YFP were recorded at several time points after addition of Angiotensin II (Ang II). Four representative images from each detection channel are shown. Initially, β-arrestin is uniformly distributed throughout the cytosol but rapidly translocated to punctate structures following addition of agonist and eventually formed large (~0.5−1 μm) vesicles. β2-adaptin is pre-clustered, which suggests its incorporation into clathrin-coated pits even in the absence of agonist. Scale bar, 5 μm.

regions of analysis was ~100 (e.g. 60 × 60 pixels, 0.11 μm/pixel, ω_0 = 0.35 μm). According to Fig. 4.3, this means that the IF detection limit for these measurements is somewhere between 20% and 30%. The vast majority (~90%) of measured M_{ICCS} values were well above these detection limits, although there were some as low as 10%. This value can still be considered reliable, however, if we consider the definition that was used to establish the detection limit. Following the analysis of twenty simulations, the minimum interaction fraction at which half of the trials returned a failed cross-correlation fit ($\omega_0 \pm 50\%$ of the input value) was deemed the detetion limit. In the majority of cases, however, several of the trials led to successful fits according to the chosen criterion, moreover, all successful fits led to relative errors of <15%. This means that in certain cases, depending on the particular image pairs in question, smaller IFs than those reported in Fig. 4.3 are possible.

The measured interaction fraction, $M2_{ICCS}$, of five separate wild type and five mutant image time series are plotted in Fig. 5.5. Error bars were omitted for clarity but were estimated to be ~20% given the measured S/B ratios of 30 and 150 for

detection channels 1 and 2 respectively (see Materials and Methods for the definition of S/B and Fig. 4.8). A relatively fast initial increase in the measured colocalization between β-arrestin2 and β2-adaptin was observed for both wild type and mutant cells after the addition of the agonist, Ang II, which was followed by a slower decrease that persisted significantly longer in the case of all mutant cells analyzed. The measured $M1_{ICCS}$ interaction fractions showed identical trends to those of $M2_{ICCS}$. In order to assess this difference in the persistence of colocalization over longer times in the case of cells transfected with the Y737F β2-adaptin mutant as compared to the wild type cells, linear regression was performed on the post-maxima decrease in the measured IF as a function of time for both wild type and mutant cells. Linear regression was performed on a cell-by-cell basis insteasd of averaging over the five measured curves for each cell type due to the temporal differences in the initial response of each cell, as well as the fact that the exact time points at which images were recorded were not identical for all experiments.

Results of the linear fits for a single wild type and mutant cell are shown in Fig. 5.6 along with estimated error bars. The average decrease in the wild type β-arrestin2/β2-adaptin interaction fraction measured using ICCS was almost 4 times faster than that of the mutant complex (slope: -0.011 $\pm$ 0.005 s^{-1} WT vs. -0.0029 $\pm$ 0.0006 s^{-1} for the mutant where errors are the standard deviation of the 5 measurements). A plot of the absolute number density of the the cross-correlated (interacting) species, $\langle N \rangle_{12}$, decays exponentially to zero with a first order rate constant of 0.079 s^{-1} and 0.015 s^{-1} for the wild type and mutant cell respectively.

These results are consistent with the previously measured biochemical data, which suggested that the c-Src-dependent phosphorylation of β2-adaptin regulates its interaction with β-arrestin2 during AT1R internalization, however, for the first time, the effect that phosphorylation of the Y737 residue of β2-adaptin has on dissociation of important regulatory endocytic complexes has been quantified in live cells by this successful application of ICCS. The mechanism by which β2-adaptin phosphorylation

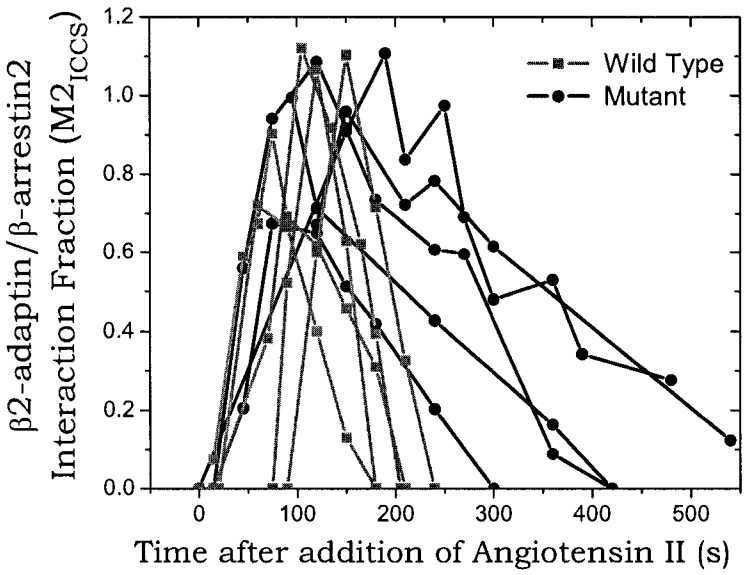

Figure 5.5: Following addition of the AT1R agonist, Ang II, a relatively fast initial increase in the measured colocalization between β-arrestin2 and β2-adaptin was observed for both wild type and mutant (β2-adaptin Y737F) HEK293 cells. The onset of this initial response varied from cell to cell but typically reached a maximum after approximately 60 to 100 s. After reaching a maximum, the amount of colocalization decreased steadily to zero and persisted significantly longer in the case of all mutant cells analyzed.

alters its binding affinity for β-arrestin remains unclear, but interestingly, it has been shown that receptor stimulation is a necessary condition to bring about this effect [20], which implies a more complicated mechanism than a simple conformational change that disrupts binding or recruitment and binding of other regulatory molecules.

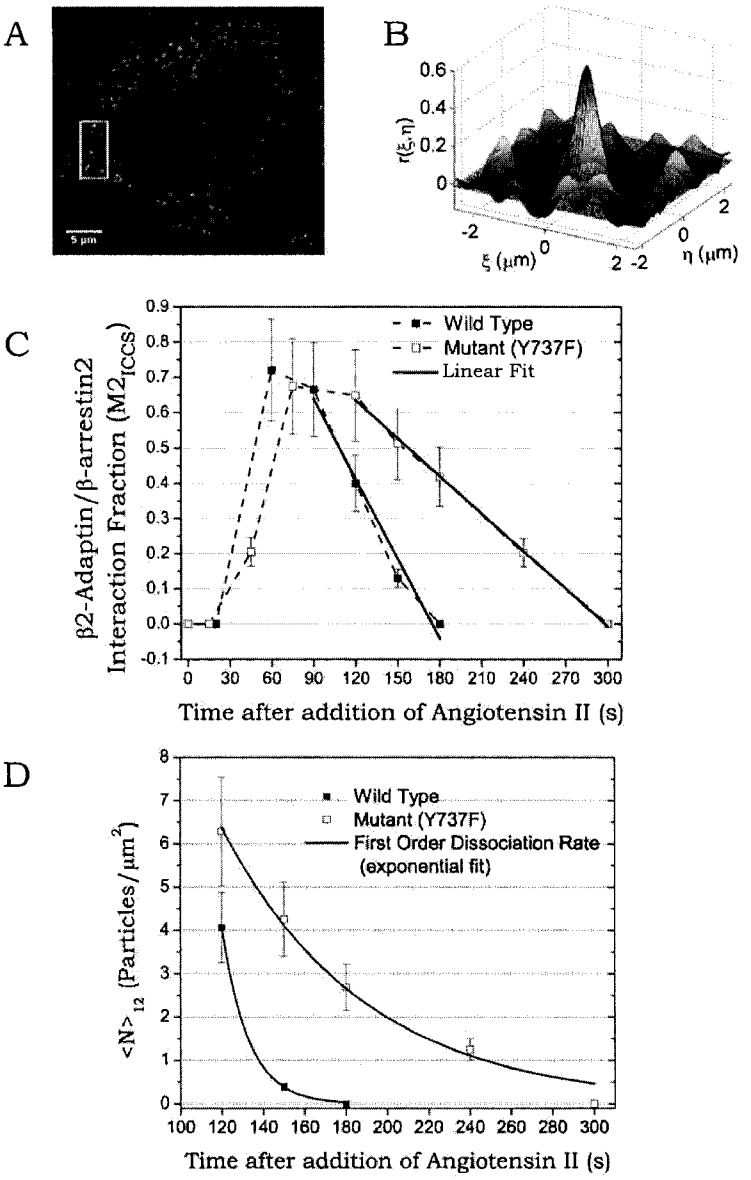

Figure 5.6: A representative two channel overlay image of wild type β2-adaptin (red) and β-arrestin2 (green), 1 minute after the addition of Ang II is shown in the (A) panel of the figure with the corresponding spatial cross-correlation function (solid) and nonlinear least squares fit (mesh) of the outlined region displayed in (B).(C) depicts the measured colocalization for this cell, as well as a β2-adaptin mutant cell as function of time after addition of agonist. Linear fits of the post-maxima colocalization decrease are plotted as solid lines with wild type and mutant slopes of -0.00756 s^{-1} and -0.00356 s^{-1}, respectively. Error bars were estimated for the measured S/B_1 and S/B_2 ratios of 30 of 150, respectively. (D) A plot of the concentration of associated complexes as a function of time decays exponentially with first order dissociation rate constants of 0.079 s^{-1} and 0.015 s^{-1} for the wild type and mutant cell respectively. Error bars were estimated from the S/B ratios as in (C). ©Journal of Cell Science 120, 1723-1732 (2007).

Bibliography

[1] C. D. Strader, T. M. Fong, M. R. Tota, and D. Underwood. Structure and function of G protein-coupled receptors. *Annu. Rev. Biochem.*, 63:101–132, 1994.

[2] T. Gudermann, B. Nurnberg, and G. Schultz. Receptors and G proteins as primary components of transmembrane signal transduction. *J. Mol. Med.*, 73(2):51–63, 1995.

[3] K. Palczewski, T. Kumasaka, T. Hori, C. A. Behnke, H. Motoshima, B. A. Fox, I. L. Trong, D. C. Teller, T. Okada, R. E. Stenkamp, M. Yamamoto, and M. Miyano. Crystal structure of rhodopsin: A G protein-coupled receptor. *Science*, 289(5480):739–745, 2000.

[4] B. Alberts, D. Bray, A. Johnson, J. Lewis, M. Raff, K. Roberts, and P. Walter. *Essential Cell Biology: An introduction to the Molecular Biology of the Cell.* Garland Publishing, Inc., 1998.

[5] J. A. Hirsch, C. Schubert, V. V. Gurevich, and P. B. Sigler. The 2.8 å crystal structure of visual arrestin: A model for arrestins regulation. *Cell*, 97(2):257–269, 1999.

[6] T. A. Kohout, F.-T. Lin, S. J. Perry, D. A. Conner, and R. J. Lefkowitz. β-arrestin 1 and 2 differentially regulate heptahelical receptor signaling and trafficking. *P. N. A. S.*, 98(4):1601–1606, 2001.

[7] O. B. Goodman Jr., J. G. Krupnick, F. Santini, V. V. Gurevich, R. B. Penn, A. W. Gagnon, J. H. Keen, and J. L. Benovic. β-arrestin acts as a clathrin adaptor in endocytosis of the β_2-adrenergic receptor. *Nature*, 383(6599):447–450, 1996.

[8] R. J. Lefkowitz and S. K. Shenoy. Transduction of receptor signals by β-arrestins. *Science*, 308(5721).

[9] D. K. Morrison and R. J. Davis. Regulation of MAP kinase signaling modules by scaffold proteins in mammals. *Annu. Rev. Cell Dev. Biol.*, 19:91–118, 2003.

[10] S.J. Perry and R.J. Lefkowitz. Arresting developments in heptahelical receptor signaling and regulation. *Trends Cell Biol.*, 12:130–138, 2002.

[11] S.S. Ferguson. Evolving concepts in G protein-coupled receptor endocytosis: The role in receptor desensitization and signaling. *Pharmacol. Rev.*, 53:1–24, 2001.

[12] S. K. Shenoy and R. J. Lefkowitz. Multifaceted roles of beta-arrestins in the regulation of seven-membrane-spanning receptor trafficking and signalling. *Biochem. J.*, 375:503–515, 2003.

[13] J. L. Goldstein, R. G. W. Anderson, and M. S. Brown. Coated pits, coated vesicles, and receptor-mediated endocytosis. *Nature*, 279(5715):679–685, 1979.

[14] M. S. Brown and J. L. Goldstein. Receptor-mediated control of cholesterol metabolism. *Science*, 191(4223):150–154, 1976.

[15] D. J. Owen, Y. Vallis, B. M. F. Pearce, H. T. McMahon, and P. R. Evans. The structure and function of β2-adaptin appendage domain. *EMBO J.*, 19(16):4216–4227, 2000.

[16] S. A. Laporte, R. H. Oakley, J. Zhang, J. A. Holt, S. S. Ferguson, M. G. Caron, and L. S. Barak. The β2-adrenergic receptor/βarrestin complex recruits the clathrin adaptor ap-2 during endocytosis. *Proc. Natl. Acad. Sci. USA*, 96(7):3712–3717, 1999.

[17] S. A. Laporte, R. H. Oakley, J. A. Holt, L. S. Barak, and M. G. Caron. The interaction of β-arrestin with the ap-2 adaptor is required for the clustering of β2-adrenergic receptor into clathrin-coated pits. *J. Biol. Chem*, 275(30):23120–23126, 2000.

[18] F. Santini, I. Gaidarov, and J. H. Keen. G protein-coupled receptor/arrestin3 modulation of the endocytic machinery. *J. Cell Biol.*, 156(4):665–676, 2002.

[19] A. Claing, S. A. Laporte, M. G. Caron, and R. J. Lefkowitz. Endocytosis of G protein-coupled receptors: Roles of G protein-coupled receptor kinases and β-arrestin proteins. *Progress in Neurobiology*, 66(2):61–79, 2002.

[20] D. Fessart, M. Simaan, and S. A. Laporte. c-Src regulates clathrin adapter protein 2 interaction with β-arrestin and the angiotensin II type 1 receptor during clathrin-mediated internalization. *Mol. Endocrinol.*, 19(2):491–503, 2005.

[21] J. Inglese, N. J. Freedman, W. J. Koch, and R. J. Lefkowitz. Structure and mechanism of the G protein-coupled receptor kinases. *J. Biol. Chem.*, 268(32):23735–23738, 1993.

[22] D. Fessart, M. Simaan, B. Zimmerman, J. Comeau, F. F. Hamdan, P. W. Wiseman, M. Bouvier, and S. A. Laporte. Src-dependent phosphorylation of β2-adaptin dissociates the β-arrestinAP-2 complex. *J. Cell Sci.*, 120(10):1723–1732, 2007.

6

Advances in ICCS

As discussed in the previous chapters, noncovalent intermolecular interactions regulate practically all cellular processes and are essential to the survival and proliferation of every cell type in all living organisms. It has also been shown that ICCS is a powerful tool to detect these interactions in a minimally-invasive fashion in cultured cell lines using readily available fluorescence probes and microscopy techniques. Of course, as is the case with any analytical technique, ICCS has limitations and must be applied in the proper fashion under the appropriate conditions to obtain valid results. Some of these limitations were tested and discussed in previous chapters and include the interaction fraction detection limits that were observed when the NIF sampled in a pair of images was low, and the large perturbations of the spatial correlation functions introduced by nonuniform particle distributions. Other limitations of ICCS include the error that is observed in the measured number densities when the relative particle brightness yields in either of the recorded images deviates from unity, as in the case when a few very bright particles are imaged in the same detection channel as several particles of lesser brightness. This type of situation can arise from a number of molecular mechanisms, including the case with a distribution in the binding stoichiometry of interacting particles due to the presence of multiple ligand binding sites. In this chapter, new strategies for overcoming some of these limitations are presented that significantly increase the range of applicability of ICCS for measuring intermolecular interactions from two-channel fluorescence microscopy images.

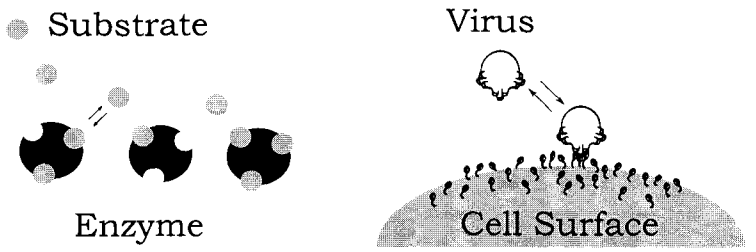

Figure 6.1: Polyvalent interactions in biological systems. There are many types of polyvalent interactions in cellular systems including many enzymes that have multiple binding sites for their substrates. Another example is the influenza virus, which binds to its host cell by association of the trimeric hemagglutinin protein on its surface with sialic acid residues on the surface of the cell. Adapted from [1].

6.1 Variable Binding Stoichiometry

Polyvalent interactions, in which single receptor molecules are found to bind simultaneously to multiple ligands, are prevalent throughout biological systems [1]. Many viruses and bacteria bind to their host cells through polyvalent interactions, which serves to increase the overall strength of the binding as compared with several monovalent interactions (see Fig. 6.1). The surface of the influenza virus, for example, is covered with the trimeric protein, hemagglutinin, which associates with three separate copies of the densely packed sialic acid moiety on the surface of its host cell [2]. Another example of multiple ligand binding in cellular systems is the specific interaction of an antibody molecule with its antigen. As described in detail in Chapter 1, all antibody monomers possess two identical antigen binding sites, and the binding of antibody molecules serves as a surface marker to target foreign invader species to immune cells for subsequent removal from the body. Also, the functional form of an abundant enzyme in the brain, Ca^{2+}/calmodulin-dependent protein kinase II (CaMKII), consists of 12 separate subunits, each of which can bind the calcium-binding protein calmodulin (CaM). The binding of CaM to an autoinhibitory domain of CaMKII results in activation of the enzyme by autophosphorylation, and subsequent phosphorylation of other target proteins [3]. The 12 different CaM binding sites allow for varying degrees of enzymatic activity depending on the ligand occu-

pation number per enzyme molecule. The CaMKII enzyme has been shown to be an important regulatory molecule in neurological signal transmission [4] and has been implicated in playing a role in the formation of long-term memories [5]. These are just a few examples of the numerous multiple-ligand binding proteins that are found in cells, which carry out critical functions in many different regulatory pathways.

Any attempt to quantify molecular interactions using ICCS in systems where multiple ligand binding is possible, would require that both the macromolecule of interest and its ligand be fluorescently labeled with two spectrally distinct fluorophores. Fluorescence images recorded in two detection channels of the two interacting species would then be spatially auto- and cross-correlated in order to determine the corresponding interaction fractions for each detection channel. If, however, two (or more) fluorescently labeled ligands are bound to various receptor molecules, then their locations within the fluorescence image for the ligand channel will appear twice as bright as compared with image locations where only one of the ligands is bound to a receptor (Fig. 6.2).

Due to the diffraction-limited resolution of the microscope used to collect the fluorescence images, it is not possible to resolve the two bound ligands as separate spots. The same is true for higher order complexes as well, and in the following discussion it is assumed that n_b number of bound particles will be n_b times as bright as a single particle for an imaged location, i.e. no fluorescence quenching or enhancement occurs between fluorophores.

Let us consider the effect that the presence of particles with varying numbers of ligands and hence variable brightness yields will have on the calculated spatial auto- and cross-correlation functions. It can easily be shown by substitution of the equations for the spatial intensity fluctuations in each detection channel, (spatial equivalent of Eqs. 2.11 and 2.12), into the general spatial correlation function (Eq. 2.16), that if each fluorescently labeled species, s, has the same brightness factor in channel k, denoted $\eta_{s,k}$, then the autocorrelation of channel k is independent of the value of

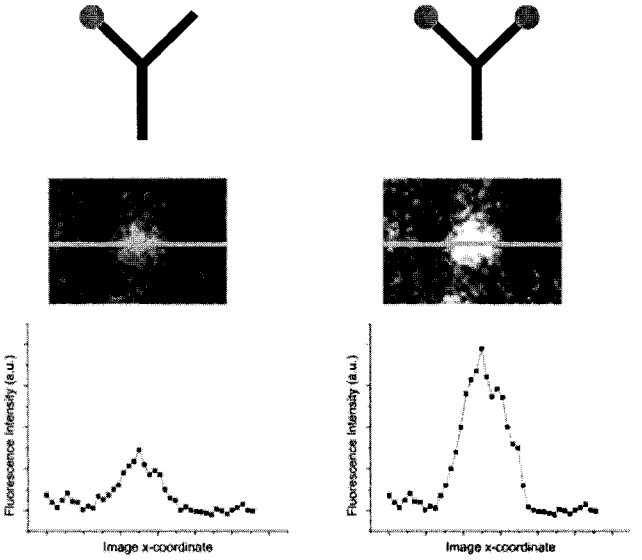

Figure 6.2: An example of an IgG antibody molecule that can bind either one or two antigen ligands is shown. In the case where two ligands are bound, the resulting image intensity profile of the unresolved particles is twice as bright as the case where only a single ligand is bound.

this brightness factor. Similarly, if all the fluorescently labeled species, s, have equal brightness in channel, l, then the cross-correlation (and autocorrelation of channel l) calculated between channel k and l will again be independent of the absolute value of $\eta_{s,l}$. Note that it is not necessary that $\eta_{s,k} = \eta_{s,l}$, and in fact, these two brightness factors are not usually equal. This factor is itself the product of the excitation intensity, overall photon detection efficiency, absorption cross-section and the fluorescence quantum yield for a given fluorophore ($\frac{\text{counts}}{\text{molecule}\cdot\text{s}}$). We do not need to know the actual values of the particle brightness, $\eta_{s,k}$, but only the relative value for each species in detection channels, k and l, due to its presence in the numerator and denominator of the equations for both the auto- and cross-correlation functions. For ICCS analysis it is more practical to define a relative brightness factor measured with respect to a single species (usually the monomeric form) in each detection channel, $Q_{s,k} \equiv \frac{\eta_{s,k}}{\eta_{1,k}}$, since it is much more difficult to measure the absolute value of the molecular brightness in ICCS as compared to FCS, where $\eta_{s,k}$ is measured continuously throughout

the experiment. If the image recorded from detection channel k or l contains contributions from particles with two or more different brightness factors, then the two autocorrelation function amplitudes are given by the sum of the number of fluorescent species contributing in that particular detection channel, weighted by the square of their respective brightness yields, $Q_{s,k}^2$ [6]. Using the definition of the relative particle brightness, the zero spatial-lags amplitudes of the autocorrelation functions for channels, k and l, are given by,

$$r\left(0,0\right)_{kk} = \frac{\sum_{s=1}^{S} Q_{s,k}^2 \left\langle N \right\rangle_{s,k}}{\left(\sum_{s=1}^{S} Q_{s,k} \left\langle N \right\rangle_{s,k}\right)^2} \qquad r\left(0,0\right)_{ll} = \frac{\sum_{s=1}^{S} Q_{s,l}^2 \left\langle N \right\rangle_{s,l}}{\left(\sum_{s=1}^{S} Q_{s,l} \left\langle N \right\rangle_{s,l}\right)^2}, \tag{6.1}$$

where the sum is over the total number of distinct fluorescent species, S, which contribute to either detection channel, k or l, and $\left\langle N \right\rangle_{s,k\,\mathrm{or}\,l}$ is the mean number of particles in the respective detection channel. Similarly, the amplitude of the cross-correlation function is given by,

$$r\left(0,0\right)_{kl} = \frac{\sum_{s=1}^{S} Q_{s,k} Q_{s,l} \left\langle N \right\rangle_{s,kl}}{\left(\sum_{s=1}^{S} Q_{s,k} \left\langle N \right\rangle_{s,k}\right)\left(\sum_{s=1}^{S} Q_{s,l} \left\langle N \right\rangle_{s,l}\right)}, \tag{6.2}$$

where $\left\langle N \right\rangle_{s,kl}$ is the mean number of particles that are detected in both channels, k and l, i.e the mean number of interacting particles. These equations can just as easily be expressed in units of concentration, simply by dividing the auto- and cross-correlation functions by the effective volume of the excitation laser beam focus, V_{eff}, or in the 2D case (that is most common for ICCS analysis applied to membranes), by the excitation laser beam area, BA.

It should be noted that in situations where multiple binding is present and $Q_{s,k}$ is relatively small, it would be extremely difficult to distinguish whether or not a particular image contained contributions from two distinct populations of particles with different brightnesses, and would certainly be impossible at elevated number densities. From the equations above we can see that assuming a single population of

fluorophores with equal brightnesses in their respective detection channels, and the subsequent calculation of the ratio between the auto- and cross-correlation function amplitudes will not represent the 'true' interaction fractions between the molecules due to the increased weighting of the brighter particles. However, while the error in the measured interaction fractions that results from the different relative brightnesses in a given detection channel can be significant, especially when $Q_{s,k}$ is large, the fact remains that the correlation function amplitudes do contain valuable information about the concentrations of the various molecular complexes formed between macromolecules and their ligands. Extracting this information can be a formidable task, but, if some of the underlying properties of the system are known, such as the total number of binding sites, and certain assumptions about these binding sites are valid, then it is possible to use ICCS analysis of two channel images to measure multiple ligand interactions in systems with variable binding stoichiometry.

It is clear that as the number of binding sites, n, increases, extracting of any information from these amplitudes about the underlying distribution of bound ligands becomes increasingly difficult. It is possible, however, to simplify the expression for the spatial correlation function amplitudes given in Eqs. 6.1 and 6.2 by deriving an expression that will allow for the evaluation of the concentrations of all the given species with b ligands bound simply by knowing the total macromolecular concentration of the receptor species, the free ligand concentration, and a single equilibrium association constant. In effect, all of the concentrations of the species that would contribute to the correlation function amplitudes can be related to each other through a single association constant. We can then substitute this expression into Eqs. 6.1 and 6.2, which describe the auto- and cross-correlation amplitudes, to significantly reduce the number of variables in the sums. By measuring the correlation amplitudes, the resulting three equations with three unknowns can then be solved and all of the concentrations of the variable stoichiometric binding complexes can be determined. To do this, let us recapitulate some of the general equations used to describe multiple

equilibria. For a more complete treatment of the subject, see [7].

Consider the n association constants that are required to describe, in general, the binding of a number of small ligands, $[A]$, to a macromolecule, $[P]$, with n binding sites:

$$\begin{aligned} P + A &\rightleftharpoons PA & K_1 &= \frac{[PA]}{[P]\,[A]} \\ PA + A &\rightleftharpoons PA_2 & K_2 &= \frac{[PA_2]}{[PA]\,[A]} \\ &\vdots & &\vdots \\ PA_{n-1} + A &\rightleftharpoons PA_n & K_n &= \frac{[PA_n]}{[PA_{n-1}]\,[A]} \end{aligned} \tag{6.3}$$

where the square brackets represent molar concentrations of the respective species. The concentrations of each complex in terms of the free macromolecule concentration, P, and the free ligand concentration, A, can be written by rearrangement of Eq. 6.3:

$$\begin{aligned} [PA] &= K_1\,[P]\,[A] \\ [PA_2] &= K_1 K_2\,[P]\,[A]^2 \\ &\vdots \\ [PA_n] &= K_1 K_2 \cdots K_n\,[P]\,[A]^n \end{aligned} \tag{6.4}$$

Let us assume that each of the n binding sites are identical, such that each site recognizes the same ligand, A, and that the binding of one ligand will not alter the binding affinities for subsequent ligands (noncooperative binding). If this assumption is valid, then it might appear as though we can simply equate all of the n binding constants described above (i.e. $K_1 = K_2 = \cdots K_n = K$). This is not the case, however, due to the difference in the number of ways that each of the molecular complexes can be formed. For instance, consider the initial reaction of A binding to unligated P. The ligand, A, can bind to any one of the binding sites of P, so there

are n different possible forms of the PA complex. Let us imagine for a moment that we can distinguish between each of these equally probable forms of PA and denote each by $PA_j^\star$. Now we can rewrite our expression for K_1 as,

$$K_1 = \frac{\sum_{j=1}^{n} [PA_j^\star]}{[P][A]} = \frac{n[PA^\star]}{[P][A]}$$
$$= nK_C, \tag{6.5}$$

where K_C is the equilibrium constant that describes the binding of a ligand, A, to any free site on the molecule (i.e. $PA_{b-1}^\star + A \overset{K_C}{\rightleftharpoons} PA_b^\star$). Similarly, we can write expressions that relate each of the n equilibrium constants shown in Eq. 6.3 to the same constant, K_c, by realizing that, in general, the number of distinct complexes that can be formed with b ligands bound, PA_b, out of n binding sites is given by the binomial coefficient, $\binom{n}{b} \equiv \frac{n!}{(n-b)!b!}$. From these expressions we can derive a general formula that allows us to calculate any of the equilibrium constants, $K_1, K_2 \ldots K_n$, from the 'single-site' equilibrium binding constant, K_C:

$$K_b = K_C \left(\frac{n-b+1}{b} \right) \tag{6.6}$$

It is now possible to simplify our expression for the concentration of each of the individual PA_b species by substitution of Eq. 6.6 into Eq. 6.4:

$$[PA_b] = \prod_{j=1}^{b} \left(\frac{n-j+1}{j} \right) K_C^b [A]^b [P],$$

and since the product,

$$\prod_{j=1}^{b} \left(\frac{n-j+1}{j} \right),$$

is simply the binomial coefficient, we may write,

$$[PA_b] = \binom{n}{b} K_C^b [A]^b [P]. \tag{6.7}$$

So for identical and independent binding sites we can calculate the concentrations of all of the possible molecular complexes, $[PA_b]$, formed between a macromolecule that has any number of binding sites and varying amounts of ligand, simply from the single-site equilibrium binding constant, K_C, the concentration of free ligand, $[A]$, and the concentration of free macromolecule, $[P]$. We can therefore substitute this expression into Eqs. 6.1 and 6.2 as mentioned at the outset of the derivation of Eq. 6.7 in order to solve for these three variables that relate to the concentrations of all the species within the system. However, we can increase the ease of solving for these variables, especially when n is large, by noting that in the absence of any higher order complex formation between different macromolecules (e.g. P_2A), all of the fluorescently labeled PA_i species that are recorded in their respective fluorescence detection channel images will be of equal brightness, regardless of the number of ligands to which they are bound (i.e $Q_{P,1} = Q_{PA,1} = Q_{PA_n,1}$). This implies that the amplitude of the autocorrelation function calculated for this detection channel, $r(0,0)_{11}$, will simply equal the reciprocal of the average number of P molecules within the focal volume. This means that, if it is possible, it would be advantageous at this stage to rewrite Eq. 6.7 in terms of the total macromolecular concentration, $[P_{total}]$, by elimination of the concentration of free macromolecule, $[P]$. If one of our unknowns, $[P_{total}]$, can be calculated directly from the reciprocal of the autocorrelation function amplitude, then solving the system of equations will be that much easier. It is in fact quite easy to rewrite Eq. 6.7 in terms of $[P_{total}]$ by taking the summation all $[PA_i]$ complexes including $[PA_0] = [P]$:

$$
\begin{aligned}
[P_{total}] &= \sum_{b=0}^{n} \binom{n}{b} K_C^b [A]^b [P] \\
&= [P] + \sum_{b=1}^{n} \binom{n}{b} K_C^b [A]^b [P] \\
&= [P] \left(1 + \sum_{b=1}^{n} \binom{n}{b} K_C^b [A]^b \right),
\end{aligned}
$$

which can be simplified by using the binomial theorem to obtain:

$$[P_{total}] = [P] (1 + K_C [A])^n \tag{6.8}$$

Solving Eq. 6.8 for $[P]$ and substitution into Eq. 6.7 leads to an expression that allows for calculation of the concentrations all of the $[PA_b]$ species from just the three parameters, K_C, $[A]$ and $[P_{total}]$:

$$[PA_b] = \frac{\binom{n}{b} K_C^b [A]^b}{(1 + K_C [A])^n} [P_{total}] \tag{6.9}$$

6.1.1 *ICCS Analysis of Multiple Binding Interactions: Stoichiometric ICCS*

In order to demonstrate that ICCS is capable of quantifying the interactions in polyvalent systems we have applied the FCCS theory of Kim et al. [8] to the ICCS analysis of single, dual-detection channel image pairs. Consider the case where a single fluorescently labeled macromolecule, G (green detection channel), has two binding sites for a second, fluorescently labeled ligand, R (red detection channel). The auto- and cross-correlation function amplitudes for this type of system can be calculated by using the form shown in Eqs. 6.1 and 6.2. In this case, N_{RFree} is the number of unbound species R per beam area, and $N(GR_b)$ is the number of complexes with b particles of R bound to G per beam area, and $Q_{s,k}$ is the relative brightness of particle s in channel k.

$$r(0,0)_{11} = \frac{Q^2_{GR_0,1}\langle N(GR_0)\rangle + Q^2_{GR_1,1}\langle N(GR_1)\rangle + Q^2_{GR_2,1}\langle N(GR_2)\rangle}{\left(Q_{GR_0,1}\langle N(GR_0)\rangle + Q_{GR_1,1}\langle N(GR_1)\rangle + Q_{GR_2,1}\langle N(GR_2)\rangle\right)^2} \quad (6.10)$$

$$r(0,0)_{22} = \frac{Q^2_{RFree,2}\langle N_{RFree}\rangle + Q^2_{GR1,2}\langle N(GR_1)\rangle + Q^2_{GR2,2}\langle N(GR_2)\rangle}{\left(Q_{RFree,2}\langle N_{RFree}\rangle + Q_{GR1,2}\langle N(GR_1)\rangle + Q_{GR2,2}\langle N(GR_2)\rangle\right)^2} \quad (6.11)$$

$$r(0,0)_{12} = \frac{Q_{GR1,1}Q_{GR1,2}\langle N(GR_1)\rangle + Q_{GR2,1}Q_{GR2,2}\langle N(GR_2)\rangle}{Q_{GR_0,1}\langle N(GR_0)\rangle + Q_{GR_1,1}\langle N(GR_1)\rangle + Q_{GR_2,1}\langle N(GR_2)\rangle} \times \frac{1}{Q_{RFree,2}\langle N_{RFree}\rangle + Q_{GR1,2}\langle N(GR_1)\rangle + Q_{GR2,2}\langle N(GR_2)\rangle}. \quad (6.12)$$

It is assumed that no crosstalk exists between channels, no changes in fluorescence intensity occur upon binding, and that noncooperative binding occurs with equal probability at either site, defined by the single-site binding constant, K_C. All values of $Q_{s,k}$ can be set to one with the exception of $Q_{GR2,2} = 2$. This is due to the fact that the GR_2 species will appear twice as bright as each of the other species, GR_1 and R_{Free}, that are detected in channel R. There are four different unknown number densities in Eqs. 6.10-6.12. However, substitution of Eq. 6.9, which relates all of these number densities to K_C, N_{GTotal}, and N_{RFree}, will result in three equations with three unknowns:

$$r(0,0)_{11} = \frac{\sum_{i=0}^{2} \frac{\binom{2}{i}K_C^i\langle N_{RFree}\rangle^i}{(1+K_C\langle N_{RFree}\rangle)^2}\langle N_{GTotal}\rangle}{\left(\sum_{i=0}^{2} \frac{\binom{2}{i}K_C^i\langle N_{RFree}\rangle^i}{(1+K_C\langle N_{RFree}\rangle)^2}\langle N_{GTotal}\rangle\right)^2} \quad (6.13)$$

$$r(0,0)_{22} = \frac{\langle N_{RFree}\rangle + \sum_{i=1}^{2} Q^2_{GR_i}\frac{\binom{2}{i}K_C^i\langle N_{RFree}\rangle^i}{(1+K_C\langle N_{RFree}\rangle)^2}\langle N_{GTotal}\rangle}{\left(\langle N_{RFree}\rangle + \sum_{i=1}^{2} Q_{GR_i,2}\frac{\binom{2}{i}K_C^i\langle N_{RFree}\rangle^i}{(1+K_C\langle N_{RFree}\rangle)^2}\langle N_{GTotal}\rangle\right)^2} \quad (6.14)$$

$$r(0,0)_{12} = \frac{\frac{2K_C\langle N_{RFree}\rangle}{(1+K_C\langle N_{RFree}\rangle)^2}\langle N_{GTotal}\rangle\left(1+K_C\langle N_{RFree}\rangle\right)}{\left(\sum_{i=0}^{2} \frac{\binom{2}{i}K_C^i\langle N_{RFree}\rangle^i}{(1+K_C\langle N_{RFree}\rangle)^2}\langle N_{GTotal}\rangle\right)\left(\langle N_{RFree}\rangle + \sum_{i=1}^{2} Q_{GR_i,2}\frac{\binom{2}{i}K_C^i\langle N_{RFree}\rangle^i}{(1+K_C\langle N_{RFree}\rangle)^2}\langle N_{GTotal}\rangle\right)} \quad (6.15)$$

By measuring the amplitudes of the auto- and cross-correlation functions, Eqs. 6.13-6.15 can be readily solved for K_C, $\langle N_{RFree}\rangle$ and $\langle N_{GTotal}\rangle$, which in turn, can be used

to calculate the number densities of all $\langle GR_b \rangle$ species using Eq. 6.9.

The error in this type of analysis was estimated by creating simulated images of interacting pairs that had multiple sites for ligand binding. Images were simulated to represent binding of either one or two particles with a known distribution and density. Channel 1 was composed of particles in three distinct states: free (i.e., not associated with a particle from Channel 2); associated with one particle from channel 2; or associated with two particles from channel 2. Association was defined by simply placing particles in the same pixel location in both images (see Materials and Methods, Chapter 3.1).

For these sets of simulations, the distribution of interacting particles was determined by Eq. 6.9 given the total number of channel 1 particles (receptors), N_{GTotal}; the number of free channel 2 particles (ligands), N_{RFree}; and the single-site binding constant, K_C. To recover the concentrations using ICCS, the fitted amplitudes of the spatial cross-correlation function and the two autocorrelation functions were used in Eqs. 6.13-6.15 to numerically solve for K_C, $\langle N_{GTotal} \rangle$, and $\langle N_{RFree} \rangle$. Once these three values were obtained, the concentrations of the different interacting species were calculated using Eq. 6.9. The error associated with ICCS colocalization analysis of a system with two binding sites for a single ligand was small over the density range investigated, as illustrated in Fig. 6.3.

In order to apply the ICCS analysis of multiple binding systems to experimentally acquired images, we re-examined the experiment described in Chapter 4, which compared the ICCS analysis of images with a high density of fluorescently labeled antibodies adsorbed on glass to measurement using automatic colocalization. Briefly, a coverslip was coated with mouse monoclonal anti-PDGF β-receptor IgG, followed by incubation of the coated coverslip with a mixture of secondary anti-mouse IgGs conjugated with either fluorescein isothiocyanate (FITC) or Alexa 633 (Fab- and Fc-specific, respectively). The incubation time of the fluorescently labeled secondary antibody mixture was varied, and the amount of colocalization was assessed by ICCS

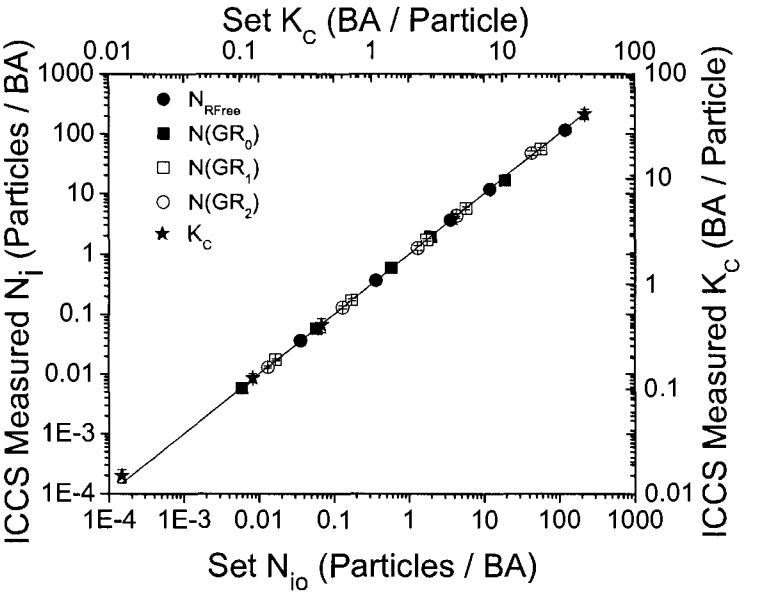

Figure 6.3: Plot of measured species number densities and equilibrium binding constant from ICCS variable stoichiometric analysis as a function of input number density, N_{i0} and equilibrium binding constant, K_C, calculated from the analysis of 50 multiple binding simulation image sets with identical settings for each density. Error bars are standard deviations. No counting or background noise was added to these images.

analysis of the CLSM images recorded for each sample. The measured colocalization was found to increase as a function of incubation time and reached a maximum after ~100 min (Fig. 4.9). All IgG antibodies have two Fab domains and and one Fc domain. In principle, the primary mouse monoclonal antibody that was coated on the glass surface had two available binding sites for the Fab-specific FITC conjugated secondary antibody and one binding site for the Fc-specific Alexa 633 secondary antibody. Therefore, in order to assess whether or not both binding sites of the primary antibody were accessible to the FITC-conjugated secondary antibody, and to measure the distribution of the resulting complexes, the stoichiometric ICCS analysis described above for a two-ligand binding system was applied to the two channel CLSM images of the surface adsorbed antibodies that were recorded after overnight incubation of the secondary antibody mixture on the primary antibody coated glass coverslip. The results are tabulated in Table 6.1. Note that in this case, because the unlabeled pri-

complex	$\langle N \rangle \pm 10\%$ (particles/BA)
RG_0	313
RG_1	255
RG_2	52
G_{Free}	49

Table 6.1: Average number densities of fluorescently tagged antibodies incubated with primary antibodies adsorbed on glass measured using stoichiometric ICCS analysis. The error associated with the measurement of $\langle N \rangle$ was estimated from the measured noises levels of, $S/B_1 = 140$, $S/B_2 = 125$, $WF_1 = 3.0$, and $WF_2 = 5.9$ using Fig. 4.7 and Fig. 4.8.

mary antibody molecules have two possible binding sites for the green fluorescently tagged secondary antibody, and only one binding site for the red fluorescently tagged secondary antibody, we will denote the resulting complexes as RG_b (and not GR_b as above), even though the red and green species do not directly bind to each other but instead bind to distinct locations of the primary antibody.

From the measured number densities presented in Table 6.1, it is possible to calculate two-ligand binding interaction fractions analogous to $M1_{ICCS}$ and $M2_{ICCS}$. For the fluorescent red labeled antibody that can only bind to the primary antibody in a 1:1 ratio we can define the fraction of bound molecules as,

$$\overline{\nu}_R = \frac{\text{total R bound}}{\text{total R}} = \frac{\langle N\left(RG_1\right)\rangle + \langle N\left(RG_2\right)\rangle}{\langle N\left(RG_0\right)\rangle + \langle N\left(RG_1\right)\rangle + \langle N\left(RG_2\right)\rangle}, \tag{6.16}$$

and for the fluorescent green labeled antibody that is capable of binding in a 2:1 ratio with the primary antibody, the fraction of interacting molecules is defined as:

$$\overline{\nu}_G = \frac{\text{total G bound}}{\text{total G}} = \frac{\langle N\left(RG_1\right)\rangle + 2\langle N\left(RG_2\right)\rangle}{\langle N_{GFree}\rangle + \langle N\left(RG_1\right)\rangle + \langle N\left(RG_2\right)\rangle} \tag{6.17}$$

The interaction fractions, $\overline{\nu}_R$ and $\overline{\nu}_G$, were determined to be 0.50 and 0.88 respectively. These values are equivalent to the interactions fractions that were measured using conventional ICCS analysis, as shown in Fig. 4.9 at $t = 1140$ min ($M2_{ICCS} = 0.46 \pm 0.04$, $M1_{ICCS} = 0.88 \pm 0.07$). This implies that when two binding sites are present on a molecule of interest, conventional ICCS can still be applied to measure the overall

interaction fractions. This is due to the fact that a factor of two in the brightness difference between particles detected in a given channel, results in relatively small errors in the recovered number density, regardless of the density ratio between the two species. Application of stoichiometric ICCS, however, is advantageous if knowledge of the distribution of bound particles is desired or if the brightness ratio is > 2 (i.e., there are more than two binding sites available).

6.2 *Improving the ICCS Detection Limits*

Another important parameter that should be carefully considered when attempting to measure interactions using spatial ICCS is the size of the image pairs to be analyzed, or more precisely, the NIF contained within the images. Due to the statistical nature of ICCS it is imperative that a sufficient number of independent spatial samples (fluctuations) be recorded if meaningful results are to be obtained. The effect of spatial sampling was investigated by measuring the detection limit of ICCS as a function of NIF as shown in Chapter 4, Fig. 4.3. From this plot we determined that at NIF values of $\sim$ 1000, which corresponds to 256 $\times$ 256 pixel images at typical pixel resolutions of 0.1 μm/pixel, the zero spatial-lags amplitude of the cross-correlation function becomes indistinguishable from the background correlation peaks at all higher spatial lag values when the interaction fraction is $< 15\%$. Thus, when $\sim$1000 independent fluctuations are sampled within both of the images the ICCS IF detection limit was determined to be 15%, and this value decreased to even lower IFs as more independent samples were measured.

In most experimental situations 15% would be an acceptable interaction fraction detection limit. The difference between 0, 2% or 5% interaction, for instance, is typically not significant in the context of biological systems due to the large cell-to-cell variability often encountered when measuring any parameter in cells. Of greater concern is the dramatic increase in the IF detection limit as the NIF is reduced. Low sampling is a common obstacle encountered for ICCS measurements on various types

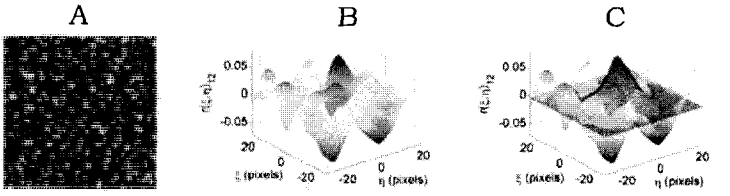

Figure 6.4: A 256×256 two channel overlay image with 10% interaction (below IF detection limit)(A) and the corresponding spatial cross-correlation function (solid)(B). The central zero spatial-lags peak is almost equivalent in amplitude to larger spatial-lags peaks and is therefore difficult to fit to a 2D Gaussian function (mesh)(C).

of cells. The area of a typical cell may be 1000 μm^2 or less, while the diffraction-limited excitation laser beam area of a CLSM is on the order of 0.1 μm^2. This means that across the entire cell, 10^4 independent fluctuations could in principle be measured, which, according to Fig. 4.3 leads to very low IF detection limits of $< 5\%$. A problem arises, however, because in most cases, ICCS analysis over the entire cell is simply not an option, either because the particle distribution is nonuniform throughout the entire cell (to be discussed later in the chapter), or, it is of interest to measure the amount of interaction in a particular subregion within the cell. In either case, we see that it is often necessary to select a 64×64, or 32×32 pixel subregion within the image. For some cell morphologies, even smaller areas would be required for ICCS analysis. This is a major disadvantage, because from the simluation experiments we determined that analysis of these small areas (NIF < 50) is not possible unless the IF is very high ($> 40\%$ in the case of a 64×64 pixel region). Analysis of such regions could lead to false-negative results when in fact the true IF is quite large.

The reason that ICCS analysis fails to detect interaction fractions below the detection limits plotted in Fig. 4.3 is simply due to the difficulty in fitting the cross-correlation function for such limited sampling (see Fig 6.4). The zero spatial-lags amplitude of the cross-correlation function is not well resolved from the background correlation peaks at nonzero spatial lags, which significantly perturbs the fitting routine. An important observation, however, is that the absolute value of the zero spatial-lags amplitude is still representative of the number of interacting particles

even at several IFs values below the reported detection limits, it is just extremely difficult to extract this value from the 2D Gaussian fit. It is worthwhile then, to investigate alternative methods for obtaining the cross-correlation zero spatial-lags amplitude.

Recall that the reason for fitting of the spatial autocorrelation function is the presence of the correlated white noise peak that is present at spatial lags of zero. In principle, however, the zero spatial-lags amplitude of the cross-correlation function could be calculated directly from the spatial intensity fluctuation data (Eq. 6.18) as there should be no cross-correlated white noise (by definition of this noise) present between the two detection channels.

$$r\left(0,0\right)_{kl} = \frac{\left(\delta i\left(x,y\right)_k\right)\left(\delta i\left(x,y\right)_l\right)}{\left\langle i\right\rangle_k \left\langle i\right\rangle_l} \tag{6.18}$$

There are some other factors, however, that must be considered before deciding to abandon the spatial cross-correlation function fitting routine altogether. First, it is not uncommon that the peak of the spatial cross-correlation function occurs at spatial lags greater than zero, and the Gaussian fitting function allows for shifts in the cross-correlation peak. Positional shifts of several pixels in the central peak of the cross-correlation function away from the zero spatial-lags position has been observed in several experiments including the ICCS analysis described in the previous chapter. These pixel shifts would introduce error into the direct calculation of the zero spatial-lags cross-correlation amplitude from the image pixels. Since this is the case, we could also determine the cross-correlation amplitude by searching for a local maximum at small spatial lag values to account for these small pixel shifts, although, due to the fact that multiple peaks are commonly observed at small spatial lags in low IF situations due to sampling noise, this method would be difficult. Secondly, the zero spatial-lags amplitude of the spatial cross-correlation function fails to be a good estimator of the average number of interacting particles at low enough IFs for a given NIF sampled. There will simply not be enough cross-correlated fluctuations to precisely measure these interactions. Therefore, fitting has the added advantage of providing a built-in

check of the quality of the measurement, which the simple calculation directly from the pixel data of the zero-lags cross-correlation does not provide.

In the following section it will be shown that spatial rearrangement, or 'scrambling', of two channel images in a random fashion prior to performing ICCS analysis can significantly reduce the measured IF detection limit for a given NIF. The scrambling procedure that will be described has the effect of lowering the IF detection limit by considerably increasing the ease of fitting the calculated spatial cross-correlation function to a 2D Gaussian function in order to extract the desired amplitude information.

6.2.1 *Image Scrambling for Spatial ICCS*

All information regarding the locations of the particles within an image is lost when a spatial correlation function is calculated from that particular image due to the averaging performed over all equivalent spatial lag values. This implies that spatial rearrangement of all the pixels, or blocks of pixels, within an image, and subsequent spatial correlation, will result in an identical zero spatial-lags value as that of the unaltered image (see Eq. 6.18). Fig. 6.5 shows a schematic diagram of the image scrambling procedure. The only difference between the spatial auto- and cross-correlation functions calculated for a particular image and a spatially scrambled variant of that image, is the width of the correlation function decay, which in turn depends on the size of the scrambled motif. For example, scrambling all of the individual pixels in an image by randomly assigning each one of them a new location will destroy the inherent spatial correlation that was present prior to the rearrangement procedure (i.e. the particles were correlated with themselves over several pixels due to the diffraction-limited width of the focussed laser beam used to excite them). In this case, the spatial correlation (at nonzero spatial lags) of the particles within the image was destroyed by the pixel scrambling, the spatial autocorrelation will have one peak at zero spatial lags (identical to the peak that would result from correlation of the unscrambled

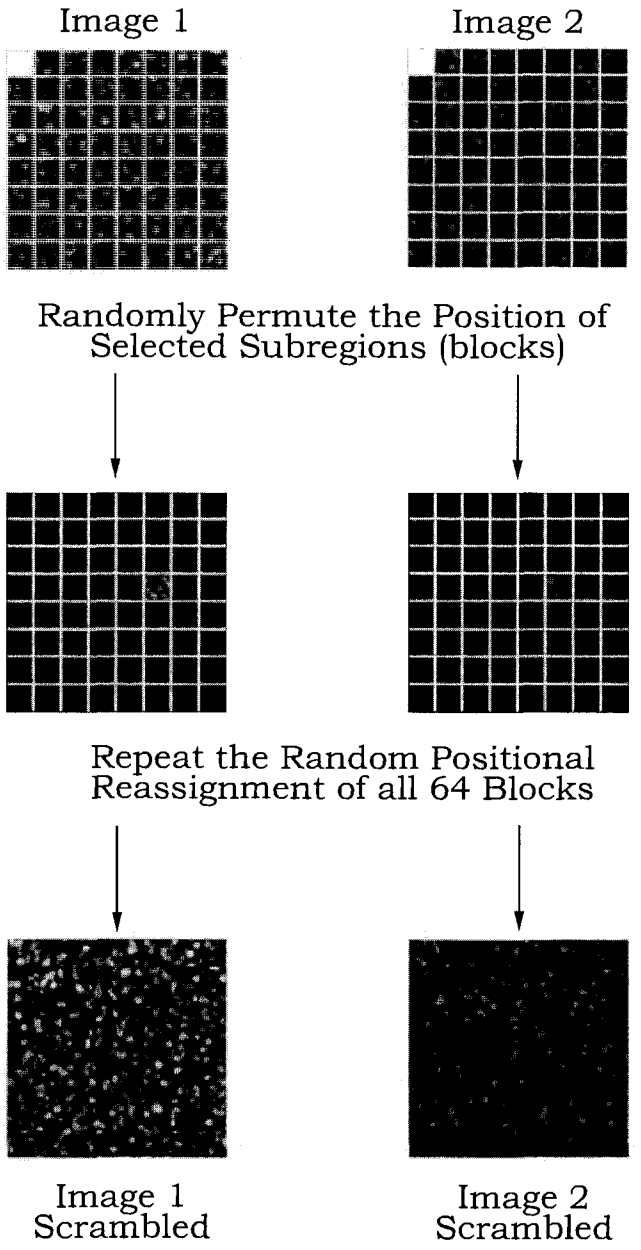

Figure 6.5: Image scrambling procedure. Overview of the process leading to the randomization of $S_x \times S_y$ pixel blocks within an $N_x \times N_y$ pixel image. First, the images are evenly divided into $S_x \times S_y$ pixel blocks. In this example there are 64, 32×32 pixel blocks. The first block of both images (highlighted) is randomly assigned a new position within the 8×8 block array. This process is repeated for the remaining blocks within the images until the resulting scrambled images are obtained.

image) and will effectively be a delta function. We can, however, preserve some of the spatial correlation of the particles within the image if instead of scrambling individual pixels, we divide the image into 2×2 pixel blocks, and then perform the random assignment of these blocks to new locations within the image. This time, the spatial autocorrelation function will only decay to zero after two spatial lags because the 2×2 pixel blocks are still spatially correlated after a shift of only one pixel (Fig. 6.6). The same will be true of the spatial cross-correlation function calculated between two images that were randomly scrambled in an identical fashion. Again, the zero spatial-lags value of the autocorrelation function for the scrambled image is identical to that of the unscrambled image, although the value at a spatial lag of one is lower for the autocorrelation of the scrambled image. By dividing the image into 2×2 pixel sections, and changing the position of these blocks, we have effectively thrown away several of the spatial lag=1 values that would normally be included in the overall spatial average used to calculate this point in the correlation function. Therefore, the overall effect on the correlation function of spatially rearranging the image in this manner is to artificially increase the rate at which the function decays to zero, while leaving the zero spatial-lags amplitude unaffected. The degree to which this rate of decay to zero is increased by scrambling, depends solely on the size of the pixel scrambling blocks used to create the rearranged image.

Artificially increasing the rate at which the spatial cross-correlation function (and autocorrelation functions) decays to zero aids significantly in resolving its central zero spatial-lags peak from background noise correlation at longer lags. This becomes a considerable advantage when attempting to fit this function in a low spatial sampling situation. For this reason, simulation experiments identical to those performed to determine the IF detection limits in ICCS in Chapter 4 were carried out, except this time, the images were randomly scrambled prior to ICCS analysis in order to see to what extent the effect of scrambling had on lowering the IF detection limit. The results are plotted in Fig. 6.7 along with the results obtained by simply fitting the

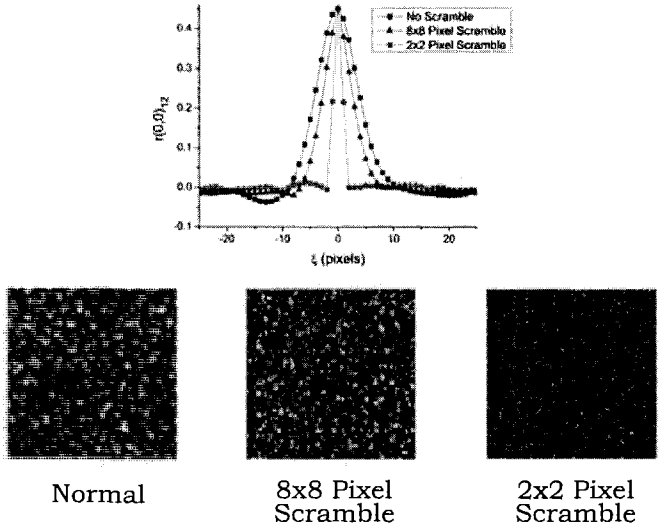

Figure 6.6: The effect of random spatial scrambling of individual pixel blocks within a 256×256 pixel image on the spatial cross-correlation function calculated for the resulting scrambled image. The IF was set to 0.5 for the simulation. A one-dimensional section of the 2D autocorrelation function through the maximum is shown for clarity. Scrambling does not alter the zero spatial-lags value, $r(0,0)_{11}$, but reduces the value of the function at each successive spatial lag. Smaller pixel block sizes used for spatial scrambling will increase the rate at which the spatial cross-correlation (and autocorrelation) function decays to zero.

spatial correlation functions calculated for the unaltered images.

The minimum IF was determined by creating 20 different sets of images with a set IF_0 value (preset colocalization). The images were then analyzed using ICCS to determine the measured IF for the two simulated images. These images were subsequently divided into 4×4 pixel blocks, which were randomly redistributed throughout the image space, and then normal ICCS analysis was applied to calculate the IF for the two scrambled simulated images. This analysis of the unaltered and scrambled image pairs was repeated with decreasing set IF_0 values until more than half of the twenty 2D Gaussian fits of the cross-correlation function failed. The IF_0 at which half of the trials failed was defined as the IF detection limit. A failed fit was defined as a fitted e^{-2} beam radius outside a range of $\pm 50\%$ of the simulation input value, or when the fitted peak position, (υ, ν), was shifted more than 2 pixels from the center, $(\xi = 0, \eta = 0)$. In all cases the total particle density in each channel was held constant and equal at 8 particles/BA. The measured IF approximatley varied with the square root of the NIF sampled in the simulated images as is expected for statistical fluctuation analysis.

We can see from Fig. 6.7 that performing random spatial scrambling of pixel blocks within the images prior to ICCS analysis significantly lowered the measured IF detection limits. This observed reduction is entirely due to the increased probability of obtaining a successful fit of the spatial cross-correlation function, as a result of pre-analysis spatial image scrambling. However, there still exists a fundamental detection limit that can not be overcome by image scrambling. It was found that the measured IF detection limit using the spatial scrambling method was minimized as long as the scrambled block diameter was less than the number of pixels in the e^{-2} radius of the Gaussian convolution function (simulating the laser beam focus radius, ω_0). The 4×4 pixel block size was chosen to provide the maximum advantage in fitting of the reduced-width cross-correlation function, while maintaining a reasonable number of points in the decay of the spatial correlation function to permit fitting.

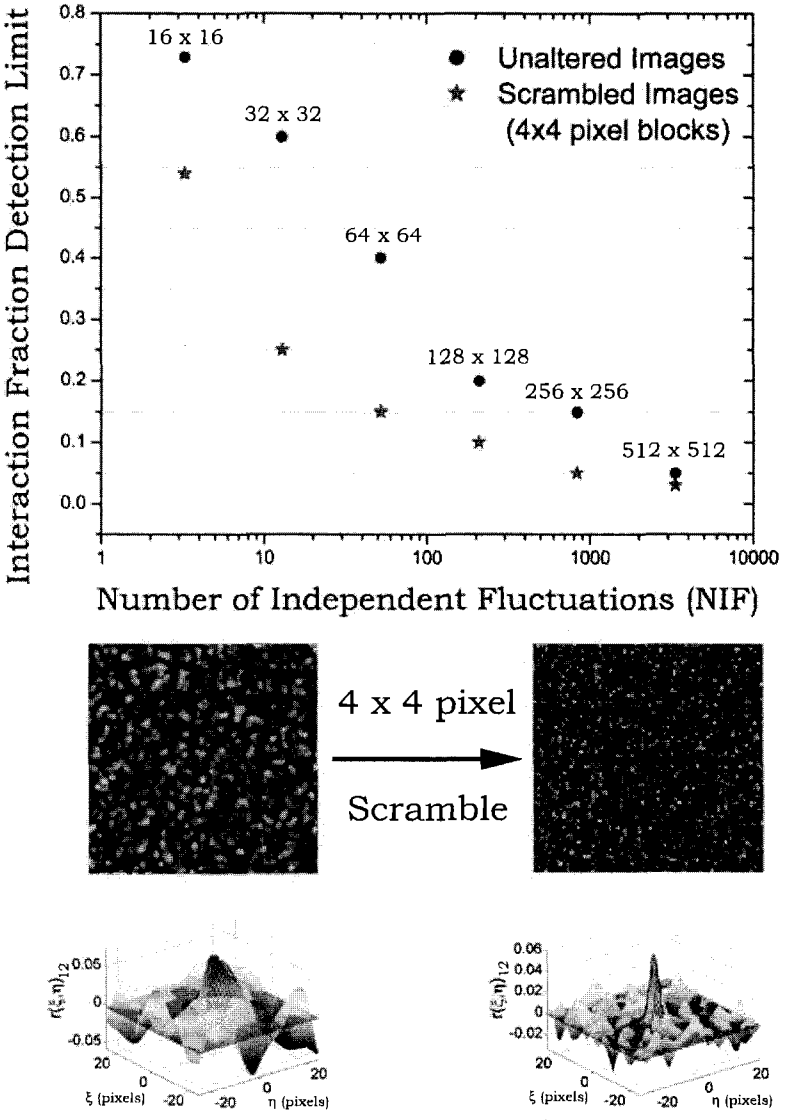

Figure 6.7: The minimum interaction fraction that could be detected using ICCS analysis as a function of the number of independent fluctuations (NIF) in the simulated images for both unaltered and the corresponding scrambled image. Both channel particle densities were held constant and equal (8 particles/BA) as the number of interacting particles was decreased. The detection limit was defined as the IF at which more than half of the 20 trials returned a fitted e^{-2} beam radius outside a range of $\pm 50\%$ of the simulation input value, or the fitted peak position, (υ, ν), was shifted more than 2 pixels from the center, $(\xi = 0, \eta = 0)$. Shown below is an overlay image of a 256×256 pixel image with 10% interaction (below the detection limit) and the corresponding cross-correlation function. The 4×4 pixel block scrambled image is also shown with the corresponding cross-correlation function to demonstrate the much better 2D Gaussian fit when the image is randomly scrambled prior to ICCS analysis.

6.3 Particle Distribution in ICCS

In addition to the NIF sampled within a given image, an equally important parameter that should be considered carefully before applying ICCS to measure interactions is the spatial distribution of the particles themselves. In all of the ICCS measurements presented thus far, it was assumed that the positions of the particles within a given image are randomly distributed from a uniform distribution. If this assumption is valid, then the distribution of particles within each of the small subregions defined by the excitation laser beam area (i.e. a single independent spatial fluctuation) will follow a Poisson distribution. The amplitude of the 2D spatial auto- and cross-correlation functions calculated for these types of images will be related to the particle density, and the functions will decay to zero over the spatial scale defined by the beam focus. If, however, the positions of the particles within a given image are not distributed in a random, uniform fashion, then an additional spatial correlation due to this nonuniform particle distribution will result. The spatial autocorrelation function calculated for these images will then consist of contributions from the spatial correlation of this additional, nonuniform particle distribution, and from the underlying spatial correlation of the individual particles that is related to the desired particle densities (see Fig. 6.8). These additional contributions to the spatial correlation function will, in certain cases, greatly affect its shape, and perturb the subsequent nonlinear least squares fitting. It also influences the relationship between the zero spatial-lags amplitude and the particle number density in a non-trivial way. Not surprisingly, perturbations in either of the two autocorrelation functions due to nonuniform particle distributions will also be manifested in the calculated cross-correlation function between the two images.

As would be expected, nonuniform distributions of fluorescently labeled proteins and other biomolecules in cells are very common, and hence, this presents a difficult challenge for spatial ICS and ICCS analysis of such systems. Typical manifestations of nonuniform particle distributions in cells include large concentration gradients within

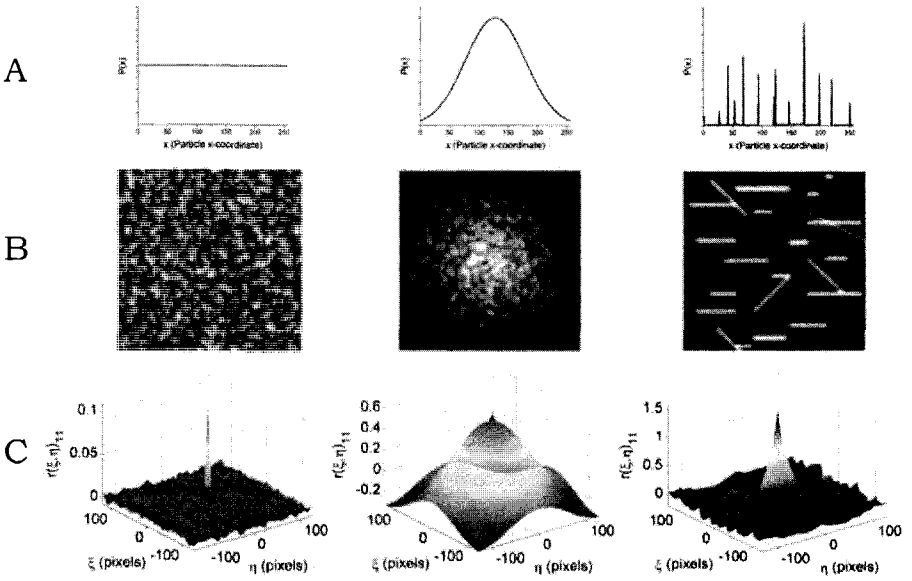

Figure 6.8: The effect of uniform and nonuniform spatial distributions of particles on the autocorrelation function. (A) The probibility distribution function from which the particle x (and y) coordinates were randomly chosen to create the images shown in (B). The spatial autocorrelation functions calculated for the images are plotted in (C). Background noise was added to the images, which manifests itself in the autocorrelation functions as a sharp peak augmenting the zero spatial-lags value.

the imaging region, as well as the formation of large clusters of particles arranged in elongated structures when incorporated into macromolecular complexes (simulated in Fig. 6.8B).

6.3.1 *ICCS Analysis of Focal Adhesion Proteins*

Cellular adhesion and migration is largely regulated by a class of heterodimeric transmembrane proteins called integrins. Integrin proteins provide a direct structural link between the extracellular matrix and elements of the cytoskeleton thereby providing 'anchorage' points for attachment and subsequent migration across surfaces. Many different proteins are recruited to these sites of attachment, in addition to integrins, forming large multi-protein complexes, which are collectively referred to as focal adhesions (FAs) (see Fig. 1.2). In a similar fashion as the GPCRs discussed in the

previous chapter, integrin proteins also act as signaling molecules, by relaying signals that are initiated at the exterior of the cell by the binding of extracellular matrix ligands to integrins in the membrane, and ultimately passing the signal to the interior of the cell. Integrin receptor proteins have been shown to be involved in the signaling pathways leading to cell growth and differentiation as well as cell survival and apoptosis [9].

A complete understanding of the spatial and temporal relationships between the multitude of proteins (e.g. talin, α-actinin, paxillin) that comprise FAs is the goal of many current studies. To this end, the study of integrin and integrin-associated proteins is particularly well suited to ICCS analysis because of the fact that the protein is restricted to a planar surface as it resides in the plasma membrane, and because of the relatively slow dynamics of cell migration that allows for the process to be adequately sampled in time. One major drawback of using spatial ICCS analysis to measure interactions between FA proteins, however, is the spatially nonuniform particle distribution that so often results from the formation of these complexes in the membrane. As shown in Fig. 6.8, any deviation from a uniform particle distribution can make the fitting of the autocorrelation and cross-correlation function amplitude problematic, which makes determination of the interaction fractions, $M1_{ICCS}$ and $M2_{ICCS}$, virtually impossible.

Figure. 6.9A shows a CLSM image of YFP-talin fusion protein in a chinese hamster ovary (CHO) cell plated on a glass coverslip coated with fibronectin, which is the extracellular binding ligand of α_5 integrin proteins. Talin is a protein that is known to bind to the cytosolic tail of the majority of the 8 mammalian integrin β subunits, and acts as an intermediary protein that provides a link between the integrin and the cytoskeleton [10]. Recent studies have shown that the binding of talin to the integrin β subunit causes a conformational change in the transmembrane receptor that leads to its activation (i.e an increase in its affinity for extracellular ligands) [11]. It is this integrin activation process that initiates most of the cell signal transduction pathways

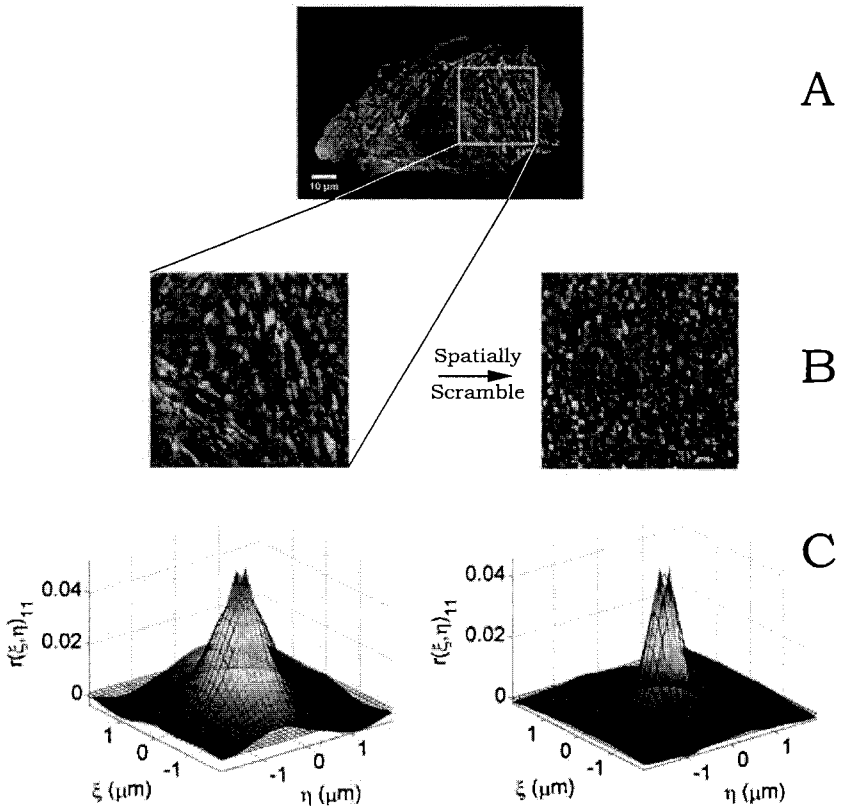

Figure 6.9: (A) A CLSM image of YFP-talin fusion protein in a CHO-K1 cell. (B) A 256×256 pixel region of the cell was selected for spatial correlation analysis. 8×8 pixel blocks of the selected subregion were randomly scrambled. The spatial autocorrelation functions calculated for both the image and the scrambled image are shown in (C) along with 2D Gaussian fit functions (mesh)

regulated by integrin proteins [12].

We can see in Fig. 6.9A that talin is localized in distinct elongated structures which are the FAs. It is also clear from the figure that the spatial autocorrelation of the YFP-labeled talin image is not well fit by the 2D Gaussian function and the fit amplitude is underestimated. As was shown in section 6.2, randomly scrambling blocks of pixels within an image can significantly enhance the ability to fit the corresponding cross-correlation function and extract accurate amplitude information in low sampling situations. Similarly, in cases where a nonuniform spatial distribution of particles leads to large perturbations in the Gaussian fitting to the autocorrelation

function, spatially scrambling the images prior to correlation analysis will allow for a more reliable estimation of the autocorrelation function amplitude from the fit. This is demonstrated in Fig. 6.9B where the region of analysis has been divided into 8×8 pixel blocks, the positions of which have been randomly permuted. The corresponding autocorrelation function is shown in solid color and its nonlinear least squares fit (mesh) appears to provide a much better estimation of the correlation function amplitude than the identical analysis on the non-scrambled image. The actual zero spatial-lags point was not weighted in the 2D fit due to the presence of white noise, and is omitted from the plot.

Although the amplitude of the spatial autocorrelation function determined after applying spatial scrambling is a better estimate of the true zero spatial-lags amplitude, the absolute value of the amplitude is difficult to interpret. Due to the fact that the adhesions in this case are $\sim$10 times larger than the excitation laser beam area, conversion of the autocorrelation function amplitude into a more meaningful number density is difficult [13]. Nevertheless, in an ICCS experiment the ratio of the cross-correlation function amplitude to that of the autocorrelation functions will still represent a measure of interaction between the two labeled species of interest within the sample. The exact meaning of this measure of interaction remains to be seen. In other words, will the cross-correlation of the adhesions themselves dominate the IF or will we be able to extract some information from the 2D fit regarding the interaction of the particles within the adhesions? In order to address this question, the talin image shown in Fig. 6.9A was used to create a binary mask, which in turn, was used to create simulated images with particles confined to specific regions within the image with a set amount of interaction. A schematic overview of this simulation experiment is shown in Fig. 6.10.

The IF measured by randomly scrambling the simulated images and subsequent fitting of the resulting spatial correlation functions was $\sim$1, regardless of the interaction fraction for the particles inside of the adhesions. The large spatial in-

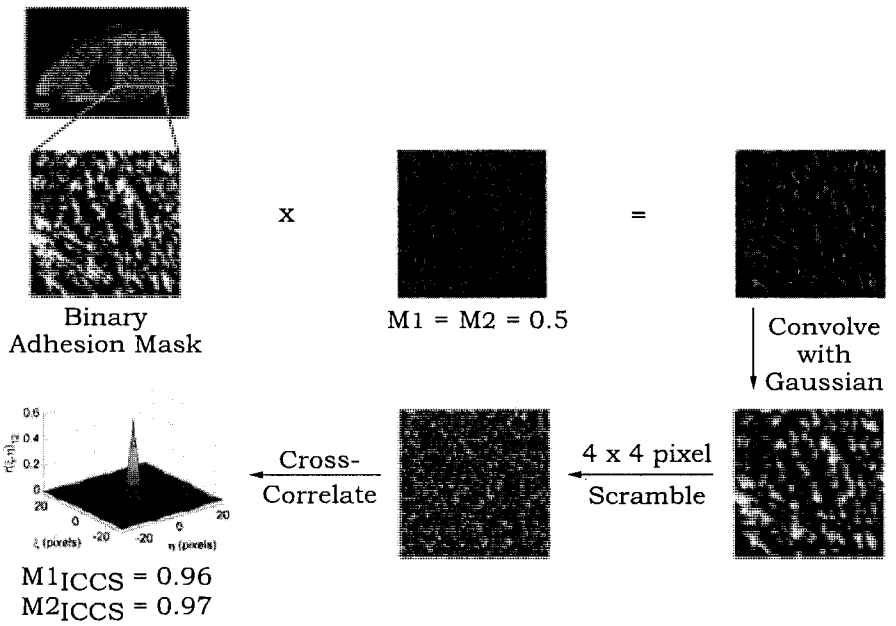

Figure 6.10: A CLSM image of YFP-talin fusion protein in a CHO-K1 cell was used to create a binary mask of FA structures. The mask was multiplied by a simulated two channel overlay image with a density of 120 particles/BA and 50% interaction. The resulting image was convolved with a 2D Gaussian function to simulate the excitation laser beam focus. 4×4 pixel blocks of the convolved image were then scrambled and ICCS analysis was performed. The measured IFs represented the colocalization of the adhesion structures and not the particles within the adhesions ($M1_{ICCS} = 0.96$ and $M2_{ICCS} = 0.97$.

tensity fluctuations arising from the presence of the adhesions dominate the cross-correlation function. Image scrambling does in fact aid in extracting the auto- and cross-correlation function amplitudes, but the calculated IFs represent a measure of the cross-correlation between the adhesions. In certain situations the measurement of the IF between large structures as opposed to smaller molecular complexes might be desired. However, if this is not the case, then practical considerations presented in the following section may aid in the measurement of the molecular IF inside the larger multicomponent complexes.

6.4 *ICCS Analysis of Arbitrary Regions within Images*

ICCS analysis is typically performed on small subregions of the acquired two channel images, due in part to the problems faced by nonuniform particle distributions that was discussed in the previous section, but also because the actual region of interest may only be a small, or oddly shaped subregion of the cell itself (e.g. the leading edge of a migrating cell, Fig. 6.13). Due to the perturbations of the spatial correlation functions caused by the presence of any 'edges' in the images to be analyzed, it is not always possible to select a completely arbitrary square or rectangular subregion of the image for analysis. These constraints restrict the use of ICCS in a number different situations.

In ICCS, spatial intensity fluctuations, $\delta i(x,y)_k = i(x,y)_k - \langle i \rangle_k$, recorded at each pixel position are cross-correlated. The fluctuations that are measured for any pixel that has an intensity value equal to the average intensity of the image recorded in detection channel k, $\langle i(x,y) \rangle_k$, will be zero by definition. Similarly, these pixels will contribute zero to the calculated spatial auto- and cross-correlation functions, $r\left(\xi,\eta\right)_{kl} = \frac{\delta i(x,y)_k \delta i(x+\xi,y+\eta)_l}{\langle i \rangle_k \langle i \rangle_l}$. This simple observation can be used to aid in the ICCS analysis of arbitrarily shaped subregions of the images. For instance, if an arbitrary region of the imaged cell is selected, then the resulting matrix can be 'padded' with the mean intensity of the selected pixels to create a final $N_x \times N_y$ image for subsequent

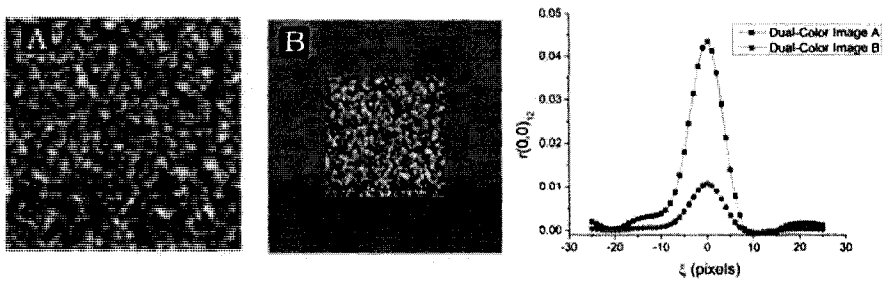

Figure 6.11: For each channel of the 256 × 256 pixel two channel overlay image, the respective mean intensities were 'padded' around the outside of the image matrix creating a final 512 × 512 pixel image. The resulting spatial cross-correlation function (and autocorrelation functions) for the 'mean-padded' image is exactly 4 times lower than that of the original image due to the increased area that was added.

ICCS analysis. The number of pixels that are added to the selected region of interest is not important as long as they surround this region to complete a rectangular $N_x \times N_y$ pixel array. It is easy to see from the equation for the spatial auto- and cross-correlation functions given above and in Eq. 2.16, that any 'padding' of the selected region of interest with its average intensity will not contribute to the numerator of the spatial correlation functions, but will in fact, decrease the entire function by a factor that is proportional to the number of pixels that were added to the image (Fig 6.11).

This is because we have artificially introduced additional spatial lag values to included in the spatial averaging that is performed when calculating the correlation functions. This is easily accounted for, however, and in cross-correlation experiments, where we are only interested in the ratio of the cross-correlation function amplitude to that of the autocorrelation function, no adjustments are necessary because this ratio will remain unchanged.

Arbitrary subregions of images can now be analyzed by simply 'padding' the resulting selection with the mean intensity of the fluorescence signal of that selection. Normal ICCS analysis of such images will then result in accurate IF measurements. A proof of this principle is shown in Fig. 6.12. A simulated 512 × 512 pixel image was created with equal particle number densities in both detection channels of 120 particles/BA and 50% interaction. An area of interest within the two channel overlay

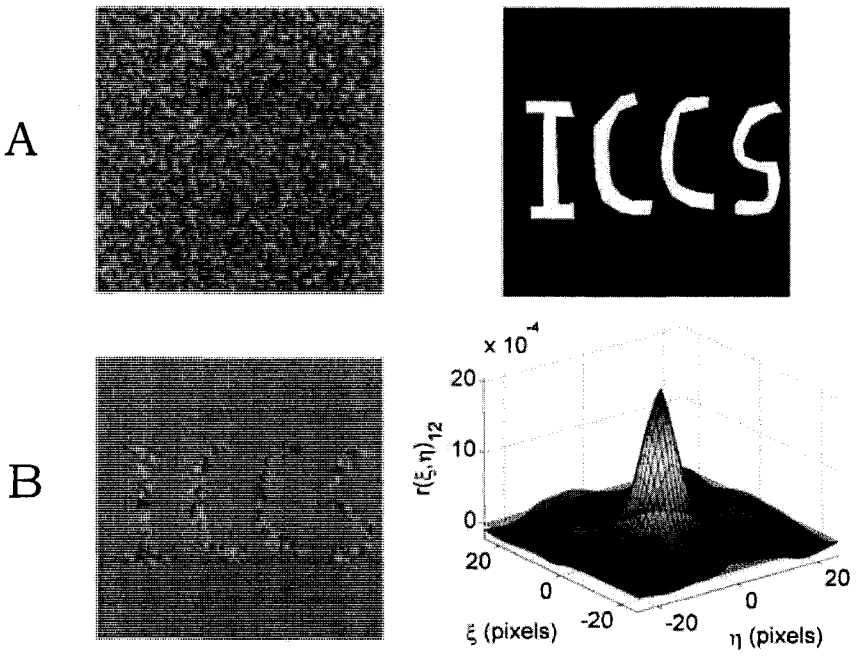

Figure 6.12: (A) A simulated 515×512 two channel overlay image was created with 120 particles/BA in each detection channel and 50% interaction. An area of interest was selected using the 'ICCS' binary mask shown on the right. (B) All pixels outside of the region of interest were set to the mean intensity of the pixels inside the region of interest for each respective detection channel. The spatial cross-correlation function calculated using conventional ICCS analysis was used to determine that $M1_{ICCS}$ and $M2_{ICCS}$ were equal to 0.46 and 0.49, respectively.

image was manually selected. Each pixel in the image that was not selected for the analysis was replaced with the mean intensity of those pixels that were chosen for the analysis. Conventional ICCS analysis was applied to the resulting images, and $M1_{ICCS}$ and $M2_{ICCS}$ were determined to be 0.46 and 0.49, respectively. The total area of the selected region of interest was 168 pixel^2, which corresponds to a NIF of $\sim$360. From Fig. 6.7 we can see that, at an IF of 0.50 and with 360 NIF sampled in this selected region of interest we are well above the IF detection limit in this case. However, if either the region of interest or the IF was significantly smaller, then the random scrambling procedure would have to be applied to the 'mean-padded' images prior to performing the ICCS analysis.

This method for selecting arbitrary subregions within images was applied to two channel TIRF microscopy images in order to measure the IF between the cytoskeletal protein, actin, and one of its binding partners α-actinin. The α-actinin protein constitutes an important component of FAs by linking intracellular actin filaments to transmembrane integrin receptors, thus coupling the cytoskeleton to the extracellular matrix [14, 15] (Fig. 1.2). While these two proteins are known to interact, less is known about the fraction of interacting molecules, especially in different regions of the cell.

In order to measure the interaction between actin and α-actinin at the leading edge of a migrating cell (outside of well-formed FAs), a small subregion of the two channel TIRF image (GFP-α-actinin and monomeric red fluorescent protein (mRFP)-actin) was manually selected. The mean intensity of this small subregion was then used to 'pad' the surrounding regions to create two images with a total size of 256 pixels (Fig. 6.13). 4×4 pixel sub-blocks of these images were then randomly spatially scrambled and ICCS analysis was performed on the resulting images. It was found that there was significant interaction between actin-mRFP and α-actinin-GFP in this manually selected region ($M1_{ICCS} = 0.71$ and $M2_{ICCS} = 0.62$). Further study of this system is required in order to determine the biological implications of this measure-

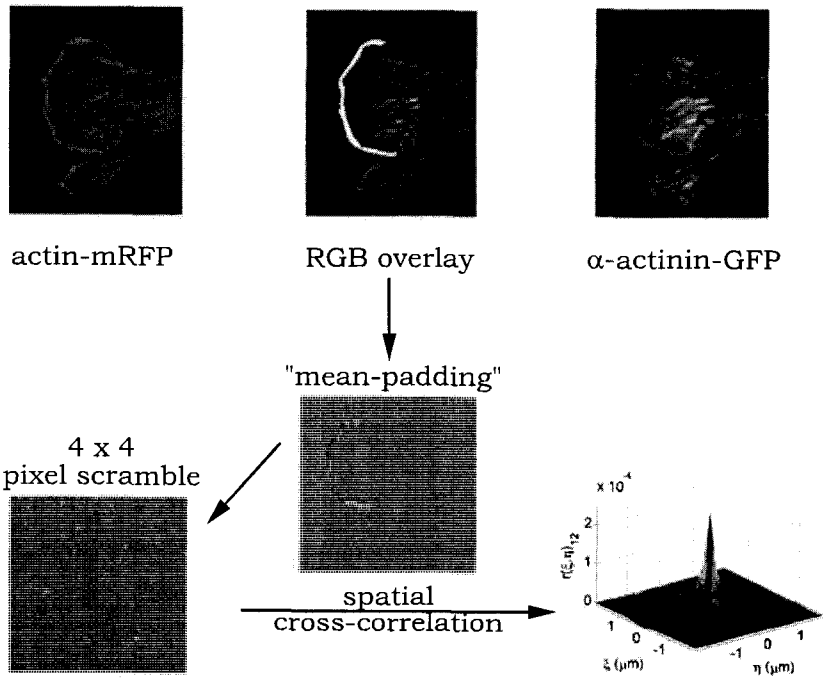

Figure 6.13: The interaction of actin and α-actinin at the leading edge of a migrating cell. A sub-region of a two channel TIRF microscopy image of actin-mRFP and α-actinin-GFP was manually selected (white area). Pre-processing of the images by mean-padding, and spatial sub-block scrambling methods was used to determine the IFs between the two proteins via ICCS ($M1_{ICCS} = 0.71$ and $M2_{ICCS} = 0.62$). Data courtesy of Dr. Claire Brown.

ment. However, as we have shown in this example, the extension of ICCS analysis to manually selected image subregions is possible in two channel fluorescence images, which can be an important tool in measuring molecular interactions in subregions within cells.

Selection of arbitrary regions of interest within the image in this manner significantly increases the range of images to which ICCS can be applied. Combined with random scrambling of pixel blocks within the image, the 'mean-padding' procedure allows for small numbers of interacting particles in small user-defined regions of the cell to be measured with relative ease using ICCS, which would be extremely difficult to measure without the use of such tools. In addition, stoichiometric ICCS analysis can be applied to determine the distribution of multiply-bound ligand complexes, as long as the total number of possible ligand binding sites on the receptor molecule is known. As was shown throughout this chapter, simple methods for overcoming some of the inherent limitations in the ICCS technique have extended its practical application to measuring interactions in cells.

Bibliography

[1] M. Mammen, S.-K. Choi, and G. M. Whitesides. Polyvalent interactions in biological systems: Implications for design and use of multivalent ligands and inhibitors. *Angew. Chem. Int. Ed*, 37(20):2754 – 2794, 1998.

[2] W. Weis, J. H. Brown, S. Cusack, J. C. Paulsona, J. J. Skehel, and D. C. Wiley. Structure of the influenza virus haemagglutinin complexed with its receptor, sialic acid. *Nature*, 333(6172):426–431, 1988.

[3] S. G. Miller and M. B. Kennedy. Regulation of brain type II Ca^{2+}/calmodulin-dependent protein kinase by autophosphorylation: A Ca^{2+}-triggered molecular switch. *Cell*, 44(6):861–870, 1986.

[4] J. Lin, M. Sugimori, R. R. Llinas, T. L. McGuinness, and P. Greengard. Effects of synapsin I and calcium/calmodulin-dependent protein kinase II on spontaneous neurotransmitter release in the squid giant synapse. *Proc. Natl. Acad. Sci.*, 87(21):8257–8261, 1990.

[5] M. Mayford, M. E. Bach, Y.-Y. Huang, L. Wang, R. D. Hawkins, and E. R. Kandel. Control of memory formation through regulated expression of a CaMKII transgene. *Science*, 274(5293):1678–1683, 1996.

[6] N. L. Thompson. Fluorescence correlation spectroscopy. In Joseph R. Lakowicz, editor, *Topics in Fluorescence Correlation Spectroscopy, Volume 1: Techniques*, pages 337–378. Plenum Press, 1991.

[7] C. Tanford. *Physical Chemistry of Macromolecules*, chapter Multiple Equilibria, pages 526–586. John Wiler & Sons, Inc., 1961.

[8] S. A. Kim, K. G. Heinze, K. Bacia, M. N. Waxham, and P. Schwille. Two-photon cross-correlation analysis of intracellular reactions with variable stoichiometry. *Biophys. J.*, 88(6):4319–4336, 2005.

[9] R. Hynes. Integrins: Bidirectional, allosteric signaling machines. *Cell*, 110(6):673–687, 2002.

[10] D. R. Critchley. Focal adhesions - the cytoskeletal connection. *Curr. Opin. Cell Biol.*, 12(1):133–139, 2000.

[11] S. Tadokoro, S. J. Shattil, K. Eto, V. Tai, R. C. Liddington, J. M. de Pereda, M. H. Ginsberg, and D. A. Calderwood. Talin binding to integrin β tails: A final common step in integrin activation. *Science*, 302(5642):103–106, 2003.

[12] B. I. Ratnikov, A. W. Partridge, and M. H. Ginsberg. Integrin activation by talin. *J. Thromb. Haemost.*, 3(8):1783–1790, 2005.

[13] K. Starchev, J. Zhang, and J. Buffle. Applications of fluorescence correlation spectroscopy-particle size effect. *J. Coll. Inter. Sci.*, 203(1):189–196, 1998.

[14] M. Vicente-Manzanares, D. J. Webb, and A. R. Horwitz. Cell migration at a glance. *J. Cell Sci.*, 118:4917–4919, 2005.

[15] C. M. Laukaitis, D. J. Webb, K. Donais, and A. F. Horwitz. Differential dynamics of alpha5 integrin, paxillin, and alpha-actinin during formation and disassembly of adhesions in migrating cells. *J. Cell Biol.*, 153(7):1427–1440, 2001.

7

Conclusion

In the post genomic era, there is a growing trend in biological research to measure, *in vivo*, the myriad of molecular interactions that have been implicated through *in vitro* molecular biological and biochemical experiments. Thus, there is much interest in the development of biophysical measurement techniques that can measure the molecular properties of biomolecules in living cells. Reliable, noninvasive detection and quantification of the complex network of molecular interactions, which forms the basis of all biochemical reactions, is the ultimate goal of many emerging techniques. Technological advances in fluorescence labeling methods and fluorescence microscopy, have sparked the development of several analysis methods for *in vivo* detection of molecular interactions that use fluorescence as the observation variable. Some of these techniques, such as FCCS and FRET, have been studied extensively in an effort to understand their fundamental limitations, and to discover new ways of extending these methods to address an even wider variety of biological questions. These types of studies, combined with the known capabilities of FCCS and FRET, are the reasons why these techniques, in particular, have become reasonably well established biophysical approaches for measuring interactions in living cells. Other microscopy based techniques, that were specifically designed to measure molecular interactions by assessing the amount of colocalization present between overlapping pixels from fluorescence images acquired in two detection channels, are widely used by biologists, even though the accuracy of these techniques has never been extensively characterized.

For these reasons, we initiated the studies reported in this thesis to rigorously test specific methods to measure interactions from analysis of fluorescence microscopy images. We used computer simulations to systematically study the dynamic range and accuracy of spatial ICCS and automatic colocalization, two statistical image analysis techniques for measuring interactions between two fluorescently labeled molecules, which are based on fundamentally different principles (Chapter 4). ICCS is a spatial intensity fluctuation correlation technique that developed as an extension of ICS and FCCS, while automatic colocalization is based on calculation of a single correlation coefficient, which identifies individual colocalized pixel pairs. This study was intended to serve as an experimental guide to using spatial ICCS to measure interactions in single image pairs and to provide a direct comparison to the common automatic colocalization algorithm. Next, by applying the specific knowledge gained through this systematic study, spatial ICCS was used to study a pair of important cell-signal regulating proteins involved in the endocytic pathway. For the first time, the interaction between these two regulatory proteins, β-arrestin and AP-2, was quantified in living HEK293 cells (Chapter 5). Finally, several strategies were outlined to extend the range of applicability of ICCS and to significantly improve its practical usage. The purpose of this study was to demonstrate that spatial ICCS was indeed capable of measuring interactions, not just for ligand receptor systems with a 1:1 binding ratio, but in principle, in systems with 1:n binding stoichiometries. As well, novel image pre-processing procedures were applied to fluorescence images prior to ICCS analysis, to overcome several of the previously determined limitations of ICCS (Chapter 6).

In detail, Chapter 4 presents a critical comparison of colocalization methods that have been used to analyze fluorescence microscopy images for macromolecular interactions in cells. By applying the analysis methods on simulated image sets, we have been able to establish important guidelines on the accuracy and range of applicability of colocalization measurements in two-dimensional systems. Our results from simulated images, as well as control-experiment antibody labeling at high den-

sity on glass coverslips, demonstrate that widely used colocalization techniques that employ Pearson's correlation coefficient (automatic colocalization) are not applicable for higher densities due to density dependent systematic errors. The pertinent densities are typical of many biologically relevant situations. We demonstrate that the magnitudes of the number densities of the two labeled species of interest are of the utmost importance in obtaining meaningful quantitative results when using different colocalization techniques. In many ways, the colocalization techniques compared in this study are complimentary, each with their own advantages and disadvantages and conditions where they work accurately. It was found that the IF detection limits in ICCS varied significantly, from 5%-75%, as the NIF sampled in each image decreased. As the IF detection limit was approached, fitting of the spatial cross-correlation function that is required to obtain a measure of the number of interacting particles, was increasingly difficult. If a sufficient number of spatial fluctuations were not recorded in an image pair, then the off-center peaks in the cross-correlation function due to the random correlation of overlapping particles were approximately equal in magnitude to the zero spatial-lags amplitude of the cross-correlation function. Therefore, it was determined that when using ICCS, every effort should be made to maximize the NIF sampled in a particular image. At all IFs above the measured detection limits, the relative error obtained using ICCS was $< 10\%$. On the other hand, the IF detection limits in automatic colocalization were found to be $\sim 3\%$ for all NIF values. However, at densities approaching 100 particles/BA and interaction fractions > 0.6, automatic colocalization significantly overestimated the IF.

A major drawback of automatic colocalization is that when the two labeled species of interest differed in total number, even by a factor of 2, large systematic deviations from the true colocalization fraction were observed. In addition, automatic colocalization was much more sensitive to noise than ICCS, especially when the particle density of the image was increased. More importantly, these errors go largely undetected because of the difficulty in determining the validity of the result. ICCS analyses are

limited in the same manner, but only when the density ratio of the two labeled species is > 10. Above this ratio, the method fails, but this is clearly indicated by the shape and the aberrant fitting of the cross-correlation function. Thus, the fitting routine provides a built-in check of the ICCS result.

ICCS analyses on two-dimensional systems can also be performed when there are registry shifts between the two image channels, which are common occurrences when the optical system is not perfectly aligned. As long as the shift is equivalent for all pixels, the central peak of the cross-correlation function will simply appear shifted from the zero lags point and accurate results can still be obtained since the fitting function includes variables to account for these systematic pixel shifts.

The major drawback of ICCS is that it requires a relatively uniform spatial distribution of particles within the images to be analyzed. Heterogeneous structures that are larger than the optical diffraction limit, as well as edge boundaries, can distort the spatial correlation function, which makes the fitting routine difficult or impossible to perform. Automatic colocalization, however, is not sensitive to the arrangement of particles and can therefore be used to analyze the colocalization of large structures such as cytoskeletal elements and organelles. Also, unlike automatic colocalization, application of ICCS to two detection channel fluorescence images does not provide information regarding the specific pixel location of the colocalized particles, although it can be applied to smaller image subregions within sampling limits.

Due to the importance of colocalization measurements in biology, and the ease of applicability of image analysis algorithms, it is extremely important to understand the errors associated with different colocalization techniques. Automatic colocalization methods, taken together with ICCS, provide a large dynamic range for accurate, quantitative colocalization measurements for a wide range of cellular processes.

The results of this study of the accuracy and dynamic range of spatial ICCS colocalization measurements were then applied in Chapter 5 to quantify, for the first time in living cells, the interaction between β-arrestin and AP-2, which are two proteins

involved in the clathrin-mediated endocytosis of GPCRs. GPCRs regulate a wide variety of coordinated cellular responses to a large number of external stimuli, and it is a protein called β-arrestin that is largely responsible for the important task of desensitization of these transmembrane receptors. β-arrestin functions as signaling adaptor by recruiting signaling molecules, such as c-Src kinase, to GPCRs for their subsequent interaction with downstream target molecules. β-arrestin also acts as an endocytic adaptor protein, by linking activated GPCRs to elements of the CCV machinery, such as the clathrin adaptor protein, AP-2. The targeting of GPCRs to CCVs by β-arrestin results in the internalization of activated receptors, which effectively provides a signal 'damping' mechanism by preventing extracellular agonists from initiating cellular responses.

Using ICCS, it was possible to show in live cells that mutation of a critical tyrosine residue (Y737) in β2-adaptin (β-subunit of AP-2), which prevented phosphorylation at this site, significantly prolonged its association with β-arrestin in clathrin-coated pits. The amount of colocalization between CFP-β-arrestin and YFP-β2-adaptin was measured from fluorescence images acquired in two detection channels at several time points following the addition of the GPCR agonist, Ang II. It was found that the phosphorylation of AP-2 by c-Src kinase led to a 4-fold increase in the measured dissociation rate of the β-arrestin/β2-adaptin complex.

The ICCS measurements, together with previous *in vitro* studies of this system, showed that the phosphorylation of AP-2 by c-Src kinase regulates the dissociation of endocytic complexes during GPCR internalization via the CCV pathway. This study also demonstrated the ability of ICCS to follow the interaction of two proteins over time, by successive application of spatial ICCS analysis to a time series of two detection channel fluorescence images.

In the final chapter, several strategies were presented to extend the scope of ICCS analysis, and to significantly improve some of the limitations that were discussed in the previous chapters such as the IF detection limits and the sensitivity of ICCS to the

distribution of particles within the cellular system. First, the FCCS theory developed by Kim et al. for measuring the distribution of particle number densities in systems where any number of ligands, 1 to n, can bind to a single receptor macromolecule, was extended to the spatial ICCS. Using simulations, it was shown that ICCS analysis could accurately determine all of the particle number densities present in a system at binding equilibrium when the receptor had two identical binding sites for a single ligand ($\langle N(GR_0)\rangle$,$\langle N(GR_1)\rangle$,$\langle N(GR_2)\rangle$,$\langle N_{RFree}\rangle$). As well, the method could be used to measure the equilibrium association constant, K_C, that describes the binding of the ligand to an unoccupied site on the macromolecule. This type of stoichiometric ICCS analysis was applied to experimental data from imaging studies of fluorescently tagged antibodies adsorbed on glass. The results showed that this antibody binding experiment was consistent with a system where one antibody molecule could bind to another in a 2:1 fashion, as was expected based on the use of IgG antibodies.

As demonstrated in Chapter 3, the IF detection limits of ICCS are strongly dependent on the NIF sampled within the image, which in many experimental situations severely hinder the effectiveness of spatial ICCS. However, it was shown that dividing the image into smaller $S_x \times S_y$ pixel sub-blocks and randomly redistributing these blocks throughout the entire $N_x \times N_y$ image, dramatically improved the fit quality for the calculated spatial cross-correlation function for images with low NIF sampling, thereby, decreasing the IF detection limits. The random scrambling of smaller sub-blocks within the image increases the rate at which the spatial cross-correlation (and autocorrelation) function decays to zero, but does not affect its zero spatial-lags amplitude. The net result is a narrowing of the correlation functions, which increases the chance of obtaining a good fit to the 2D Gaussian function because it leads to better spatial resolution of the central peak from random background correlations. The use of this scrambling method was also shown to extend the application of ICCS to the measurement of the colocalization within large, irregularly shaped objects within the images, such as focal adhesions that normally would preclude the application of

ICCS.

Finally, as a practical tool for implementation of ICCS, a procedure was outlined to select arbitrary regions of the images for analysis. This procedure consisted of 'padding' the matrix that contained the selected region of interest with the mean intensity of that region. ICCS analysis of these types of images resulted in identical spatial correlation functions, reduced by a factor proportional to the number of pixels that were added around the region of interest. This practical tool, combined with the image scrambling procedure, allows one to select individual focal adhesions, cell protrusions, or other small regions of interest for subsequent ICCS analysis of the molecular interactions within these structures.

The development and application of temporal image correlation and cross-correlation based techniques to measure particle dynamics and interactions in living systems has progressed steadily since their initial inception almost 15 years ago. However, the spatial cross-correlation of fluorescence intensity fluctuations has not undergone a similar progression over these years. This is due in part to the interest in obtaining dynamic molecular properties in cells, such as diffusion coefficients or flow speeds, but also to some of the limitations of spatial ICCS investigated throughout this thesis. In many cases, such as the application of spatial ICCS to endocytic complexes presented in Chapter 5, temporal information regarding any of the interacting molecules can still be obtained using spatial ICCS, by acquiring fluorescence images in two detection channels as a function of time with subsequent spatial analysis of each image in the time series. In fact, in any case where the amount of interacting particles changes as a function of time, spatial ICCS is the only image correlation method capable of extracting this information. This observation alone makes spatial ICCS an important tool for measuring interactions in the highly dynamic milieu that comprises the cell. The results presented in the previous chapters will aid in a broader understanding of the capabilities and limitations of ICCS, and allow this powerful technique to be appropriately applied and more widely used to decipher the molecular interactions

that drive the processes of life.

Future work is necessary to fully realize the numerous advantages of spatial ICCS analysis on a much broader scale. This includes a more detailed biological study of the techniques presented in the final chapter. A cellular system with a known interaction fraction of fluorescently labeled interacting proteins would be an ideal system to study the arbitrary selection and scrambling process in a 'real' experimental situation. This system could also be used to study the effects that the shape of the arbitrarily selected region have on the measured interaction fractions. It is possible that selected regions with many vertices could lead to erroneous results, which was occasionally observed in simulation experiments but was not investigated systematically. Finally, combining the programs used to perform spatial ICCS analysis in an easy-to-use graphical user interface could significantly aid other scientists who are unfamiliar with ICCS in applying the technique to their particular system of interest.

8

Appendix A: Derivation of Equation 6.5

The association constants, $K_1 \ldots K_n$, defined in Eq. 6.4 are referred to as 'macroscopic' equilibrium constants because they include all species with equal numbers of bound ligands, regardless of the particular ligand binding sites that are occupied on a macromolecule. From these constants we can derive an experimentally useful expression for the extent of binding, $\bar{X}$, which is defined as the ratio of the number of moles of bound ligand, A, to that of the total moles of macromolecule, P. For the simple case of two ligand binding sites per macromolecule, $\bar{X}$ has the following form:

$$\begin{aligned} \bar{X} &= \frac{[PA_1] + 2[PA_2]}{[P] + [PA_1] + [PA_2]} \\ &= \frac{K_1[A] + 2K_1K_2[A]^2}{1 + K_1[A] + K_1K_2[A]^2} \end{aligned} \tag{8.1}$$

However, if we consider the case where macromolecule, P, has two ***distinguishable*** binding sites for the ligand A, then we can define four distinct 'microscopic' binding constants as follows:

$$k_1 = \frac{[PA_1^\star]}{[P][A]}, k_2 = \frac{[PA_2^\star]}{[P][A]}, k_3 = \frac{[PA_2]}{[PA_1^\star][A]}, k_4 = \frac{[PA_2]}{[PA_2^\star][A]}, \tag{8.2}$$

where $[PA_1^\star]$ and $[PA_2^\star]$ represent the two microscopically distinct forms of $[PA]$. The extent of binding can now be written in terms of these microscopic binding constants:

$$\begin{aligned} \bar{X} &= \frac{[PA_1^\star] + [PA_2^\star] + 2[PA_2]}{[P] + [PA_1^\star] + [PA_2^\star] + [PA_2]} \\ &= \frac{k_1[P][A] + k_2[P][A] + 2k_3[PA_1^\star][A]}{[P] + [PA_1^\star] + [PA_2^\star] + [PA_2]}, \end{aligned}$$

and substituting for the $[PA^{\star}]$ species and $[PA_2]$:

$$\begin{aligned}\bar{X} &= \frac{k_1[P][A] + k_2[P][A] + 2k_1k_3[P][A]^2}{[P] + k_1[P][A] + k_2[P][A] + k_1k_3[P][A]^2} \\ &= \frac{k_1[A] + k_2[A] + 2k_1k_3[A]^2}{1 + k_1[A] + k_2[A] + k_1k_3[A]^2} \\ &= \frac{(k_1 + k_2)[A] + 2k_1k_3[A]^2}{1 + (k_1 + k_2)[A] + k_1k_3[A]^2} \end{aligned} \tag{8.3}$$

If we assume independent and identical binding sites (i.e. $k_1 = k_2 = k_3 = k_4 = K_C$) then Eq. 8.3 can be written as:

$$\bar{X} = \frac{2K_C[A] + 2K_C^2[A]^2}{1 + 2K_C[A] + K_C^2[A]^2} \tag{8.4}$$

From Eqs. 8.1 and 8.4 we can see that the macroscopic constant, K_1, is simply the sum of the microscopic constants K_C (i.e. $K_1 = 2K_C$). Similarly, $K_2 = K_C^2/K_1 = K_C/2$. We can therefore write K_1 as a summation of the n microscopic equilibrium binding constants, which for independent and identical binding sites, are all equal to a single constant, K_C.

9

Appendix B: Biohazardous Materials Certificate

10

Appendix C: Copyright Permission Form

Journal of Cell Science
the company of biologists